

Electronic and Geometric Structures of Transition-Metal-Doped Silver Clusters: Size- Dependent s-d Interaction Studied by Chemical Reaction and Anion Photoelectron Imaging

南川, 賢人

<https://hdl.handle.net/2324/4784408>

出版情報 : Kyushu University, 2021, 博士 (理学) , 課程博士
バージョン :
権利関係 :

Electronic and Geometric Structures of
Transition-Metal-Doped Silver Clusters:
Size-Dependent s–d Interaction
Studied by Chemical Reaction and Anion Photoelectron Imaging

Doctoral Dissertation

Kento Minamikawa

Graduate School of Science

Kyushu University

March 2022

Abstract

In this thesis, reactivity measurements, photoelectron imaging (PEI) spectroscopy, and theoretical calculations were performed on 3d transition-metal-doped silver cluster anions, Ag_NM^- ($\text{M} = \text{Sc-Ni}$), to explore the electronic and geometric structures governing the interaction between the d electrons of a transition metal atom and the s electrons of a host silver cluster.

First, the reaction kinetics of Ag_NM^- toward oxygen was investigated. In a small size range, fragmentations were the major reaction channels for all dopant elements, M. The reaction pathways involved a large amount of excess energy in the reaction, suggesting that M served as an active site on the cluster surface. This was supported by DFT calculations, which showed that small clusters had exohedral geometries. For larger clusters, the major reaction channels changed from fragmentation to O_2 adsorption, suggesting that the reaction site changed from M to Ag. The location of the dopant was found to affect the reaction pathways in this manner.

Focusing on the size-dependent reactivity of $\text{Ag}_N\text{M}^{+/-}$ with 18 valence electrons (18-e clusters), the author discovered remarkably stable clusters, *viz.*, $\text{Ag}_{14}\text{Sc}^-$, $\text{Ag}_{13}\text{Ti}^-$, and Ag_{12}V^- , in addition to $\text{Ag}_{16}\text{Sc}^+$, $\text{Ag}_{15}\text{Ti}^+$, Ag_{14}V^+ , $\text{Ag}_{11}\text{Fe}^+$, $\text{Ag}_{10}\text{Co}^+$, and Ag_9Ni^+ , which have been found in previous studies on cationic clusters. DFT calculations revealed that 1S, 1P, and 1D superatomic orbitals were formed by the interaction between the 3d orbital of the M atom and the sp orbitals of Ag and M. On the other hand, Ag_9Fe^- , Ag_8Co^- , and Ag_7Ni^- showed reactivities that were as high as those of neighboring sizes, even though they had 18 valence electrons. DFT calculations revealed that the dopant in the former stable clusters was encapsulated, whereas the latter three anions showed exohedral geometries. Thus, the endohedral geometry promoted delocalization of 3d electrons as well as electron counting. In the case of Cr- and Mn-doping, the half-filled 3d orbital of Cr and Mn is so stable that the 3d electrons are localized in both endohedral $\text{Ag}_{13}\text{Cr}^+$ and $\text{Ag}_{12}\text{Mn}^+$ and exohedral $\text{Ag}_{11}\text{Cr}^-$ and $\text{Ag}_{10}\text{Mn}^-$.

The present findings for Ag_NCo^- contradict a previous report on Ag_8Co^-

involving photoelectron spectroscopy [Tono *et al.*, *Chem. Phys. Lett.* 2007, **449**, 276], where Ag_8Co^- was assigned closed electronic shells as well as an endohedral geometry. The author performed updated DFT and TDDFT calculations to solve the contradiction. These updated calculations revealed that the photoelectron spectrum (PES) simulation based on the exohedral structure reproduced the reported experimental PES. The electronic and geometric structures of Ag_6Co^- and Ag_7Co^- were also reviewed.

Finally, PEI spectroscopy was performed to probe the electronic structures of the Ag_NM^- . A photoelectron image of $\text{Ag}_{15}\text{Sc}^-$ (19-e) revealed an anisotropic distribution with respect to the laser polarization vector, providing evidence for the 2S superatomic orbital predicted by DFT calculations. In addition, the experimental PES was reproduced by the simulated PES, thus revealing that the Sc 3d electron was delocalized to be accommodated in the superatomic orbital. The PES of $\text{Ag}_{14}\text{Sc}^-$ showed that the electron binding energy (EBE) was larger than those of $\text{Ag}_{13}\text{Sc}^-$ and $\text{Ag}_{15}\text{Sc}^-$, suggesting that $\text{Ag}_{14}\text{Sc}^-$ was the most stable cluster. For Ag_NTi^- , PEI revealed that $\text{Ag}_{14}\text{Ti}^-$ (19-e) had a 2S-type HOMO and that the EBE of $\text{Ag}_{13}\text{Ti}^-$ was the largest. For the V-doped clusters, the photoelectron image and PES of Ag_{13}V^- (19-e) suggested the HOMO may not be a 2S orbital, unlike in the case of the Sc- and Ti-doped clusters. DFT calculations for the Ag_{13}V^- revealed that the 3d orbitals were localized on the V atom. The same result was obtained for Ag_{11}V^- (17-e). Thus, the 3d electrons of Sc and Ti atoms may preferentially delocalize in the clusters, unlike those of a V atom.

The present study investigated the exohedral/endohedral geometry and open/closed electronic shells of Ag_NM^- by reactivity measurements and anion PEI spectroscopy combined with DFT calculations. It was found that the endohedral geometry promoted delocalization of 3d electrons to form superatomic orbitals through interactions between 3d and sp orbitals. The author discovered the stable 18-e species $\text{Ag}_{14}\text{Sc}^-$, $\text{Ag}_{13}\text{Ti}^-$, and Ag_{12}V^- , which form a closed electronic shell with delocalized 3d electrons. In addition, the EBEs and angular momentums of the superatomic orbitals in Ag_NM^- were for the first time detected experimentally using the PEI method.

Table of Contents

Chapter 1. General Introduction	1
1.1. Metal clusters	1
1.2. Heteroatom doping in pure metal clusters	2
1.3. Transition-metal-doped clusters	4
1.4. Objective of the present study	6
Chapter 2. Experimental and Computational Procedures.....	8
2.1. Reactivity experiment	8
2.1.1. Metal cluster ion source	8
2.1.2. Ion guide, ion deflector, and mass selector	9
2.1.3. Linear ion trap	9
2.1.4. Reflectron time-of-flight mass spectrometer.....	10
2.2. Anion photoelectron imaging.....	11
2.3. Quantum chemical calculation.....	12
Chapter 3. Reaction Kinetics	19
3.1. Introduction.....	19
3.2. Results	20
3.2.1. Reaction products.....	20
3.2.2. Simulation of reaction kinetics.....	23
3.2.3. Geometric structures	25
3.3. Discussion	26
3.3.1. Reaction site	26
3.3.2. Formation of reaction products	27
3.3.3. Comparison of the reaction products of Ag_NNi^- and Ag_NNi^+	29
3.4. Summary	30
Chapter 4. Reactivity of $\text{Ag}_N\text{M}^{+/-}$ ($\text{M} = \text{Sc-Ni}$).....	47
4.1. Introduction.....	47

4.2. Analysis of experimental data	48
4.3. Results.....	49
4.3.1. The size-dependent reactivity of $\text{Ag}_N\text{M}^{+/-}$	49
4.3.2. Theoretical results of $\text{Ag}_N\text{M}^{+/-}$	52
4.4. Discussion	55
4.4.1. Category 1; M = Sc, Ti, and V	56
4.4.2. Category 2; M = Fe, Co, and Ni.....	56
4.4.3. Category 3; M = Cr and Mn	57
4.5. Summary	58
Chapter 5. A Revisit to Electronic Structure of Ag_NCo^-	76
5.1. Introduction.....	76
5.2. Theoretical results	77
5.2.1. Geometric structures of Ag_NCo^- for $N = 4-9$	77
5.2.2. Electronic structures of Ag_NCo^- for $N = 6$ and 7	78
5.3. Discussion	78
5.3.1. Localization of 3d electrons	78
5.3.2. Revisit to photoelectron spectra previously reported	78
5.4. Summary	79
Chapter 6. Photoelectron Velocity Map Imaging	84
6.1. Introduction.....	84
6.2. The analysis of experimental data.....	85
6.3. Results.....	86
6.3.1. Sc-doped silver clusters.....	86
6.3.2. Ti-doped silver clusters	87
6.3.3. V-doped silver clusters.....	89
6.4. Discussion	91
6.4.1. Behavior of 3d electrons in Ag_NSc^-	91
6.4.2. Behavior of 3d electrons in Ag_NTi^-	93

6.4.3. Behavior of 3d electrons in Ag_NV^-	94
6.5. Summary	96
Chapter 7. Concluding Remarks.....	114
References	118
List of Publications.....	124
Acknowledgements	126

Chapter 1. General Introduction

1.1. Metal clusters

A metal cluster is a sub-nanometer sized particle consisting of two to several hundred metal atoms. These clusters have been attracting much attention as catalysts because they show remarkable chemical and physical properties, *e.g.*, stability, reactivity, and magnetic properties.^[1,2] The properties of metal clusters are characterized on the basis of their electronic structures, which have been investigated for simple metal clusters by mass spectrometry,^[3–5] reactivity with O₂ gas,^[6,7] photoelectron spectroscopy,^[8,9] and DFT calculations.^[10,11]

For example, Knight *et al.* reported that sodium clusters, Na_N, show a rich abundance at $N = 8, 20, 40, \dots$ in the mass spectrum, which are called magic sizes.^[3] The high stability of these magic-sized clusters can be explained by the spherical jellium model in which free electrons move around in the potential of the background positive charges of the nuclei.^[3,12] Such a 3D quantum-well potential creates discrete energy levels of electronic shells. Since the number of electrons for shell closing is 2, 8, 18, 20, ..., these magic-sized Na_N form a closed electronic shell because one 3s electron per Na atom is included in the clusters. The discrete orbitals in the jellium model have an angular momentum similar to those of atomic orbitals, and thus are labeled 1S, 1P, 1D, 2S, ..., which are called superatomic orbitals. A theoretical study on Na₂₀ revealed that s electrons are delocalized in the cluster to achieve electronic-shell closure by filling the 1S, 1P, 1D, and 2S orbitals.^[13] Similar behavior has been reported for cluster ions of coinage metals, *i.e.*, Au, Ag, and Cu, which possess a single valence s electron.^[4,5]

The superatomic concept is also applicable to clusters having p electrons. For example, Leuchtner *et al.* investigated the reaction of aluminum cluster anions, Al_N[−], with oxygen.^[6] In the mass spectrum, Al₁₃[−] exhibited a high resistance to oxygen etching, and can be regarded as a magic-sized cluster. Since the Al atom has two 3s and one 3p electrons, Al₁₃[−] has a total of 40 valence electrons, including the negative charge. DFT

calculations by King *et al.* revealed that the 40 electrons in Al_{13}^- occupy 1S, 1P, 1D, 2S, 1F, and 2P to form a singlet state,^[10] suggesting that p electrons as well as s electrons are delocalized in the cluster to form the closed electronic shell.

The properties of these clusters are governed not only by their electronic structures but also by their geometric structures. Luo *et al.* reported that Ag_{13}^- with a pyramidal geometry shows enhanced stability in its reaction with oxygen despite not being a magic-sized cluster in the spherical jellium model.^[14] The author performed DFT calculations, which revealed that a distortion in the geometry of Ag_{13}^- induced a splitting of the D shell, leading to a large electron detachment energy due to a large HOMO–LUMO gap. This suggests that clusters such as Ag_{13}^- have high spin excitation energies and thus do not react with O_2 because these clusters with an even number of valence electrons require spin accommodation for activation of O–O bonds. For aluminum oxide clusters, Watanabe and Tsukuda performed photoelectron spectroscopy and DFT calculations to characterize the geometric structures of Al_{14}O^- and $\text{Al}_{15}\text{O}_2^-$.^[15] They found that these clusters exhibit high stability because they form geometrically stable icosahedral Al_{13} motifs.

1.2. Heteroatom doping in pure metal clusters

Heteroatom doping is a useful method for creating metal clusters with new properties. The electronic structure of the host metal clusters is modified by the interaction between the valence electrons of the host metal clusters and those of the dopant. The geometric structure also changes from that of the host clusters, and it is possible to generate various geometric motifs depending on the dopant location. To this end, a wide variety of doped clusters have been investigated to characterize their electronic and geometric structures.

In an early-stage work, Kappes *et al.* reported photoionization mass spectra for K_nLi_m , K_nMg_m , and K_nZn_m ($m = 0,1$), where the clusters were generated through supersonic expansion of the corresponding metal vapors and ionized by light from a 1

kW Xe/Hg arc lamp.^[16] In the mass spectrum of K_nLi , K_7Li and $K_{19}Li$ exhibited rich abundances, suggesting that these clusters formed a closed electronic shell with 8 and 20 valence electrons, respectively, because K and Li atoms provide one valence s electron. On the other hand, the mass spectra of the Mg- and Zn-doped clusters showed local maxima at $n = 8$ and 18, and have a total of 10 and 20 valence electrons, respectively. The magic numbers were explained by the reversal of the filling order of the 1D and 2S shells, resulting in closed shells at 2, 8, 10, 20, ... (1S, 1P, 2S, 1D, ...). The extended-Hückel calculations for K_8Mg showed that the most stable structure is a potassium cube with a central magnesium, which causes such an orbital reversal. The results suggested that Mg and Zn provide two valence electrons from their 3s and 4s orbitals, respectively, to form a closed electronic shell. Bouwen *et al.* investigated the relative stabilities of $Au_nCu_m^+$ by photofragmentation.^[17] The photofragmentation pattern for Au_nCu^+ showed abundance steps at $n = 8, 18, 20$, and 34. In addition, $Au_nCu_2^+$ ($n = 7, 17, 19, 33$) were found to be magic-sized clusters in the mass abundance spectrum, and have 8, 18, 20, and 34 valence electrons, respectively. Thus, the s-type valence electrons of the dopant were delocalized over the doped clusters to occupy the superatomic orbitals.

Lievens's group reported photofragmentation experiments on Al-doped Au_n^+ with valence s and p electrons.^[17] For Au_nAl^+ , enhanced stability was mainly observed for $n = 6$ and 18. This indicated that the two 3s and one 3p electrons of the Al atom are delocalized in the clusters, inducing electronic shell closure with 8 and 20 valence electrons. Other examples of doping p electrons are silicon-doped gold and silver cluster anions, which have been investigated using photoelectron spectroscopy by Majer and von Issendorff.^[18] For Si-doped gold clusters, the photoelectron spectrum (PES) of $Au_{30}Si^-$ showed a peak that was clearly separated from the other peaks. They assigned this peak to the singly occupied 2P state, suggesting that all of the valence electrons of the Si atom are delocalized. Similarly to $Au_{30}Si^-$, a new peak appeared for $Au_{54}Si^-$ in the PES, which indicates the opening of the 2D shell. On the other hand, a new peak was observed for $Ag_{56}Si^-$ instead of $Ag_{54}Si^-$, which means that two electrons were

delocalized. Thus, the localization/delocalization of p electrons may depend on the combination of dopant and host metal elements.

Nonose *et al.* reported the reactivity of vanadium-doped cobalt clusters toward H₂.^[19] They found that the reactivities of Co₅V and Co₇V exceeded those of Co₆ and Co₈, respectively, by exchanging one Co atom for a V atom. This suggests that in these clusters, the V atom serves as an active site for H₂ adsorption. On the other hand, the reactivity of Co₁₂V is lower than that of Co₁₃. A subsequent theoretical study by Datta *et al.* revealed that the most stable structure is an icosahedral geometry with an encapsulated V atom, which is shielded from H₂ by all the surface Co atoms.^[20] Thus, the location of the dopant atom affects the cluster properties.

1.3. Transition-metal-doped clusters

Among heteroatom-doped systems, transition-metal-doped clusters such as Co_NV have attracted much attention because transition metal elements play an important role in determining chemical and physical properties owing to their open d orbital. Of particular interest are alkali and coinage metal clusters doped with a transition metal atom, where the character of the d electrons is perturbed by the interaction between the d electrons of the dopant and s electrons of the host metal. It is known that in bulk dilute magnetic alloys, the dopant atom retains (loses) its magnetic moment originating from localized d electrons when the s–d interaction is weak (strong).^[21–23] However, the s–d interaction is not trivial for doped clusters because the electronic structure is subject to the quantum size effect; the situation is much different from that in bulk metals. This has motivated extensive exploration of a variety of transition-metal-doped clusters, both experimentally and theoretically.

Theoretical studies initially investigated clusters with an icosahedral cage of coinage metals as a host, enclosing a transition metal dopant M, *viz.*, Cu₁₂M,^[24] Ag₁₂M,^[25,26] and Au₁₂M,^[27,28] which were followed by studies incorporating spin–orbit coupling.^[29,30] One of the notable finding was Au₁₂W, which was predicted to be a

closed-electronic-shell species according to the 18-electron (18-e) rule known from organometallic compounds, with contributions of twelve Au 6s and W 5d⁴ 6s² electrons, suggesting delocalization of 5d electrons.^[27,31] A similar electronic-shell closure has been reported for other combinations of coinage metal hosts and group 6 dopants, *e.g.*, Ag₁₂Mo,^[26,30] Ag₁₂W,^[26] and Cu₁₂Cr.^[32] These stable species exhibit notable properties, such as a high electron binding energy and a large HOMO–LUMO gap. Computational studies based on DFT have been extended to explore other sizes, predicting a variety of stable doped clusters as reviewed very recently, where the electron-counting rule played an important role in characterizing the physical and chemical properties of the clusters.^[33]

Experimental studies exploring such transition-metal-doped clusters have been performed on ions, rather than neutral species, which were investigated mostly through theoretical work, to take advantage of mass spectrometry for size selectivity. The first report was on free Au cluster cations doped with a 3d transition metal atom, where the abundance of Au_NM⁺ clusters (M = Sc – Ni) was measured after photofragmentation to identify stable sizes *N*.^[34,35] The prominent abundance of Au₁₆Sc⁺ and Au₁₅Ti⁺ revealed that they form an 18-e closed shell^[36] consisting of delocalized 4s and 3d electrons of Sc 3d¹ 4s² and Ti 3d² 4s², Au 6s¹ from each Au atom, and minus one for the positive charge, whereas other dopants (Cr, Mn, Fe, Co, and Ni) were found to delocalize only 4s electrons. The experiment was extended to doped Ag clusters Ag_NM⁺,^[37,38] where Ag₁₆Sc⁺, Ag₁₅Ti⁺, Ag₁₄V⁺, Ag₁₁Fe⁺, Ag₁₀Co⁺, and Ag₉Ni⁺ were identified as stable clusters; all of these suggest 18-e shell closure by the participation of delocalized 3d electrons. Indeed, DFT calculations have revealed that the electronic structure of Ag₁₀Co⁺ consists of 1S-, 1P-, and 1D-like superatomic orbitals occupied by Ag 5s and delocalized Co 4s and 3d electrons, forming a singlet state with completely unpolarized spins, and, therefore, that the magnetic moment on the dopant Co is quenched.^[37] The experiment was also applied to Cu_NSc⁺ clusters, the results of which showed that Cu₁₆Sc⁺ is an extremely stable cluster. It possesses not only an 18-e closed electronic shell but also a highly symmetric geometry with a Frank–Kasper-type tetrahedron,^[39] forming clear superatomic

orbitals of 1S, 1P, and 1D; its neutral counterpart, Cu_{16}Sc , was identified to have a superatom character similar to those of alkali metal atoms.^[40,41] In addition to these abundance measurements examining the stability of doped clusters, X-ray magnetic circular dichroism (XMCD) spectroscopy has been performed to probe the local magnetic moment on the dopant atom. An experiment on Au_NCr^+ ($N = 2-7$) revealed that the local moment on the Cr atom is correlated with the energy gap of the host Au cluster, showing a finite-size effect in the s-d interaction.^[42]

1.4. Objective of the present study

The present thesis focuses on the s-d interaction in silver clusters doped with a 3d transition metal atom. Among the host metals Au, Ag, and Cu, Ag differs from the other two in that the 5s-4d energy gap is so large that the 5s electrons are effectively free electron, whereas the corresponding 6s-5d and 4s-3d gaps are so small that the s orbitals are perturbed by their own d orbitals in Au and Cu.^[43,44] Therefore, it is a distinct feature of Ag that the 3d electrons of the dopant interact primarily with the s electrons of the host cluster. It should also be noted that the 3d electrons of a dopant atom tend to delocalize not only in Sc- and Ti-doped clusters as observed for Au as a host^[34] but also in V-, Fe-, Co-, and Ni-doped Ag clusters.^[37] As such, the present author is interested in the use of Ag as a host to examine the electron-counting rule systematically both for cations and anions, which should give stable clusters for a host metal of varying size depending on the charge state. Recently, silver clusters doped with 3d transition metals have been subjected to systematic experiments to measure the reactivity of the clusters toward molecular oxygen.^[45,46] These studies, which focused on cationic species, found that $\text{Ag}_{16}\text{Sc}^+$, $\text{Ag}_{15}\text{Ti}^+$, Ag_{14}V^+ , $\text{Ag}_{11}\text{Fe}^+$, $\text{Ag}_{10}\text{Co}^+$, and Ag_9Ni^+ exhibit a reactivity minimum in size-dependent measurements of the reaction rate coefficients. Reactivity measurements were thus confirmed to be able to identify magic clusters that are stable owing to the 18-e rule, which was consistent with previous photofragmentation experiments.^[37,38]

The present thesis extends reactivity measurements to anionic species of 3d-transition-metal-doped silver clusters, Ag_NM^- , where the size-dependent reactivity of the anions toward O_2 is systematically investigated for all the 3d transition metals, $\text{M} = \text{Sc} - \text{Ni}$. The present study aims to further examine the electron-counting effect on the localization/delocalization of 3d electrons by comparing the reactivities of two isoelectronic systems, namely, Ag_NM^- and $\text{Ag}_{N+2}\text{M}^+$. While Ag_NM^- and $\text{Ag}_{N+2}\text{M}^+$ are isoelectronic, their geometric structures are different because the former has two fewer Ag atoms. In this regard, the present study also addresses how the endo- vs. exohedral geometry of the dopant affects localization/delocalization of the 3d electrons in Ag_NM^- and $\text{Ag}_{N+2}\text{M}^+$. In addition to the reactivity measurements, the author performed photoelectron imaging (PEI) spectroscopy to directly probe the electronic structure of Ag_NM^- with the aid of DFT calculations.

The present thesis is organized as follows: Chapter 2 describes the design of the whole experimental apparatus and the computational methods. In Chapter 3, the reaction kinetics of Ag_NM^- ($\text{M} = \text{Sc} - \text{Ni}$) are studied, where the reactivities of the clusters toward oxygen molecules are investigated along with DFT calculations to discuss the effects of doping on reaction pathways. Chapter 4 examines the size-dependent reactivities of Ag_NM^- to discuss electron-counting and geometric effects on the delocalization of 3d electrons. In Chapter 5, the electronic structures of Ag_NCo^- are revisited by comparing the simulation of PES by theoretical calculations with previous photoelectron spectra for the clusters.^[47] In Chapter 6, PEI results for Ag_NM^- ($\text{M} = \text{Sc}$, Ti , and V) are presented to examine their electronic structures alongside DFT calculations. Finally, some concluding remarks are given in Chapter 7.

Chapter 2. Experimental and Computational Procedures

2.1. Reactivity experiment

Figure 2.1 shows a schematic of an experimental apparatus for investigating reactions of size-selected metal clusters toward small molecules in the gas phase. It consists of a source chamber, octopole ion guides, ion deflectors, a quadrupole mass filter, a linear ion trap, and a reflectron time-of-flight mass spectrometer. The base pressure is $\sim 10^{-5}$ Pa in the whole apparatus, which is evacuated by turbo molecular pumps and rotary pumps.

2.1.1. Metal cluster ion source

A magnetron-sputter cluster-ion source^[48] was employed to produce transition-metal-doped silver cluster anions, Ag_nM^- ($\text{M} = \text{Sc-Ni}$). Figure 2.2 shows a schematic of the ion source. A sputter target (Fig. 2.2B) was mounted on a magnetron head (Fig. 2.2A). The target consisted of a silver plate (diameter: 50.4 mm, thickness: 5 mm) with two holes (diameter: 8 mm) and a transition metal plate (diameter: 50.4 mm, thickness: 3 mm) (99.99%, Kojundo Chemical Laboratory Co., Ltd.), where the former was placed over the latter. They were sputtered by Ar^+ atoms generated by discharge between the target and a grounded magnetron head, where an argon-gas flow was continuously introduced from gas inlets (Fig. 2.2C). The magnetron ion source was cooled by liquid nitrogen flowing in a liquid nitrogen jacket (Fig. 2.2D). Silver atoms and transition-metal atoms were liberated into an aggregation cell, where clustering was encouraged by a buffer helium gas cooled by liquid nitrogen. Typical flow rates of the argon and helium gases were ~ 200 and ~ 150 sccm (standard cubic centimeter per minute), respectively, controlled by mass flow controllers (EL-FLOW Base, Bronkhorst High-Tech B.V.). Resultant cluster ions exited through an aperture (Fig. 2.2E) as an ion beam.

2.1.2. Ion guide, ion deflector, and mass selector

Three octopole ion guides were used to transport the cluster ions. Alternating current (AC) voltages with a peak-to-peak amplitude of ~ 700 V at a frequency of ~ 1.5 MHz were applied to 8 rods, where the phases of the neighboring rods are opposite with each other. Two ion deflectors were used to bend the cluster-ion beam by 90 degrees, which selected only negatively charged clusters. A quadrupole mass selector (MAX-16000 or MAX-4000, Extrel CMS) was employed for size-selection of Ag_NM^- .

2.1.3. Linear ion trap

A linear ion trap was used to store Ag_NM^- for a certain period to investigate reactions of the clusters and gaseous O_2 . Figure 2.3 shows a schematic of the ion trap. It consists of 30-cm-long quadrupole ion guides with entrance and exit electrodes. The ion trap was filled with a buffer He gas of 0.3 Pa and a pressure-controlled O_2 gas. The partial pressures of a buffer He gas and an O_2 gas were measured by a residual gas analyzer (RGA 100, Stanford Research Systems, Inc.) outside the reaction cell. The pressures inside the reaction cell were calibrated by referring to the reaction rate coefficients of $\text{Co}_N^+ + \text{O}_2$ reported previously.^[49] First, direct current (DC) voltages of +2, +9, and +13 V were applied to the entrance electrode, the ion guides, and the exit electrode, respectively, so that cluster anions can pass through the ion trap as shown in Fig. 2.3(A). Size-selected clusters were decelerated by collision with He atoms at room temperature in the ion trap. Then, the clusters can be stored when the voltage of the exit electrode switched from positive to negative as shown in Fig. 2.3B. The net voltage of the entrance electrode was -7 V for the clusters in the trap because the potential of the ion guide was +9 V. Thus, it is difficult for the cluster anions to exit through the entrance electrode as well as the exit electrode. After the trap was filled with the ions, a negative voltage was applied to the entrance electrode so that no more ions were introduced into the trap as shown in Fig. 2.3C. The clusters were stored for a variable time for reaction with O_2 molecules. Product ions were extracted from the ion trap by applying a positive

voltage to the exit electrode (Fig. 2.3D).

2.1.4. Reflectron time-of-flight mass spectrometer

A reflectron time-of-flight (TOF) mass spectrometer^[50] was employed to identify ions extracted from the ion trap. The TOF apparatus consists of three components: an accelerating part, a reflecting part, and a detecting part. The accelerating region has been described in detail in the report by Sarugaku *et al.*^[51] Briefly, the ions were accelerated with ~ -2 kV pulsed voltage generated by a DC power supply (MPOD Mini create, Wiener, Inc.). The accelerating voltage was switched by a fast high-voltage transistor switch (HTS41-06-GSM, BEHLKE, Inc.) after ions were extracted from the ion trap. The timing of the switch was controlled by a delay generator (DG 645, Stanford Research Systems, Inc.).

The reflectron region have been improved recently and described in the report by Handa *et al.*^[52] Figure 2.4 shows a schematic of the reflector. Briefly, it consists of an eyeglasses-frame electrode (Fig. 2.4A) and an electrode with two through-holes (Fig. 2.4B) mounted in front of a stack of reflecting electrodes (Fig. 2.4C) that are negatively biased to reflect incoming anions. The electrode with two through-holes was grounded, whereas a positive voltage was applied to the eyeglass-frame electrode to converge outgoing ion beam on an ion detector. The high voltages for the eyeglass-frame electrode and the stack of reflecting electrodes were supplied by a DC power supply (MPOD Mini create, Wiener, Inc.).

Ions were detected by a dual microchannel plate (MCP: F4655-14, Hamamatsu Photonics). The signals from the MCP detector were amplified by a preamplifier (SR445A, Stanford Research Systems, Inc.) and were recorded by a 500-MHz oscilloscope (HDP5054, Teledyne LeCroy). The TOF mass spectra were accumulated for 256 cycles of trap and detection.

2.2. Anion photoelectron imaging

Figure 2.5 shows a schematic of the apparatus for photoelectron velocity map imaging on size-selected Ag_NM^- . The procedures of generation and mass-selection of Ag_NM^- were the same as described in subsections 2.1.1 and 2.1.2. After size selection, an anion beam of Ag_NM^- entered the potential switch^[53] held at +600 V, which was driven by a high voltage pulser (PVX-4140, DEI). The high voltage was then switched to ground while the clusters are traveling inside, which produced the cluster beam with a 0.6-keV kinetic energy with respect to ground. A typical pulse width and switching frequency of the +600 V pulse were adjusted to $\sim 5 \mu\text{s}$ and $\sim 0.1 \text{ MHz}$, respectively, meaning that the continuous size-selected cluster beam was converted into quasi-continuous after the potential switch. The quasi-continuous anion bunches were then focused with two sets of Einzel lens, and finally introduced into an assembly of photoelectron accelerating electrodes with velocity map imaging (VMI) configuration^[54]. The voltages of the potential switch and the Einzel lenses were supplied by DC power supplies (PWR400H, Kikusui and MPOD Mini create, Wiener, Inc., respectively). The clusters through the VMI were detected by a Faraday cup (F. C.), where the ion current was typically $\sim 5 \text{ pA}$.

The design of VMI electrodes followed a novel setup proposed by Verlet and co-workers.^[55] It consists of repeller, extractor, and ground electrodes, which are plated by gold to suppress secondary electrons from the surface of electrodes by irradiation of CW laser. The extractor and ground electrodes have a through-hole to allow photoelectrons to pass through and to create an electrostatic field for VMI. A resistive glass tube (PHOTONICS) is placed between the extractor and the ground electrodes. The DC voltages of the repeller and the extractor are set to -100 V supplied by DC power supplies (PLJ650-0.1 and PLE-650-0.1, Mastusada).

A CW diode laser (MDL-III-405nm-1W-BL23078, Changchun New Industries Optoelectronics Tech. Co., Ltd) was employed for a photodetachment laser source, which was operated at 404 nm (3.07 eV) with the laser power of about 400 mW. The laser

beam was introduced to the VMI electrodes, where it crossed with the quasi-continuous cluster beam. Then, photoelectrons were detached from cluster anions and were accelerated toward a dual MCP detector (F1217-01, Hamamatsu Photonics, effective diameter = 40 mm ϕ) backed with a phosphor screen (P43). A CMOS camera (CS165MU1/M, 1440 \times 1080 pixels, Thorlabs) captured a projected image of their three-dimensional distribution on the phosphor screen. The CMOS camera acquired the projected photoelectron image for 500 ms and the image acquisition was repeated for 500–1000 times to achieve an acceptable signal to noise ratio by accumulating the images. With the CW laser beam off, a certain number of secondary electrons, generated by collisions of the incident anions with inner walls of electrodes for the photoelectron acceleration, were observed in the image. Therefore, a laser-on image was subtracted by a laser-off background image recorded for the same accumulation.

2.3. Quantum chemical calculation

DFT calculations were performed by the Gaussian 16 package^[56] to explore optimized geometric and electronic structures of Ag_NM^- as well as Ag_NM^+ . The author employed the B3LYP * ^[57] functional with the basis sets of 6-311++G(d,p)^[58] for transition-metal atoms and LanL2DZ for Ag atoms with the corresponding effective core potential^[59]. Only for Ag_7Ni^- , B3LYP functional were used to explain the experimental result. A frozen core was assumed for 28 inner-shell electrons of each Ag atom. Initial geometries for optimization were generated by replacing non-equivalent Ag sites in $\text{Ag}_{N+1}^{+/-}$ clusters with a dopant atom, where possible symmetries were assumed for each undoped Ag cluster. The basis sets were chosen by referring to the previous report on Ag_NM^+ , where computational results obtained by the LanL2DZ basis set were found to be essentially the same as those by higher-level calculations using def2-TZVPP with triple- ζ quality in terms of geometry, spin multiplicity, and s–d orbital mixing.^[46] The relative energies were corrected for zero-point-energy contributions. The local magnetic moment on the transition metal atom was obtained by the natural bond orbital

(NBO) analysis^[60] using the NBO 3.1 program.^[61]

Photoelectron spectra of Ag_NM^- were simulated by a procedure described by Yin and Bernstein^[62] as follows. After geometry optimization and total-energy calculation of Ag_NM^- , the total energy of corresponding neutral, Ag_NM , in the same geometry was calculated for spin states of $M_S \pm 1$ allowed for final states of single-photon photodetachment, where $M_S (= 2S + 1)$ is the spin multiplicity of Ag_NM^- . The lowest electron binding energy (EBE) was obtained as a total-energy difference between the initial anion in M_S and the final-state neutral either in $M_S + 1$ or $M_S - 1$. The lower one of these EBE is the vertical detachment energy (VDE). TDDFT calculations were performed for the neutral clusters to obtain one-electron excitation energies for each spin state, which were added to the lowest EBE to evaluate higher EBEs corresponding to excited final states. The simulations of photoelectron spectra were obtained by convolution of each EBE with a Gaussian profile with 0.3-eV full-width at half-maximum (FWHM).

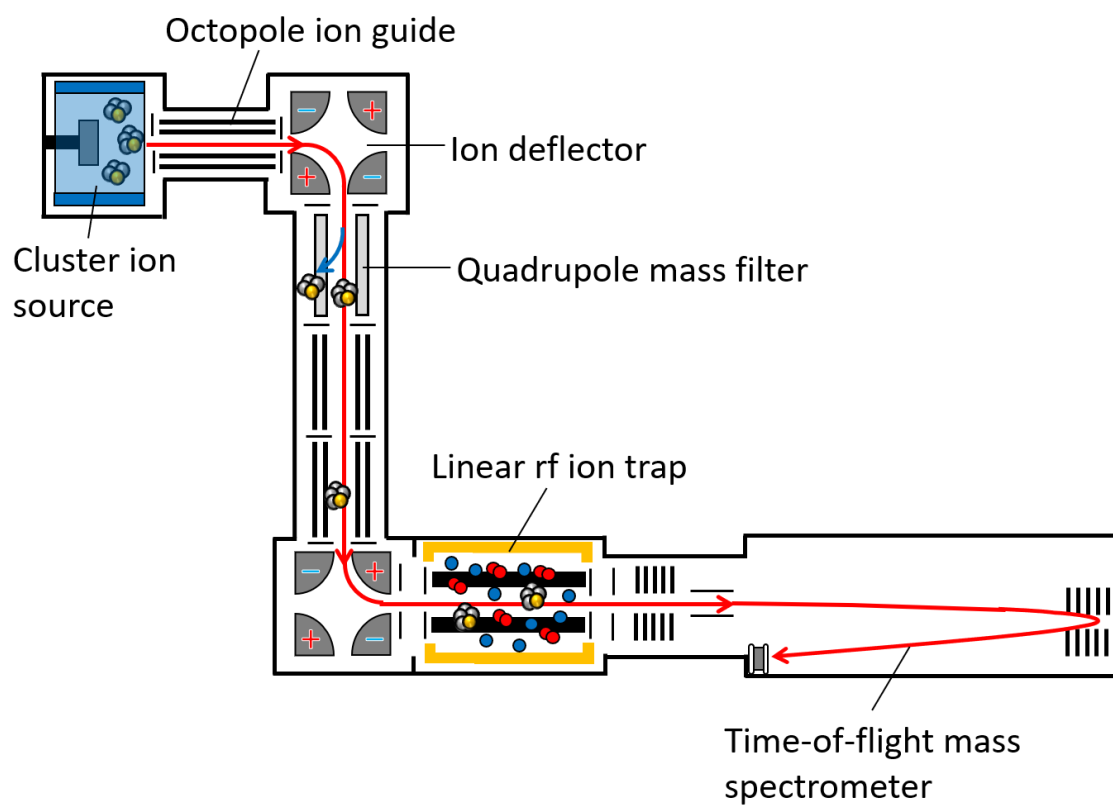


Figure 2.1. A schematic of an experimental apparatus for reaction studies.

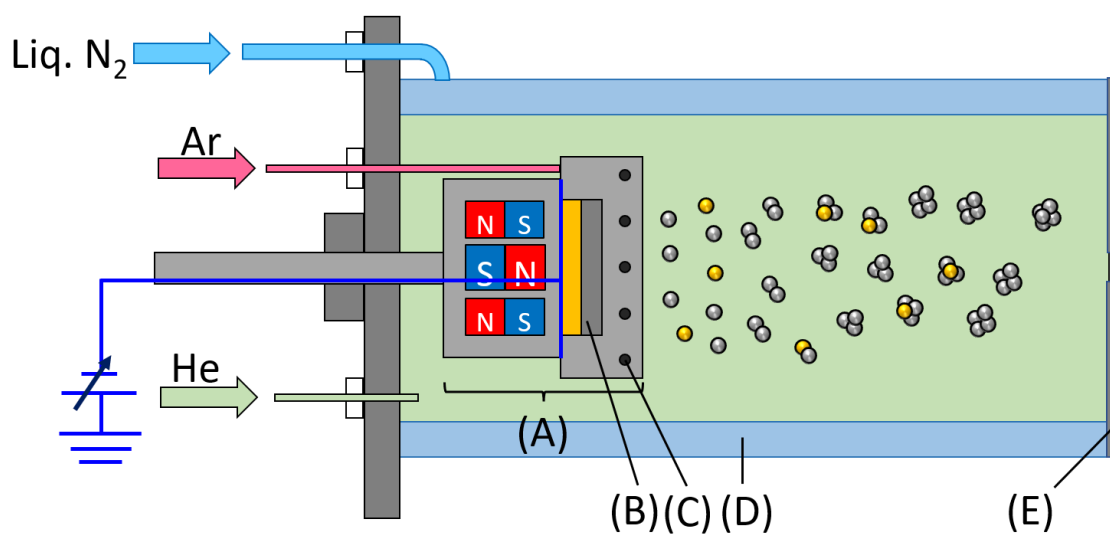


Figure 2.2. A schematic of a metal cluster ion source: (A) a magnetron head, (B) metal targets, (C) Ar-gas inlets, (D) a liquid nitrogen jacket, and (E) an aperture

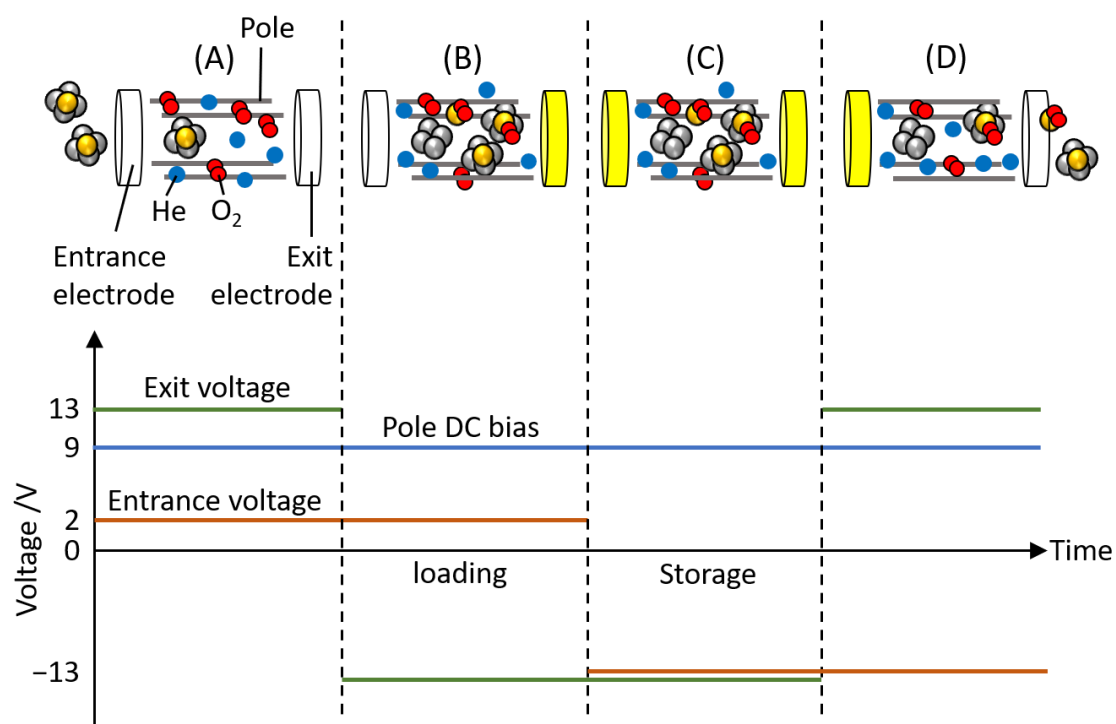


Figure 2.3. Procedures of an ion-trap operation for reaction: (A) preloading time, (B) loading time, (C) storage time, and (D) extraction from the ion trap. The diagram shows voltages for pole, entrance, and exit electrodes as a function of time. Green, blue, and red lines represent applied voltage for exit, pole, and entrance electrodes, respectively.

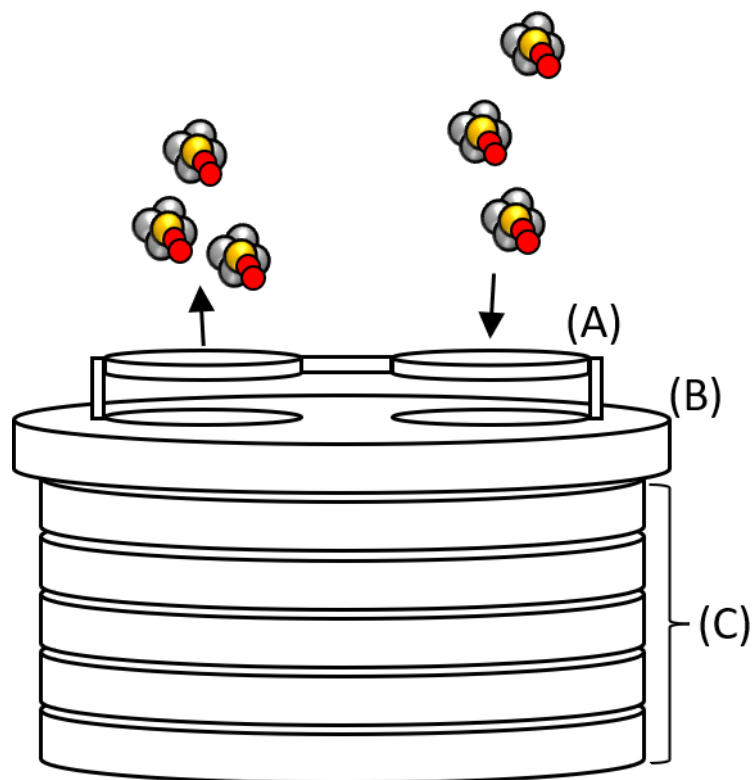


Figure 2.4. A schematic of an ion reflector. (A) An eyeglasses-frame electrode. (B) A grounded electrode with two holes. (C) A stack of cylindrical electrodes.

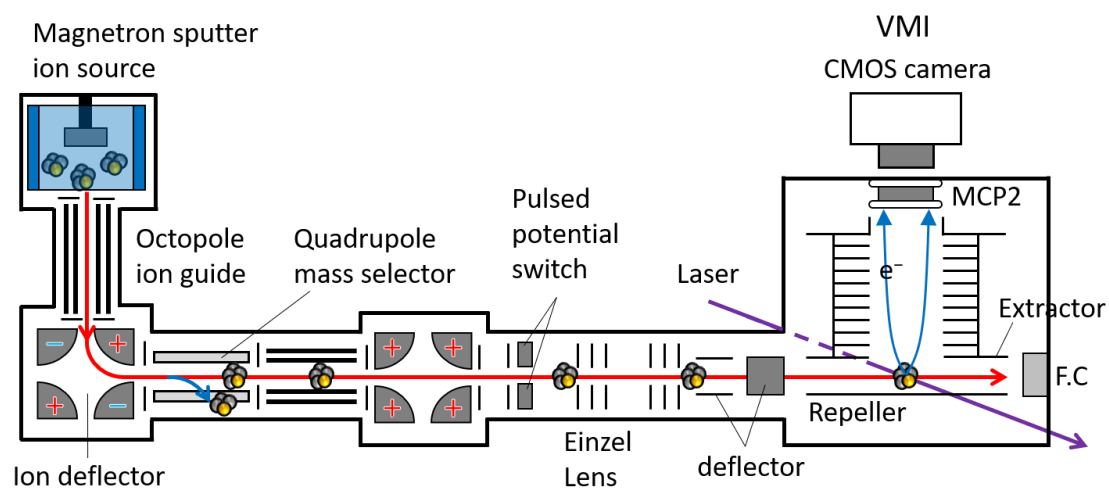


Figure 2.5. Experimental setup for velocity map imaging of photoelectrons.

Chapter 3. Reaction Kinetics

3.1. Introduction

A reaction kinetics study of clusters is the standard method for investigating their electronic and geometric structures to reveal the origins of their size-dependent properties. Gas phase reactions have been investigated for a wide variety of metal clusters. For example, a reaction study on Co_N^+ with CO was performed by Guo *et al.*^[63] They used extended Hückel calculations to predict bonding capacities and structures. For $N = 4$, $\text{Co}_4(\text{CO})_{12}^+$ was observed as the final product, which was expected to form tetrahedral Co_4 by X-ray crystallography.^[64] Their theoretical calculations predicted that the structure of $\text{Co}_4(\text{CO})_{12}$ has 60 valence electrons, which consist of valence electrons of Co and two electrons from each CO molecule. This suggests that Co_4^+ has a tetrahedral geometry. For $N = 5$, the coordination reactions of CO were observed to terminate at $\text{Co}_5(\text{CO})_{14}^+$, which has 72 valence electrons to form a closed electronic shell. By comparing the number of valence electrons with the theoretical result, they predicted that Co_5^+ would have a trigonal bipyramidal. Thus, it is possible to predict a geometric structure by analyzing the reaction products. Geometries of other metal clusters have been revealed by similar reaction studies.^[65–67]

Since the electronic and geometric structures of the clusters are modified when doped with a heteroatom,^[35,36,46,68] the reaction procedures for doped clusters must be different from those for pure clusters. In a previous theoretical study, M@Pt core-shell particles for 3d, 4d, and 5d late transition metal atoms were reported to facilitate O_2 dissociation because favorable distortions of the shell's Pt(111) facet induces binding of the O_2 with the particle.^[69] For NiPd alloy clusters, theoretical calculations revealed that the Ni-doped Pd clusters Pd_3Ni and Pd_2Ni_2 lower the activation energy for O_2 dissociation with respect to the Pd_4 cluster.^[70] Recently, the size-dependent reactivity of Ag_MM^+ ($M = \text{Sc–Ni}$) toward O_2 was reported.^[46] In this study, Ag_NNi^+ produces $\text{Ag}_N\text{NiO}_2^+$ ($N' < N$) as the main products for $N \leq 8$ in contrast to Ag_N^+ because the doped Ni, rather than

Ag, serves as the active site. Thus, the geometric structure affects the reaction kinetics and, in addition, heteroatom doping opens various reaction pathways that are not found in pure clusters.

This chapter presents the reactions of Ag_NM^- with O_2 molecules to examine the doping effects on Ag_N^- , focusing on size- and dopant-dependent reaction pathways.

3.2. Results

Details of experimental and theoretical procedures have been described in Chapter 2. Figure 3.1 shows the mass spectra of clusters produced in the cluster-ion source. Ag_NM^- marked by color bars were produced for $N = 4\text{--}18$ as well as Ag_N^- . Since the number of dopants depends on the size and number of holes on the silver target and the condition of the source, these parameters were adjusted to optimize single-atom doping. The optimized parameters were used, but small amounts of Ag_NM_2^- were produced as marked by asterisks. However, Ag_NM_3^- may not be contaminating Ag_NM^- because the Ag_NM^- peaks have no shoulders.

3.2.1. Reaction products

Figures 3.2–3.9 show TOF mass spectra of ions produced in the reaction of Ag_NM^- ($M = \text{Sc--Ni}$) with O_2 . All ions from the trap are accelerated by a high voltage to gain a kinetic energy, E . Thus, the velocity, v , of these ions is given by $v = \sqrt{2E/m}$, where m is the mass of the ions. After acceleration, the ions travel the same distance, L , and so, the flight time, t_{fl} , can be expressed as $t_{\text{fl}} = \frac{L}{v} = \frac{L}{\sqrt{2E}}\sqrt{m}$. Therefore, the mass associated with each peak in the TOF mass spectra is calculated by the equation

$$\frac{t_{\text{fl},i}}{t_{\text{fl},0}} = \sqrt{\frac{m_i}{m_0}}, \quad (3.1)$$

where $t_{\text{fl},i}$ is the flight time of the ions, $t_{\text{fl},0}$ is the flight time of the reactant ion, m_i is the mass of ions, m_0 is the mass of the reactant ion, and i labels the peak.

M = Sc. Figure 3.2 shows TOF mass spectra of ions produced in the reaction of Ag_NSc^- with O_2 . Main reaction products were subject to fragmentation at $N \leq 13$. For example, Ag_4Sc^- produced ScO_2^- , ScO_3^- , Ag^- , AgScO_2^- , Ag_2ScO^- , $\text{Ag}_2\text{ScO}_2^-$, and Ag_3^- , as shown in Fig. 3.2(a). These clusters were formed by adsorption and subsequent dissociation via an intermediate cluster, $\text{Ag}_4\text{ScO}_2^-$, which was not observed in the mass spectrum. These clusters can be categorized into Ag-free, Sc-free, and oxide fragment products. The three types of dissociation products were observed up to $N = 13$ as shown in Figs. 3.2(b)–(j). Ag-free ScO_L^- ($L = 2-4$) were observed below $N = 8$. Sc-free $\text{Ag}_{N'}^-$ ($N' < N$) were produced at $N = 4-7, 12$, and 13 . $\text{Ag}_{N'}^-$ with an odd N' were mainly formed owing to the stability of the singlet state. For these sizes, the main products were $\text{Ag}_N\text{ScO}_L^-$ ($L = 2, 3, 4$) for $N \leq 13$. At $N = 14$, no product ions were observed, as shown in Fig. 3.2(k). As the size increased above $N = 15$, the main products changed from fragmentation ions to oxygen adducts. Ag_NSc^- reacted with several O_2 molecules to produce $\text{Ag}_N\text{ScO}_{2m}^-$ ($m = 1-4$).

M = Ti. Figure 3.3 shows TOF mass spectra of ions produced in the reaction of Ag_NTi^- with O_2 . The dissociation products were observed for $N \leq 12$. Similarly to Ag_NSc^- , Ag-free, Ti-free, and oxide fragments were formed by O_2 adsorption and subsequent dissociation via $\text{Ag}_N\text{TiO}_2^-$, which was not observed in the mass spectra, as shown in Figs. 3.3(a)–(i). Ag-free TiO_L^- were produced below $N = 7$. Major products were $\text{Ag}_N\text{TiO}_L^-$ in the small sizes. As the size increased up to $N = 13$, oxygen adsorption was the major reaction channel, rather than fragmentation reaction pathways.

M = V. Figure 3.4 shows TOF mass spectra of ions produced in the reaction of Ag_NV^- with O_2 . The dissociation products were observed for $N \leq 11$. The three types of products described above were formed by O_2 adsorption and subsequent dissociation via the intermediate Ag_NVO_2^- , which were not observed in the TOF mass spectra. Ag-free VO_L^- were produced below $N = 8$, as shown in Figs. 3.4(a)–(d). In the case of $N =$

12 and 13, small amounts of products were observed. As the size increased up to $N = 14$, oxygen adducts were the major products, instead of fragmentation products.

M = Cr. Figure 3.5 shows TOF mass spectra of ions produced in the reaction of Ag_NCr^- with O_2 . The dissociation ions were mainly observed for $N \leq 13$, except for $N = 12$. The three types of products were formed by the adsorption of O_2 and subsequent dissociation via $\text{Ag}_N\text{CrO}_2^-$, which were not observed in the TOF mass spectra. Ag-free CrO_L^- were produced for $N = 5-9$. The major products at these sizes were $\text{Ag}_{N'}\text{CrO}_L^-$ with an odd N' . Small amounts of Cr-free Ag_3^- and Ag_7^- were observed in the reaction of Ag_5Cr^- and $\text{Ag}_{10}\text{Cr}^-$ in Figs. 3.5(a) and (f), respectively. These Cr-free products have an even number of valence electrons. For $N = 12$ and $N \geq 14$, the major reaction channel is the adsorption of oxygen. The dissociation products were also observed for these large sizes, in contrast to the reaction of Ag_NM^- ($M = \text{Sc-V}$) with O_2 .

M = Mn. Figure 3.6 shows TOF mass spectra of ions produced in the reaction of Ag_NMn^- with O_2 . The dissociation products were formed for $N \leq 12$. No Mn-free Ag_N^- were observed for any size, whereas AgO^- was produced for $N = 5-9$. Ag-free MnO_L^- and oxide fragments were observed in the same manner as in the reactions of Ag_NM^- discussed above. These product ions were formed by the adsorption of O_2 and subsequent dissociation via the intermediate $\text{Ag}_N\text{MnO}_2^-$, which were not observed in the TOF mass spectra. Ag-free MnO_L^- were produced below $N = 9$. The major products were oxygen adducts at above $N = 13$.

M = Fe. Figure 3.7 shows TOF mass spectra of ions produced in the reaction of Ag_NFe^- with O_2 . The dissociation products were observed for $N \leq 11$, which were formed by the adsorption of O_2 and subsequent dissociation via the intermediate $\text{Ag}_N\text{FeO}_2^-$. Oxidized dissociation products, $\text{Ag}_{N'}\text{FeO}_L^-$, were formed as the major products for all small sizes, while Ag-free FeO_2^- were observed only for $N = 6$. Fe-free

Ag_N^- were not detectable in the mass spectra. For $N = 12$ and 13 , both oxygen adducts and dissociation products were produced. As the size increased above $N = 14$, oxygen adsorption was the major reaction channel, rather than dissociation.

M = Co. Figure 3.8 shows TOF mass spectra of ions produced in the reaction of Ag_NCo^- with O_2 . The dissociation products were observed for $N \leq 11$. The three types of products explained in the subsection “M = Sc” were formed by the adsorption of O_2 and subsequent dissociation via the intermediate $\text{Ag}_N\text{CoO}_2^-$, which were not detected in the TOF mass spectra. Ag-free CoO_2^- was observed only for $N = 4$. Co-free Ag_N^- and Ag_2O_2^- were produced. $\text{Ag}_N\text{CoO}_2^-$ were observed as the major products for these small sizes. For $N = 12$, an oxygen adduct, $\text{Ag}_{12}\text{CoO}_2^-$, was produced as well as the dissociation ion $\text{Ag}_{11}\text{CoO}_2^-$. As the size increased above $N = 13$, oxygen adsorption was the major reaction channel, rather than dissociation.

M = Ni. Figure 3.9 shows TOF mass spectra of ions produced in the reaction of Ag_NNi^- with O_2 . The dissociation channels were the major reaction for $N \leq 12$, similarly to clusters doped with other transition metals. Ag-free, Ni-free, and oxidized dissociation products were formed by O_2 adsorption and subsequent dissociation via $\text{Ag}_N\text{NiO}_2^-$, which was not detected in the TOF mass spectra. Ag-free NiO_2^- was observed for $N = 3$ and 4 . Further oxidized products, $\text{Ag}_N\text{NiO}_{L'}^-$ ($L' > 2$), could not be observed, unlike with the other dopant metals. For $N = 13$ and 14 , oxygen adducts were produced as the major products.

3.2.2. Simulation of reaction kinetics

This subsection reports the reaction pathways for Ag_NCo^- and Ag_NNi^- . To obtain the intensity of each ion, each TOF mass spectrum was fitted by the function

$$I = \sum_i a_i \left(\frac{1}{e^{b_1(T-c_i)} + e^{-b_2(T-c_i)}} \right)^2, \quad (3.2)$$

where I is the ion signal of the TOF mass spectrum, T is the time elapsed after the acceleration of ions measured at the ion detector, c_i is the flight time of each ion, a_i , b_1 , and b_2 are fitting parameters, and i labels the ions. Eq. (3.2) gave a better fitting than the Gaussian function because Eq. (3.2) reproduces asymmetric peaks of the mass spectra. The intensity for each ion was determined by integrating the corresponding fitting curve of the peak area. Figures 3.10 and 3.11 show the abundance ratios of the reactants and products for Ag_NCo^- and Ag_NNi^- , respectively, as a function of storage time, t_{st} . The kinetics data were fitted to rate equations using a program coded by referring to the DETMEC software.^[71] The software uses the Simplex algorithm, which optimizes the rate constant of each reaction step by the least-squares method, and the Runge-Kutta-Nyström method, which simulates fitting curves to reproduce experimental data. The present reactions proceed by a pseudo-first-order process because the reaction gas cell was filled with O_2 and He gases at constant partial pressures that were sufficiently higher than the concentration of the reactant clusters. All possible reaction pathways were examined to determine the most probable one. The solid lines in Figs. 3.10 and 3.11 show data fitting obtained for the differential equations based on the reaction pathways shown in Tables 3.1 and 3.2, respectively.

M = Co. Figure 3.10 shows the abundance ratios of each ion produced in the reaction of Ag_NCo^- as a function of t_{st} , plotted with solid circles. Note that product ions were observed at $t_{\text{st}} = 0$, which were produced during the loading time of the reactant ions. The reactant cluster, Ag_NCo^- , shown by red circles, disappears exponentially with storage time, while product ions are formed. The solid curves in each panel of Fig. 3.10 show data fitting obtained for pseudo-first-order differential equations based on the reaction pathways listed in Table 3.1. The reaction pathways revealed that successive dissociation reactions occur for most of the sizes of $N = 5, 7, 10$, and 11 . Product ions are formed directly from the reactant except for Ag_3^- at $N = 6$ and $\text{Ag}_5\text{CoO}_{2,4}^-$ at $N = 8$ and 9 . $\text{Ag}_5\text{CoO}_4^-$ are produced by O_2 adsorption to the dissociation product, $\text{Ag}_5\text{CoO}_2^-$.

Ag_NCo^- at $N \leq 7$ released a maximum of four Ag atoms in the reaction, whereas Ag_NCo^- for $N = 8-12$ dissociated into two Ag atoms at maximum. Ag_NCo^- and $\text{Ag}_N\text{CoO}_2^-$ are almost in equilibrium at $N = 13$, where oxygen adsorption is the major reaction channel and the rate constant for further adsorption, $k_3(\text{Co}, 13)$, is smaller than that of adsorption back to $\text{Ag}_{13}\text{Co}^-$, $k_2(\text{Co}, 13)$.

M = Ni. Figure 3.11 shows the abundance ratio of each ion produced in the reaction of Ag_NNi^- as a function of t_{st} , plotted with solid circles. Note that the products observed at $t_{\text{st}} = 0$ were formed during the loading time of the reactant ions. The reactant cluster, Ag_NNi^- , shown by red circles, disappears exponentially with storage time. The solid curves in each panel of Fig. 3.11 show data fitting obtained for the rate equations based on the reaction pathways listed in Table 3.2. In contrast to Ag_NCo^- , successive dissociation reactions occur only for $N = 11$. As the size increased, the maximum number of released Ag atoms decreased from four to one. In the large size range, *i.e.*, $N = 13$ and 14, where the oxygen adducts are the major products, Ag_NNi^- and $\text{Ag}_N\text{NiO}_2^-$ are almost in equilibrium.

3.2.3. Geometric structures

The author explored the geometric structures of Ag_NM^- to investigate the location of the dopant in the clusters, which may affect the reaction pathways. The optimized geometric structures of 18-valence-electron clusters for $\text{M} = \text{Sc-Ni}$ are shown in Fig. 3.12, along with spin multiplicity and symmetry. The results for $\text{Ag}_{14}\text{Sc}^-$ revealed that the most stable isomer has a D_{6d} symmetry, with the Sc atom fully encapsulated by Ag atoms. The most stable isomer is in the singlet state, which is 1.2 eV lower than the triplet state. This is similar to the results for $\text{Ag}_{14}\text{Ti}^{[72]}$ and $\text{Ag}_{14}\text{V}^{+[44,68,73]}$ reported in previous theoretical studies. $\text{Ag}_{13}\text{Ti}^-$ showed an endohedral geometry with C_{3v} , which is also in the singlet state. The most stable cluster is lower than the triplet and quintet states by 0.6 and 1.7 eV, respectively. Ag_{12}V^- also has an

endohedral geometry with I_h symmetry. The singlet state is the most stable isomer, which is lower than the triplet and quintet states by 0.3 and 0.8 eV, respectively. On the other hand, $\text{Ag}_{11}\text{Cr}^-$, $\text{Ag}_{10}\text{Mn}^-$, Ag_9Fe^- , Ag_8Co^- , and Ag_7Ni^- exhibited exohedral geometries with open electronic structures.

3.3. Discussion

3.3.1. Reaction site

For all doped clusters, dissociation via the intermediate Ag_NMO_2^- is the major reaction channel for small sizes. This contradicts the results for the reaction of Ag_N^- with O_2 reported in a previous study, where an O_2 molecule was adsorbed on Ag_N^- without fragmentation.^[74] As reported in the Results section above, Ag-free MO_L^- were observed as one of the dissociation products. The analyses of reaction kinetics for Ag_NCo^- and Ag_NNi^- imply that the products were formed by the release of N Ag atoms from the intermediate Ag_NMO_2^- , as listed in Tables 3.1 and 3.2. This indicates that the O_2 molecule is adsorbed on the dopant atom, which acts as an active site. Another type of product, M-free $\text{Ag}_{N-N'}^-$, corroborates this finding because the products were formed by the release of $\text{Ag}_{N-N'}$ and MO_2 , as revealed by the reaction pathways for Ag_6Co^- and $\text{Ag}_{11}\text{Ni}^-$. Since Ag- and M-free products were observed for Ag_NM^- ($\text{M} = \text{Sc} - \text{Fe}$) as well, an active site in those clusters may be the dopant atom, as in Co- and Ni-doped clusters. This hypothesis is supported by DFT calculations. As shown in Fig. 3.12, the dopant atom is located on the cluster at small sizes, *e.g.*, $\text{Ag}_{11}\text{Cr}^-$, $\text{Ag}_{10}\text{Mn}^-$, Ag_9Fe^- , Ag_8Co^- , and Ag_7Ni^- . The geometric feature was also found for Ag_NM cations^[44–46,73,75] and neutrals^[72,76–83], which have an exohedral dopant at small sizes. The previous DFT calculations for Ag_NIrO_2 revealed that an oxygen atom adsorbed on Ir at the surface, where the adsorption energy of O_2 is larger than that on pure Ag_N .^[83] Thus, the dopant M serves as an active site, where a large amount of excess energy is produced by the adsorption of an O_2 molecule to dissociate Ag_NMO_2^- .

On the other hand, large clusters produced oxygen adducts, Ag_NMO_L^- , as the

major products, similarly to the reaction products of Ag_N^- . The geometric structures in Fig. 3.12 show that the dopant atom is encapsulated by Ag atoms as the number of Ag atoms increases, indicating that Ag atoms may act as reaction sites. This is consistent with a previous study, where an O_2 molecule was adsorbed on the surface Ag atoms in the case of endohedral Ag_NIr .^[83] Therefore, the reaction site changes from the dopant M to Ag atoms for the large sizes, owing to dopant encapsulation.

3.3.2. Formation of reaction products

As mentioned in the previous section, the dissociation products suggest that the binding energy of O_2 to the M atom is sufficiently large to promote dissociation. The three types of products, *i.e.*, Ag-free MO_L^- , M-free $\text{Ag}_{N'}^-$, and Ag_NMO_L^- , were observed in the small size range. The analysis of reaction pathways for Ag_NCo^- and Ag_NNi^- revealed that the major products, Ag_NMO_2^- , were formed directly by the release of $\text{Ag}_{N-N'}$ from the reactant via the intermediate, Ag_NMO_2^- , as summarized in Tables 3.1 and 3.2. The types of product ions were the same for all the dopants, suggesting that Ag_NMO_2^- for M = Sc–Fe is produced in the same way as M = Co and Ni. Since the excess energy produced in the reaction causes cleavage of the weaker bonds in the gas phase, the formation of the dissociation products may be explained by comparison of the bond energies, D , of M–O, Ag–Ag, and Ag–M. These values have been determined by experimental^[84] and theoretical^[72,78–81,83] studies for cationic and neutral clusters. An experimental study reported that the $D(\text{M}^+-\text{O})$ values for M = Sc, Ti, and V were 6.9, 6.93, and 6.0 eV, respectively, while those for M = Cr, Mn, and Fe were comparatively lower: 3.72, 2.95, and 3.53 eV, respectively.^[84] Theoretical calculations showed that $D(\text{Ag–M})$ is between 1.4 and 2.5 eV for M = Sc,^[81] Ti,^[72] and V^[80], which is higher than $D(\text{Ag–Ag})$,^[78–81,83] which has been reported to be between 0.9 and 1.9 eV. Thus, it appears that the strong interaction between the dopant M and the O_2 molecule may be producing a large amount of excess energy, promoting the cleavage of Ag–Ag and Ag–M bonds. It is noted that the number of released Ag atoms is two or four, *i.e.*, $N-N' = 2$ or

4 for small sizes below $N = 7$. This suggests that the reaction pathways preferentially proceed via the release of stable neutrals because Ag_2 forms a singlet state. As the size increases, the number of released Ag atoms decreases from 4 to 1. For large sizes, the Rice–Ramsperger–Kassel theory predicts that the dissociation rate of the ion-molecular complex will be reduced owing to large vibrational degrees of freedom.^[67] In addition, previous theoretical studies have reported that the dissociation energy of Ag increased with size.^[72,80,81] Therefore, the excess energy generated during the reactions would be redistributed to vibrational energy, and not suffice for the release of several Ag atoms. The major products, Ag_NMO_2^- , can react with another O_2 molecule to form Ag_NMO_4^- , as shown in the reactions of Ag_8Co^- and Ag_9Co^- , suggesting that the adsorption energy of the second O_2 molecule to the reactant is low. On the other hand, Ag_NMO_3^- were observed, as shown in Figs. 3.2–3.7. Reaction experiments of V_n^+ , Cr_n^+ , and Fe_n^+ with O_2 have revealed that monoxide products are formed by the dissociative adsorption of O_2 .^[85–87] Theoretical calculations for Ag_NIrO_2 showed that the O_2 dissociation barriers on small clusters are much lower, ranging between 0.34 and 0.89 eV.^[83] These results suggested that Ag_NMO_3^- were produced through the release of a single oxygen atom from Ag_NMO_4^- .

Ag-free MO_L^- are produced by pathways similar to those for Ag_NMO_L^- , the former being a specific case of the latter with $N' = 0$. The reactant, Ag_NM^- , reacted with an O_2 molecule to form MO_2^- directly, as shown in Tables 3.1 and 3.2. MO_2^- reacted further with an O_2 molecule to produce MO_4^- , which released an oxygen atom to form MO_3^- in the reactions for $\text{M} = \text{Sc–Fe}$. Focusing on the dopant dependence, MO_2^- was observed up to $N = 8, 7, 8, 9, 9, 6, 4$, and 4 for $\text{M} = \text{Sc–Ni}$, respectively. It was found that the adsorption energy of O_2 to M decreased in going from the early transition metals to the late ones. This is supported by previous studies, which showed that $D(\text{M}^+-\text{O})$ decreased in going from the early transition metals to the late ones.^[84] This suggests that the dissociation reaction may favor systems doped with early transition metals.

In the case of large clusters, oxygen adducts, Ag_NMO_L^- ($L = 1, 2$, and 3),

dominate the products, rather than dissociation products. The analysis of the reaction kinetics for $M = \text{Co}$ and Ni revealed that Ag_NMO_2^- release O_2 to form the reactant Ag_NM^- at $N = 13$ and 14 , indicating that the O_2 molecule physisorbed on Ag_NM^- . The binding energies of O_2 to Ag_N^- have been reported to range between 0.18 and 1.10 eV,^[88] which is lower than those of $\text{Ag}-\text{Ag}$ and $\text{Ag}-\text{M}$. Therefore, dissociation may not be occurring because the weak interaction between reactant and O_2 produces little excess energy.

Another factor influencing the formation of reaction products is the stability of the product ions. $\text{Ag}_N\text{ScO}_2^-$ with an even N' , $\text{Ag}_N\text{TiO}_2^-$ with an odd N' , and $\text{Ag}_N\text{CrO}_2^-$ with an odd N' were mainly observed, all of which have an even number of electrons. In the reaction for $M = \text{Sc}$ and Cr , Ag_N^- with an odd N' were produced, which also have an even number of electrons. Since the electronic structure of s-electron clusters consists of discrete energy levels, an even number of electrons occupy these levels to form a singlet state.^[5,88] Thus, even-electron clusters may tend to be produced preferentially owing to stability.

3.3.3. Comparison of the reaction products of Ag_NNi^- and Ag_NNi^+

This subsection will compare the product ions in the reactions of Ag_NNi^- and Ag_NNi^+ to investigate the effect of the charge state. A previous reaction study on Ag_NNi^+ reported that dissociation channels were the major processes at $N \leq 8$.^[46] $\text{Ag}_N\text{NiO}_2^+$ were the major products in this size range. The theoretical calculations for Ag_NNi^+ revealed that the dopant Ni atoms are located on the surface of the clusters at these cluster sizes. The reaction of Ag_NNi^- is similar to that of Ag_NNi^+ . Thus, it appears that the reaction site is the Ni atom regardless of the charge state. Ag_NNi^- can liberate four Ag atoms at maximum to produce NiO_2^- for small sizes, whereas Ag_NNi^+ released three Ag atoms at maximum. Since O_2 is an electron acceptor, a negative charge accelerates reactions with O_2 .^[89] It is thus implied that the adsorption energy of O_2 on anionic clusters is larger than that on cationic clusters.

3.4. Summary

In this chapter, reaction products and kinetics were reported to investigate size-, dopant-, and charge-state-dependent effects. For all dopants, significant fragmentation was observed at small sizes, yielding products that could be categorized into Ag-free MO_L^- , M-free Ag_N^- , and Ag_NMO_L^- oxide fragments. The formation of Ag-free MO_L^- suggests that O_2 molecules adsorb on the dopant M. The theoretical calculations for Ag_NM^- showed that the M atom is located on the cluster surface in the small size range. Thus, the doped atom may act as an active site at the cluster surface. Since $D(\text{M}^+-\text{O})$ is larger than $D(\text{Ag}-\text{Ag})$ and $D(\text{Ag}-\text{M})$, the adsorption energy of O_2 to M may be sufficiently large to cleave Ag–Ag and Ag–M bonds, resulting in fragment products. The formation of Ag-free MO_L^- also showed that the maximum number of released Ag atoms decreased from 8 for M = Sc to 4 for M = Ni. $D(\text{M}^+-\text{O})$ decreased from 6.9 eV for M = Sc to 3.53 eV for M = Fe. Thus, the dissociation reaction may preferentially occur in systems doped with early transition metals. For large sizes, the main reaction channel was O_2 adsorption, rather than fragmentation. Large clusters, *e.g.*, $\text{Ag}_{14}\text{Sc}^-$, $\text{Ag}_{13}\text{Ti}^-$, and Ag_{11}V^- , showed an endohedral geometry, suggesting that the reaction site changed to Ag atoms. The binding energies of O_2 to Ag_N^- were lower than $D(\text{Ag}-\text{Ag})$ and $D(\text{Ag}-\text{M})$, and thus, the oxygen adducts Ag_NMO_2^- could not proceed to dissociation. Therefore, the reaction channels changed from fragmentation to adsorption as the size increased, because the reaction site changed from M to Ag. Comparing the reaction products of Ag_NNi^- with those of Ag_NNi^+ , the maximum number of released Ag atoms for Ag_NNi^- is larger than that for Ag_NNi^+ . Since a negative charge promotes the reaction with an electron acceptor, anionic clusters may be producing more excess energy for dissociation than cationic clusters. Thus, geometric structure, type of dopant element, and charge state all affect the reaction channels.

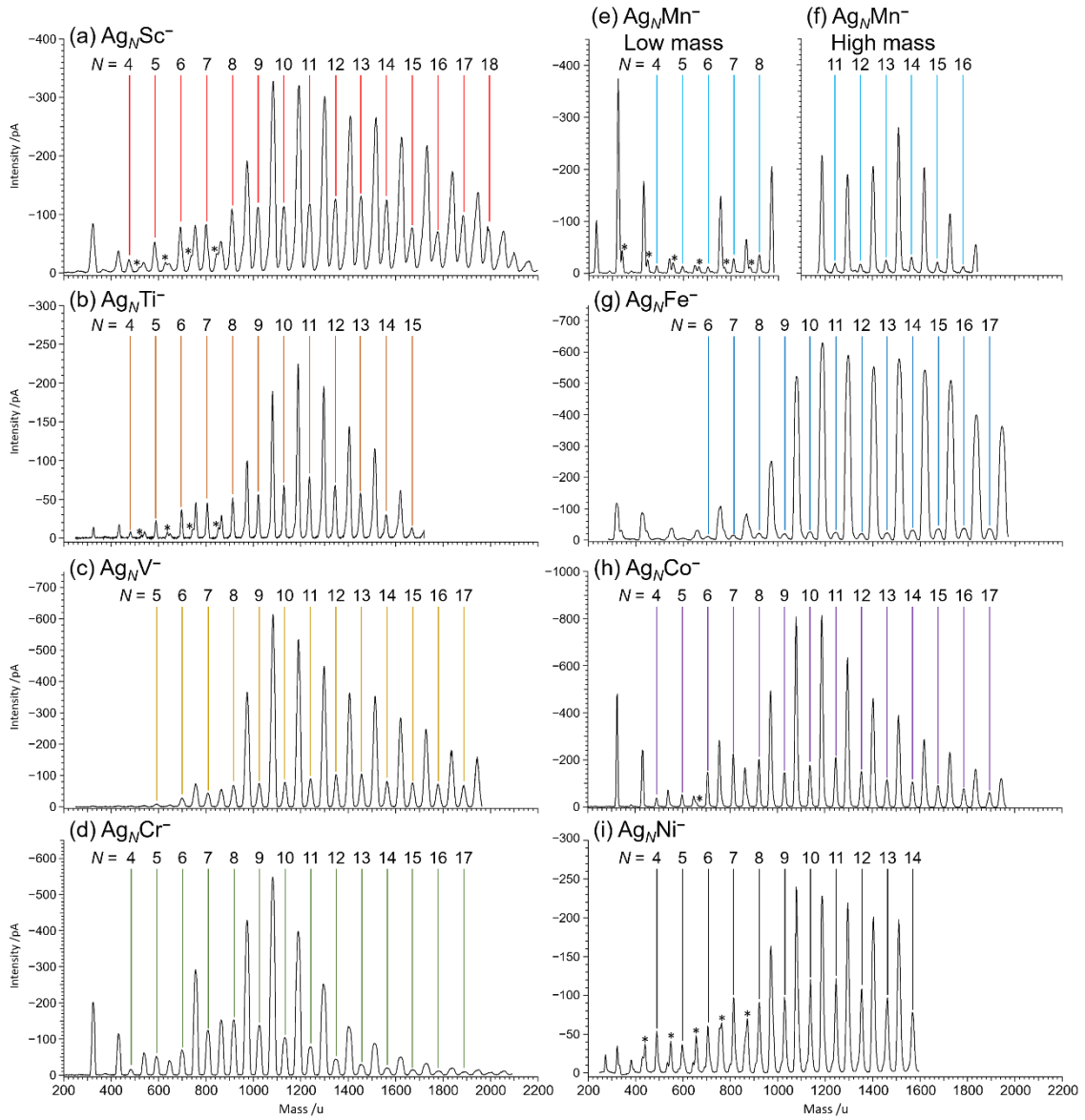


Figure 3.1. Mass spectra of cluster anions produced by simultaneous sputtering of silver and (a) scandium, (b) titanium, (c) vanadium, (d) chromium, (e) and (f) manganese, (g) iron, (h) cobalt, or (i) nickel in the magnetron-sputter ion source. The peaks of silver cluster anions with a transition metal atom, $\text{Ag}_N \text{M}^-$, are pointed out by color bars, where N is the number of Ag atoms. The peaks marked by asterisks in (a), (b), (e), (h), and (i) show silver cluster anions with two transition metal atoms, $\text{Ag}_N \text{M}_2^-$.

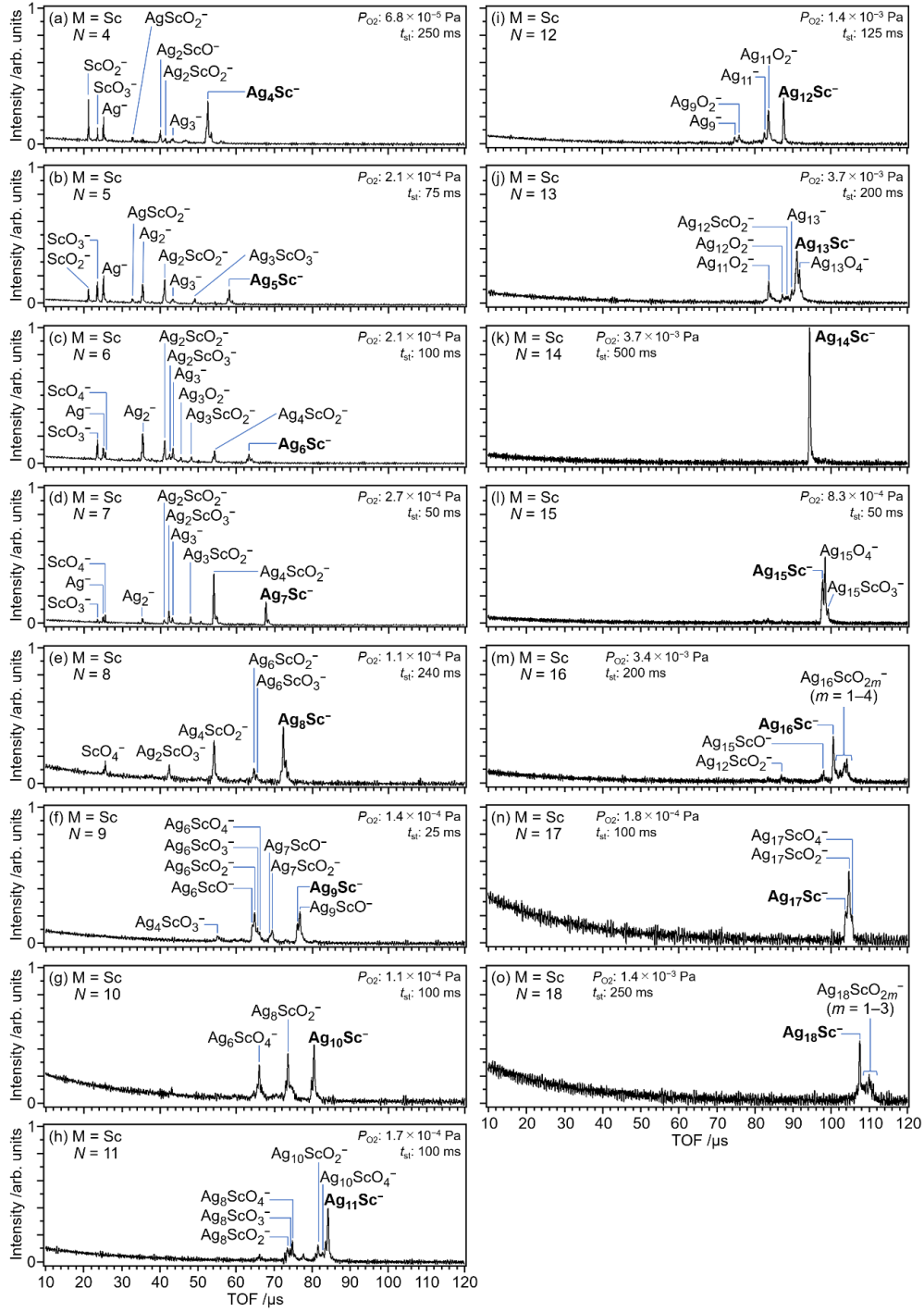


Figure 3.2. Time-of-flight (TOF) mass spectra of ions produced in the reaction of Ag_NSc^- ($N = 4\text{--}18$) with O_2 molecules. The partial pressure, P_{O_2} , and the storage time, t_{st} , in the trap are denoted in each panel.

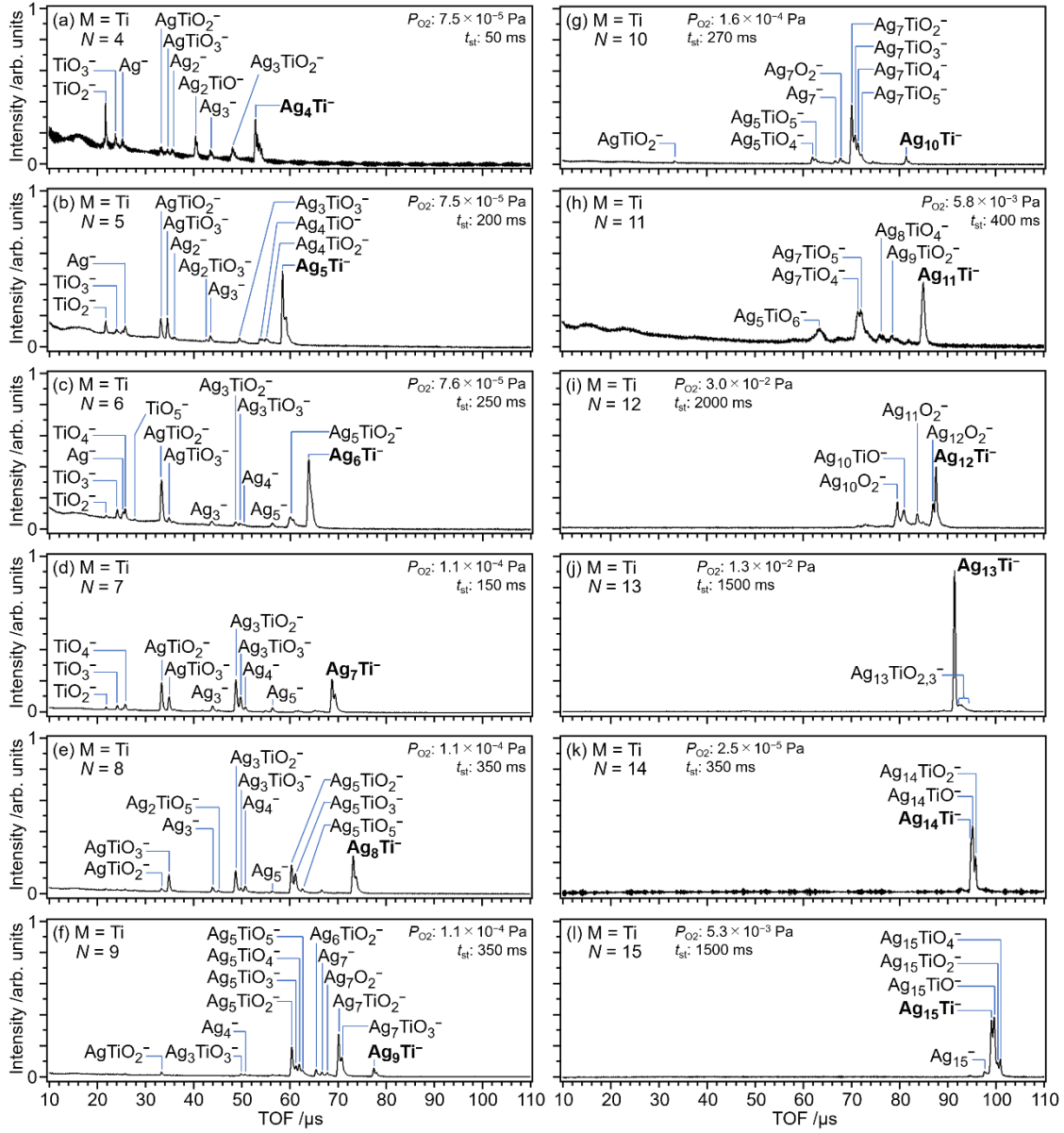


Figure 3.3. Time-of-flight (TOF) mass spectra of ions produced in the reaction of Ag_NTi^- ($N = 4\text{--}15$) with O_2 molecules. The partial pressure, P_{O_2} , and the storage time, t_{st} , in the trap are denoted in each panel.

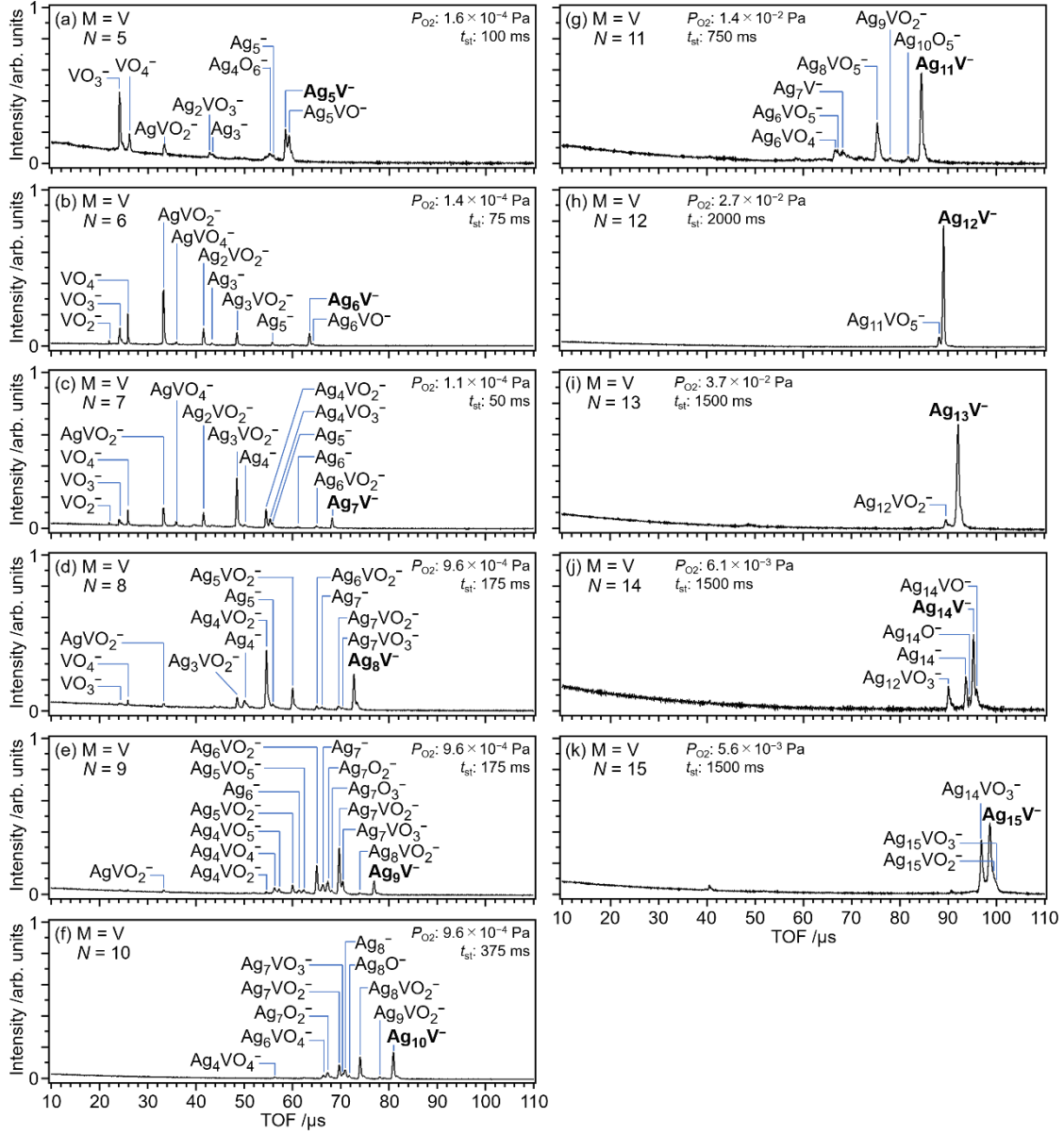


Figure 3.4. Time-of-flight (TOF) mass spectra of ions produced in the reaction of Ag_NV^- ($N = 5\text{--}15$) with O_2 molecules. The partial pressure, P_{O_2} , and the storage time, t_{st} , in the trap are denoted in each panel.

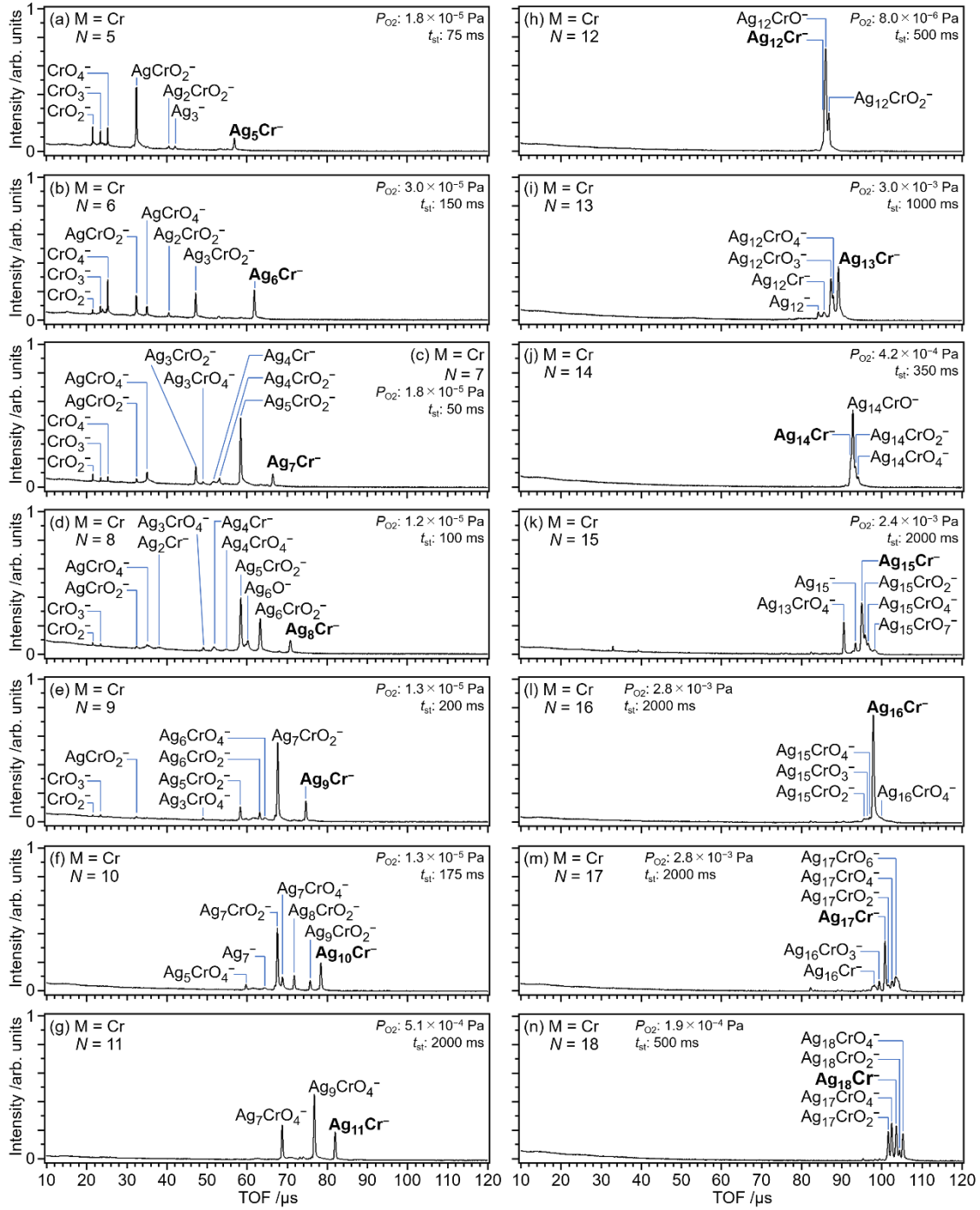


Figure 3.5. Time-of-flight (TOF) mass spectra of ions produced in the reaction of Ag_NCr^- ($N = 5-18$) with O_2 molecules. The partial pressure, P_{O_2} , and the storage time, t_{st} , in the trap are denoted in each panel.

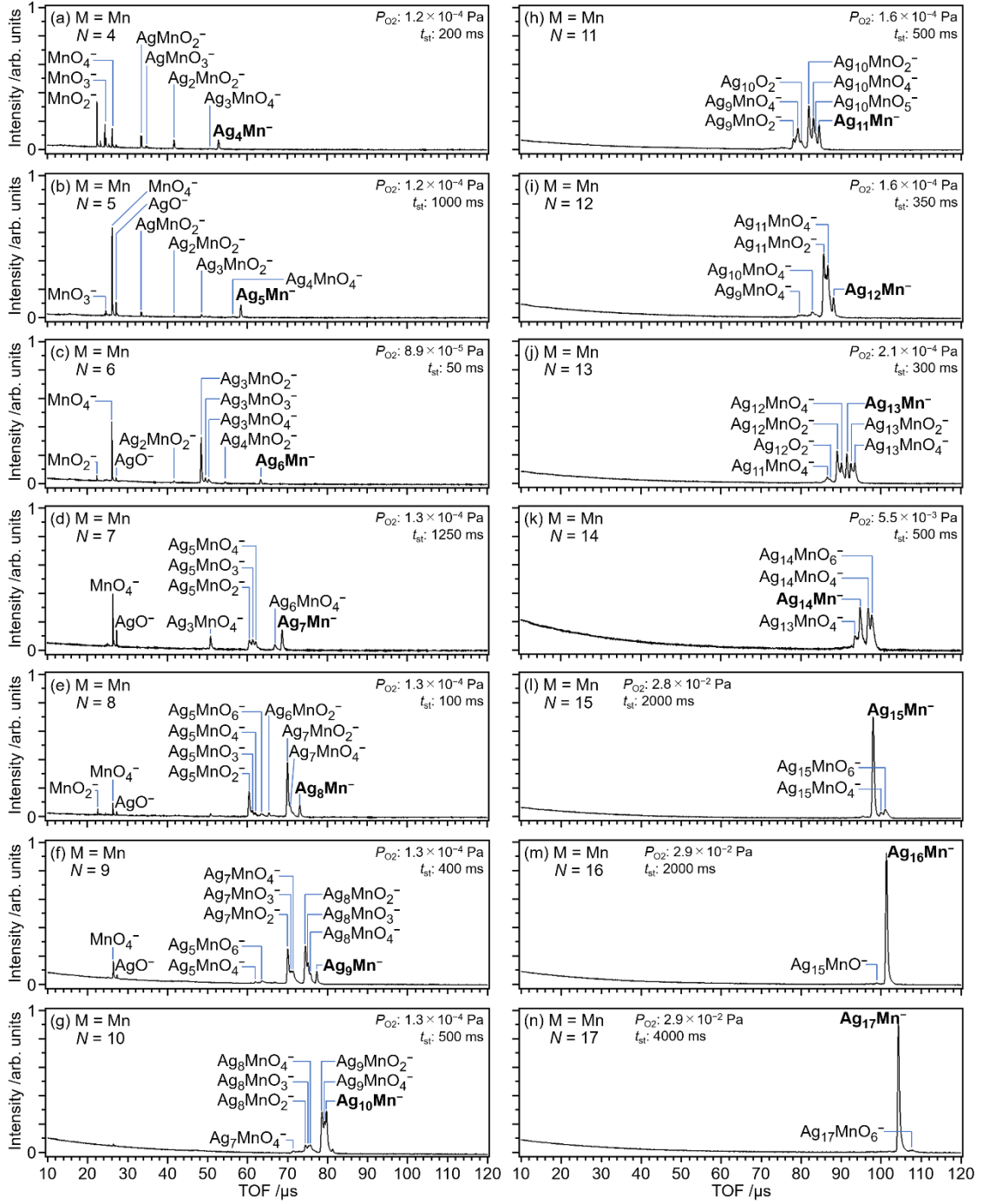


Figure 3.6. Time-of-flight (TOF) mass spectra of ions produced in the reaction of Ag_NMn^- ($N=4-17$) with O_2 molecules. The partial pressure, P_{O_2} , and the storage time, t_{st} , in the trap are denoted in each panel.

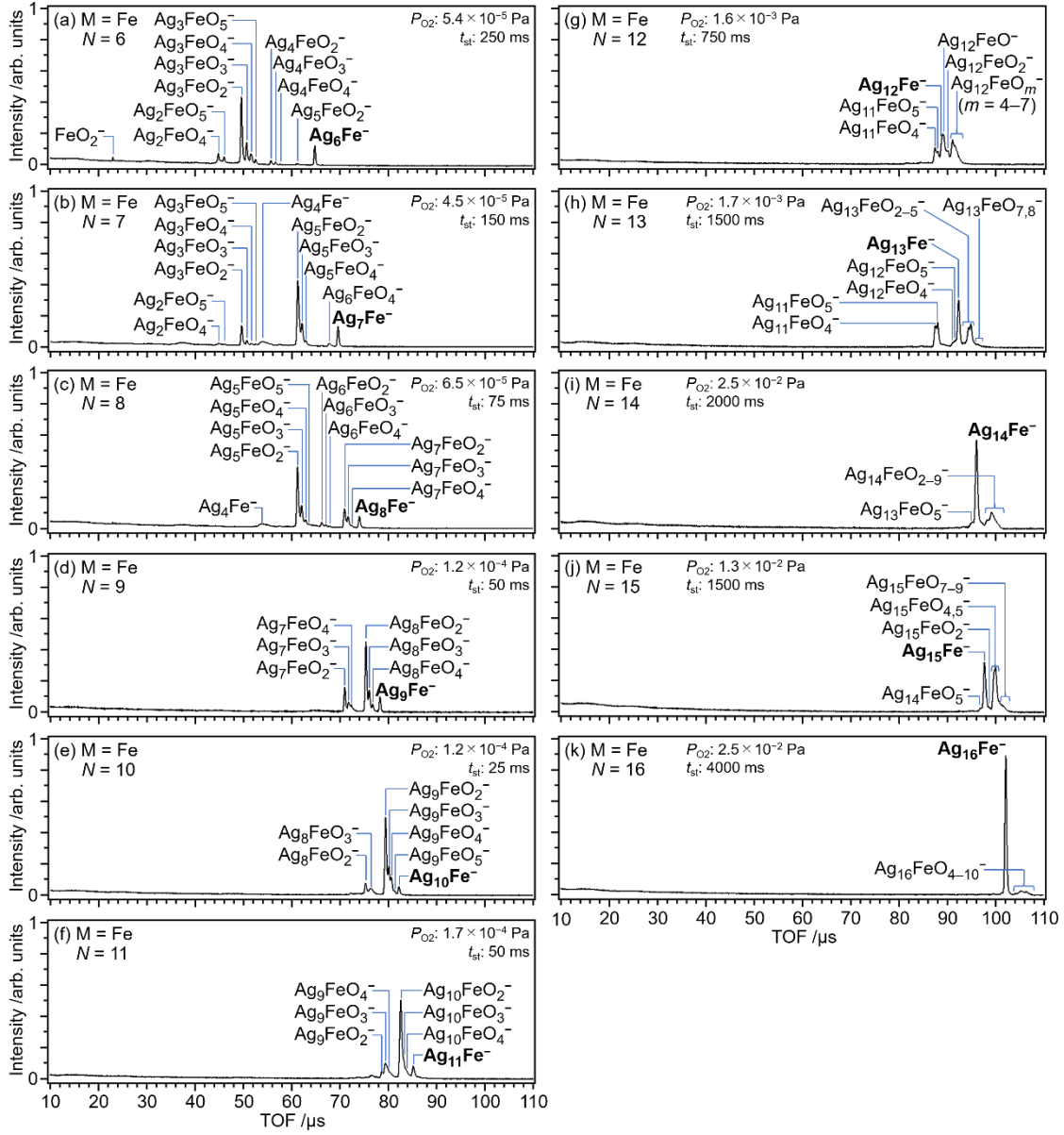


Figure 3.7. Time-of-flight (TOF) mass spectra of ions produced in the reaction of Ag_NFe^- ($N = 6-16$) with O_2 molecules. The partial pressure, P_{O_2} , and the storage time, t_{st} , in the trap are denoted in each panel.

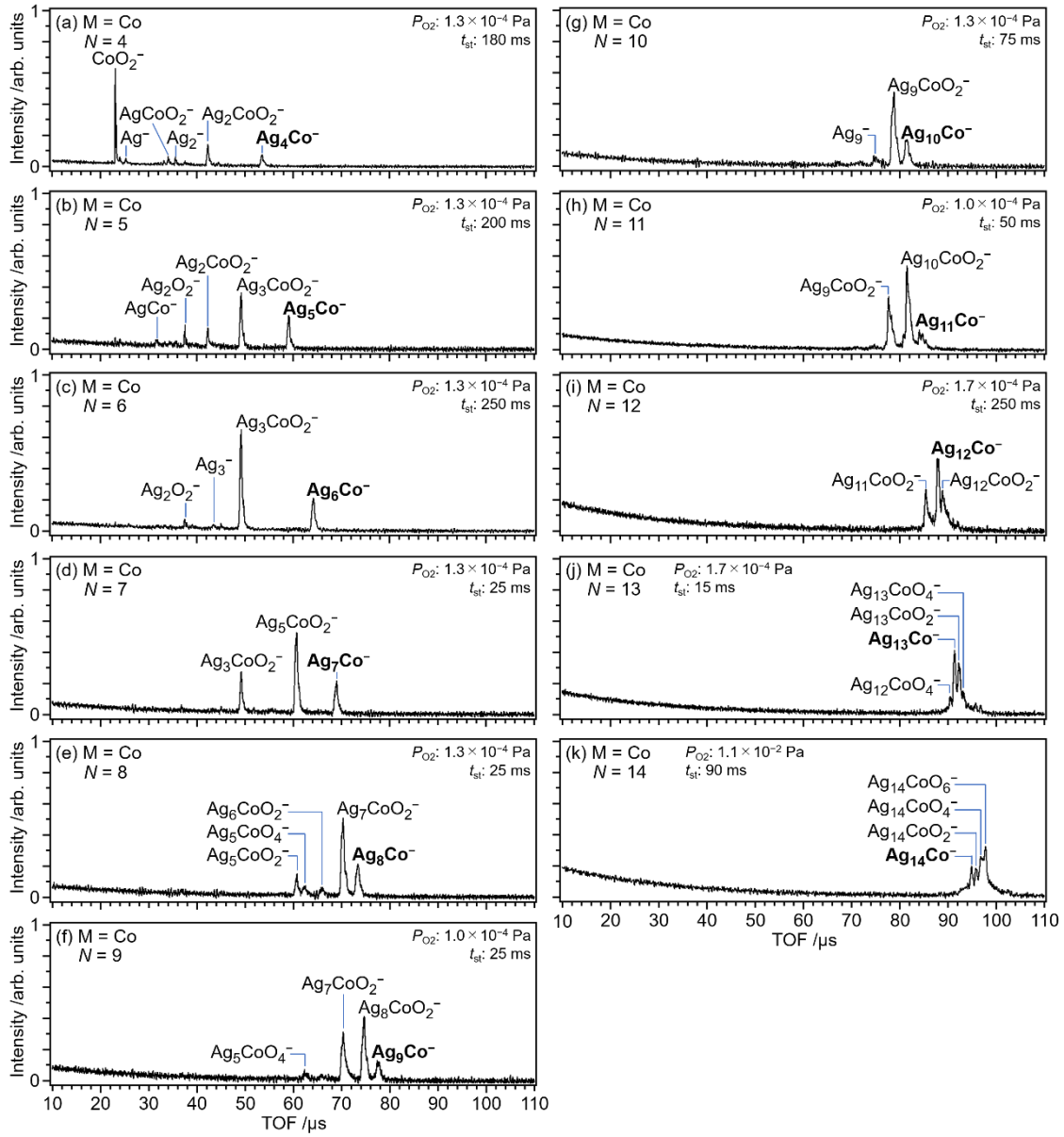


Figure 3.8. Time-of-flight (TOF) mass spectra of ions produced in the reaction of Ag_NCo^- ($N = 4-14$) with O_2 molecules. The partial pressure, P_{O_2} , and the storage time, t_{st} , in the trap are denoted in each panel.

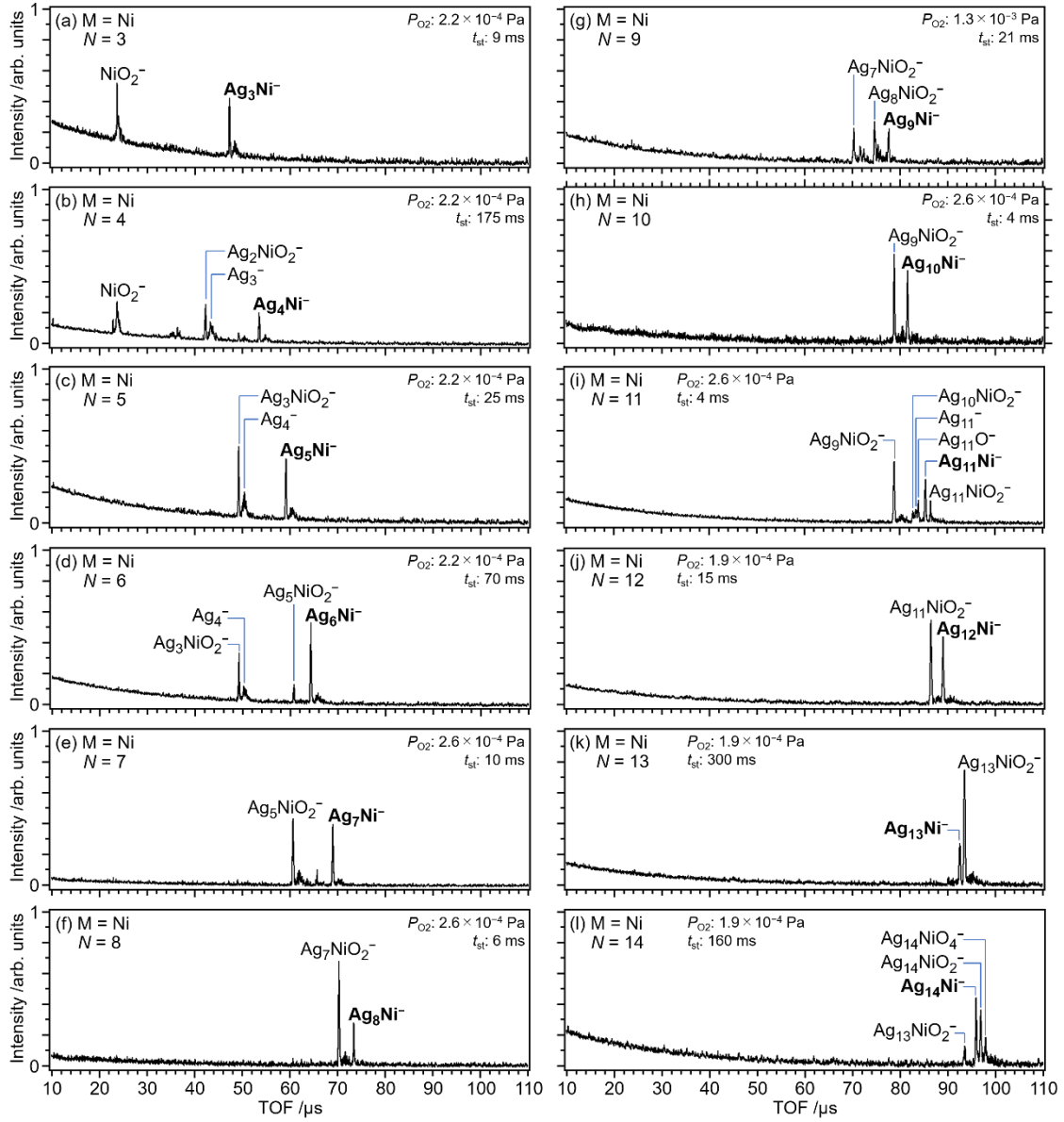


Figure 3.9. Time-of-flight (TOF) mass spectra of ions produced in the reaction of Ag_NNi^- ($N = 3-14$) with O_2 molecules. The partial pressure, P_{O_2} , and the storage time, t_{st} , in the trap are denoted in each panel.

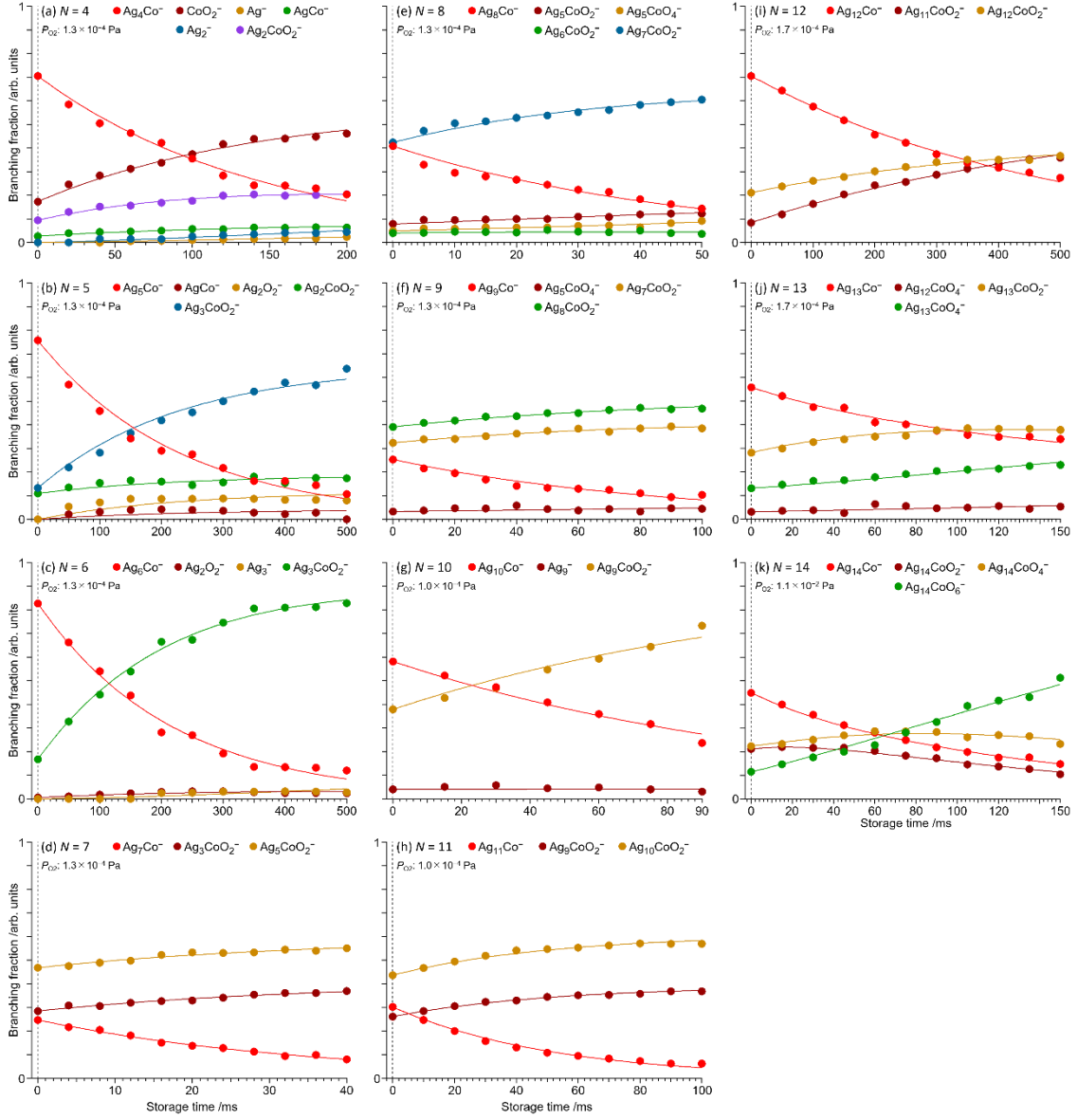


Figure 3.10. Time-dependent branching fractions of ions produced in the reaction of Ag_NCo^- ($N=4-14$) with O_2 molecules. Solid circles show the experimental data, which are normalized so that the total intensity of all the ions is to be unity. Solid curves present the data fitting.

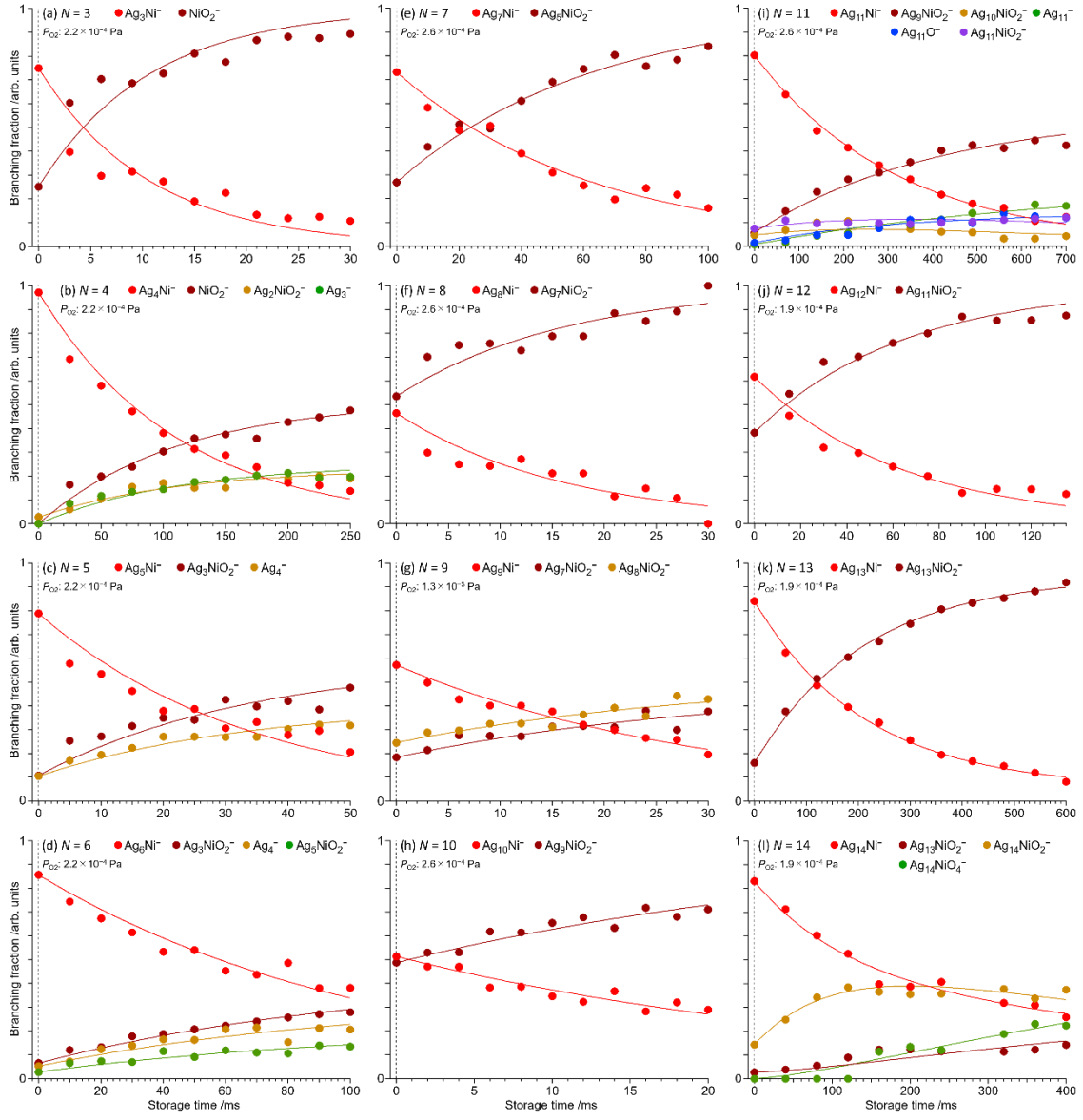


Figure 3.11. Time-dependent branching fractions of ions produced in the reaction of Ag_NNi^- ($N=3-14$) with O_2 molecules. Solid circles show the experimental data, which are normalized so that the total intensity of all the ions is to be unity. Solid curves present the data fitting.

Table 3.1. Most probably reaction pathways in the reaction of Ag_NCo^- with oxygen along with the reaction rate coefficients of each process.

Reaction paths	Reaction rate coefficients $/10^{-17} \text{ m}^3 \text{ s}^{-1}$
$\begin{array}{l} \text{Ag}_4\text{Co}^- \xrightarrow{k_1(\text{Co}, 4)} \text{Ag}_2\text{CoO}_2^- \xrightarrow{k_4(\text{Co}, 4)} \text{Ag}_2^- \\ \quad \quad \quad \xrightarrow{k_2(\text{Co}, 4)} \text{AgCo}^- \xrightarrow{k_5(\text{Co}, 4)} \text{Ag}^- \\ \quad \quad \quad \xrightarrow{k_3(\text{Co}, 4)} \text{CoO}_2^- \end{array}$	$k_1(\text{Co}, 4) = 8.0 \pm 0.26$
	$k_2(\text{Co}, 4) = 1.8 \pm 0.057$
	$k_3(\text{Co}, 4) = 13 \pm 0.42$
	$k_4(\text{Co}, 4) = 4.9 \pm 0.16$
	$k_5(\text{Co}, 4) = 2.2 \pm 0.071$
$\begin{array}{l} \text{Ag}_5\text{Co}^- \xrightarrow{k_1(\text{Co}, 5)} \text{Ag}_3\text{CoO}_2^- \\ \quad \quad \quad \xrightarrow{k_2(\text{Co}, 5)} \text{Ag}_2\text{CoO}_2^- \\ \quad \quad \quad \xrightarrow{k_3(\text{Co}, 5)} \text{Ag}_2\text{O}_2^- \\ \quad \quad \quad \xrightarrow{k_4(\text{Co}, 5)} \text{AgCo}^- \end{array}$	$k_1(\text{Co}, 5) = 9.8 \pm 0.34$
	$k_2(\text{Co}, 5) = 1.5 \pm 0.047$
	$k_3(\text{Co}, 5) = 2.2 \pm 0.072$
	$k_4(\text{Co}, 5) = 0.78 \pm 0.025$
$\begin{array}{l} \text{Ag}_6\text{Co}^- \xrightarrow{k_1(\text{Co}, 6)} \text{Ag}_3\text{CoO}_2^- \xrightarrow{k_3(\text{Co}, 6)} \text{Ag}_3^- \\ \quad \quad \quad \xrightarrow{k_2(\text{Co}, 6)} \text{Ag}_2\text{O}_2^- \end{array}$	$k_1(\text{Co}, 6) = 15 \pm 0.51$
	$k_2(\text{Co}, 6) = 0.55 \pm 0.018$
	$k_3(\text{Co}, 6) = 0.44 \pm 0.014$
$\begin{array}{l} \text{Ag}_7\text{Co}^- \xrightarrow{k_1(\text{Co}, 7)} \text{Ag}_5\text{CoO}_2^- \\ \quad \quad \quad \xrightarrow{k_2(\text{Co}, 7)} \text{Ag}_3\text{CoO}_2^- \end{array}$	$k_1(\text{Co}, 7) = 47 \pm 1.5$
	$k_2(\text{Co}, 7) = 46 \pm 1.5$
$\begin{array}{l} \text{Ag}_8\text{Co}^- \xrightarrow{k_1(\text{Co}, 8)} \text{Ag}_7\text{CoO}_2^- \\ \quad \quad \quad \downarrow k_3(\text{Co}, 8) \\ \quad \quad \quad \xrightarrow{k_2(\text{Co}, 8)} \text{Ag}_6\text{CoO}_2^- \xrightarrow{k_4(\text{Co}, 8)} \text{Ag}_5\text{CoO}_2^- \\ \quad \quad \quad \quad \quad \quad \quad \downarrow k_5(\text{Co}, 8) \\ \quad \quad \quad \quad \quad \quad \quad \text{Ag}_5\text{CoO}_4^- \end{array}$	$k_1(\text{Co}, 8) = 62 \pm 2.0$
	$k_2(\text{Co}, 8) = 8.1 \pm 0.26$
	$k_3(\text{Co}, 8) = 7.2 \pm 0.23$
	$k_4(\text{Co}, 8) = 130 \pm 4.1$
	$k_5(\text{Co}, 8) = 24 \pm 0.76$

Table 3.1. (Continued.)

Reaction paths	Reaction rate coefficients $/10^{-17} \text{ m}^3 \text{ s}^{-1}$
$\text{Ag}_9\text{Co}^- \begin{cases} \xrightarrow{k_1(\text{Co}, 9)} \text{Ag}_8\text{CoO}_2^- \\ \xrightarrow{k_2(\text{Co}, 9)} \text{Ag}_7\text{CoO}_2^- \end{cases} \xrightarrow{k_3(\text{Co}, 9)} \text{Ag}_5\text{CoO}_4^-$	$k_1(\text{Co}, 9) = 23 \pm 0.73$ $k_2(\text{Co}, 9) = 22 \pm 0.71$ $k_3(\text{Co}, 9) = 1.7 \pm 0.055$
$\text{Ag}_{10}\text{Co}^- \begin{cases} \xrightarrow{k_1(\text{Co}, 10)} \text{Ag}_9\text{CoO}_2^- \\ \xrightarrow{k_2(\text{Co}, 10)} \text{Ag}_9^- \end{cases}$	$k_1(\text{Co}, 10) = 27 \pm 0.88$ $k_2(\text{Co}, 10) = 0.15 \pm 0.0046$
$\text{Ag}_{11}\text{Co}^- \begin{cases} \xrightarrow{k_1(\text{Co}, 11)} \text{Ag}_{10}\text{CoO}_2^- \\ \xrightarrow{k_2(\text{Co}, 11)} \text{Ag}_9\text{CoO}_2^- \end{cases}$	$k_1(\text{Co}, 11) = 44 \pm 1.4$ $k_2(\text{Co}, 11) = 33 \pm 1.1$
$\text{Ag}_{12}\text{Co}^- \begin{cases} \xrightarrow{k_1(\text{Co}, 12)} \text{Ag}_{12}\text{CoO}_2^- \\ \xrightarrow{k_2(\text{Co}, 12)} \text{Ag}_{11}\text{CoO}_2^- \end{cases} \quad \text{Ag}_{12}\text{CoO}_2^- \xrightarrow{k_3(\text{Co}, 12)} \text{Ag}_{11}\text{CoO}_2^-$	$k_1(\text{Co}, 12) = 2.0 \pm 0.068$ $k_2(\text{Co}, 12) = 2.9 \pm 0.10$ $k_3(\text{Co}, 12) = 0.35 \pm 0.011$
$\text{Ag}_{13}\text{Co}^- \xrightleftharpoons[k_2(\text{Co}, 13)]{k_1(\text{Co}, 13)} \text{Ag}_{13}\text{CoO}_2^- \xrightarrow{k_3(\text{Co}, 13)} \text{Ag}_{13}\text{CoO}_4^- \xrightarrow{k_4(\text{Co}, 13)} \text{Ag}_{12}\text{CoO}_4^-$	$k_1(\text{Co}, 13) = 17 \pm 0.55$ $k_2(\text{Co}, 13) = 9.4 \pm 0.30$ $k_3(\text{Co}, 13) = 6.3 \pm 0.20$ $k_4(\text{Co}, 13) = 2.5 \pm 0.079$
$\text{Ag}_{14}\text{Co}^- \xrightleftharpoons[k_2(\text{Co}, 14)]{k_1(\text{Co}, 14)} \text{Ag}_{14}\text{CoO}_2^- \xrightarrow{k_3(\text{Co}, 14)} \text{Ag}_{14}\text{CoO}_4^- \xrightarrow{k_4(\text{Co}, 14)} \text{Ag}_{14}\text{CoO}_6^-$	$k_1(\text{Co}, 14) = 0.52 \pm 0.016$ $k_2(\text{Co}, 14) = 0.35 \pm 0.011$ $k_3(\text{Co}, 14) = 0.56 \pm 0.018$ $k_4(\text{Co}, 14) = 0.35 \pm 0.011$

Table 3.2. Most probably reaction pathways in the reaction of Ag_NNi^- with oxygen along with the reaction rate coefficients of each process.

Reaction paths	Reaction rate coefficient $/10^{-17} \text{ m}^3 \text{ s}^{-1}$
$\text{Ag}_3\text{Ni}^- \xrightarrow{k_1(\text{Ni}, 3)} \text{NiO}_2^-$	$k_1(\text{Ni}, 3) = 180 \pm 5.7$
$\text{Ag}_4\text{Ni}^- \begin{cases} \xrightarrow{k_1(\text{Ni}, 4)} \text{Ag}_3^- \\ \xrightarrow{k_2(\text{Ni}, 4)} \text{Ag}_2\text{NiO}_2^- \\ \xrightarrow{k_3(\text{Ni}, 4)} \text{NiO}_2^- \end{cases}$	$k_1(\text{Ni}, 4) = 4.4 \pm 0.14$
	$k_2(\text{Ni}, 4) = 3.6 \pm 0.12$
	$k_3(\text{Ni}, 4) = 9.1 \pm 0.30$
$\text{Ag}_5\text{Ni}^- \begin{cases} \xrightarrow{k_1(\text{Ni}, 5)} \text{Ag}_4^- \\ \xrightarrow{k_2(\text{Ni}, 5)} \text{Ag}_3\text{NiO}_2^- \end{cases}$	$k_1(\text{Ni}, 5) = 22 \pm 0.69$
	$k_2(\text{Ni}, 5) = 34 \pm 1.1$
$\text{Ag}_6\text{Ni}^- \begin{cases} \xrightarrow{k_1(\text{Ni}, 6)} \text{Ag}_5\text{NiO}_2^- \\ \xrightarrow{k_2(\text{Ni}, 6)} \text{Ag}_4^- \\ \xrightarrow{k_3(\text{Ni}, 6)} \text{Ag}_3\text{NiO}_2^- \end{cases}$	$k_1(\text{Ni}, 6) = 4.0 \pm 0.13$
	$k_2(\text{Ni}, 6) = 6.1 \pm 0.19$
	$k_3(\text{Ni}, 6) = 7.8 \pm 0.25$
$\text{Ag}_7\text{Ni}^- \xrightarrow{k_1(\text{Ni}, 7)} \text{Ag}_5\text{NiO}_2^-$	$k_1(\text{Ni}, 7) = 26 \pm 0.83$
$\text{Ag}_8\text{Ni}^- \xrightarrow{k_1(\text{Ni}, 8)} \text{Ag}_7\text{NiO}_2^-$	$k_1(\text{Ni}, 8) = 99 \pm 3.2$
$\text{Ag}_9\text{Ni}^- \begin{cases} \xrightarrow{k_1(\text{Ni}, 9)} \text{Ag}_8\text{NiO}_2^- \\ \xrightarrow{k_2(\text{Ni}, 9)} \text{Ag}_7\text{NiO}_2^- \end{cases}$	$k_1(\text{Ni}, 9) = 5.0 \pm 0.16$
	$k_2(\text{Ni}, 9) = 5.4 \pm 0.17$
$\text{Ag}_{10}\text{Ni}^- \xrightarrow{k_1(\text{Ni}, 10)} \text{Ag}_9\text{NiO}_2^-$	$k_1(\text{Ni}, 10) = 52 \pm 1.7$

Reaction paths	Reaction rate coefficient $/10^{-17} \text{ m}^3 \text{ s}^{-1}$
	$k_1(\text{Ni}, 11) = 0.97 \pm 0.032$
	$k_2(\text{Ni}, 11) = 0.76 \pm 0.025$
$\text{Ag}_{11}\text{Ni}^- \xrightarrow{k_1(\text{Ni}, 11)} \text{Ag}_{11}\text{NiO}_2^-$ $\quad \quad \quad \downarrow k_6(\text{Ni}, 11)$ $\quad \quad \quad \text{Ag}_{11}^-$ $\quad \quad \quad \downarrow k_3(\text{Ni}, 11)$ $\quad \quad \quad \text{Ag}_{11}\text{O}^-$ $\quad \quad \quad \downarrow k_4(\text{Ni}, 11)$ $\quad \quad \quad \text{Ag}_{10}\text{NiO}_2^-$ $\quad \quad \quad \downarrow k_7(\text{Ni}, 11)$ $\quad \quad \quad \text{Ag}_9\text{NiO}_2^-$ $\quad \quad \quad \downarrow k_5(\text{Ni}, 11)$	$k_3(\text{Ni}, 11) = 1.1 \pm 0.035$
	$k_4(\text{Ni}, 11) = 0.90 \pm 0.029$
	$k_5(\text{Ni}, 11) = 3.1 \pm 0.11$
	$k_6(\text{Ni}, 11) = 2.4 \pm 0.075$
	$k_7(\text{Ni}, 11) = 4.6 \pm 0.15$
$\text{Ag}_{12}\text{Ni}^- \xrightarrow{k_1(\text{Ni}, 12)} \text{Ag}_{11}\text{NiO}_2^-$	$k_1(\text{Ni}, 12) = 34 \pm 1.1$
$\text{Ag}_{13}\text{Ni}^- \xrightleftharpoons[k_2(\text{Ni}, 13)]{k_1(\text{Ni}, 13)} \text{Ag}_{13}\text{NiO}_2^-$	$k_1(\text{Ni}, 13) = 9.6 \pm 0.34$
	$k_2(\text{Ni}, 13) = 0.54 \pm 0.017$
	$k_1(\text{Ni}, 14) = 12 \pm 0.38$
$\text{Ag}_{14}\text{Ni}^- \xrightleftharpoons[k_2(\text{Ni}, 14)]{k_1(\text{Ni}, 14)} \text{Ag}_{14}\text{NiO}_2^- \xrightarrow{k_3(\text{Ni}, 14)} \text{Ag}_{14}\text{NiO}_4^-$ $\quad \quad \quad \quad \quad \quad \quad \quad \quad \quad \quad \quad \quad \quad \quad \downarrow k_4(\text{Ni}, 14)$ $\quad \quad \quad \quad \quad \quad \quad \quad \quad \quad \quad \quad \quad \quad \quad \text{Ag}_{13}\text{NiO}_2^-$	$k_2(\text{Ni}, 14) = 6.4 \pm 0.20$
	$k_3(\text{Ni}, 14) = 3.7 \pm 0.12$
	$k_4(\text{Ni}, 14) = 2.1 \pm 0.067$

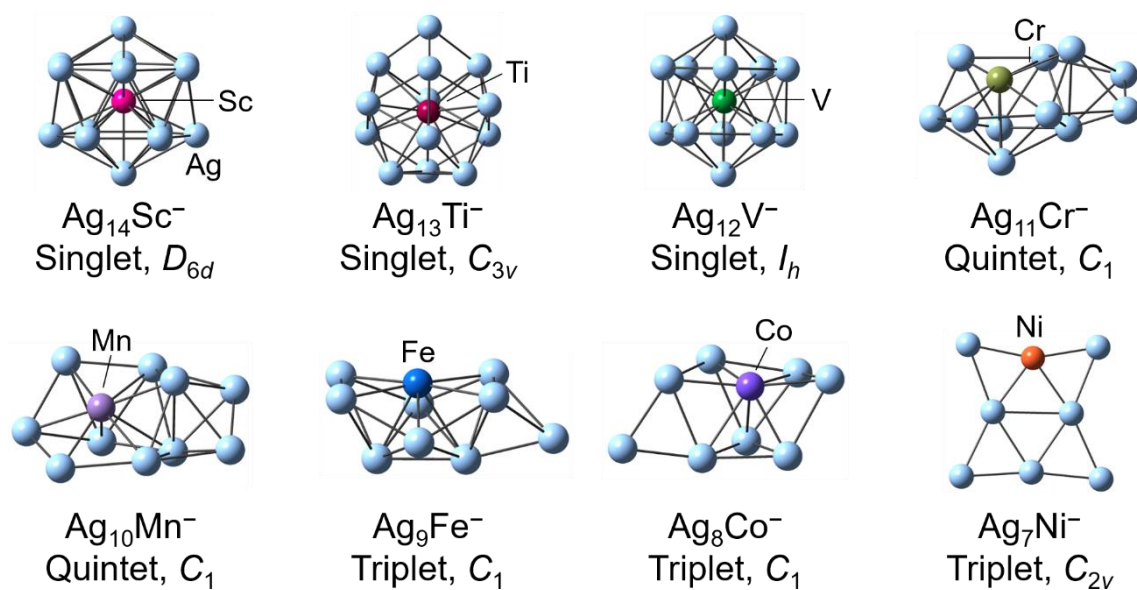


Figure 3.12. The most stable geometric structures of $\text{Ag}_{14}\text{Sc}^-$, $\text{Ag}_{13}\text{Ti}^-$, Ag_{12}V^- , $\text{Ag}_{11}\text{Cr}^-$, $\text{Ag}_{10}\text{Mn}^-$, Ag_9Fe^- , Ag_8Co^- and Ag_7Ni^- optimized by DFT calculation. Spin multiplicity and symmetry are denoted. Note that the calculation of Ag_7Ni^- was performed by B3LYP functional instead of B3LYP \star functional; B3LYP \star leads Ag_7Ni^- to a singlet state with an endohedral geometry, which did not explain its high reactivity described in Chapter 4.

Chapter 4. Reactivity of $\text{Ag}_N\text{M}^{+/-}$ ($\text{M} = \text{Sc-Ni}$)

4.1. Introduction

Metal clusters show remarkable size-dependent reactivity because their electronic structures consist of discrete energy levels, which is different from the band structure of bulk metal. Reactivity measurement toward oxygen is often employed for probing their electronic structure by stability of the clusters. As one of the earliest studies, reactions of Al_N^+ with oxygen have been investigated by Jarrold and Bower in 1986.^[90] In the study, aluminum clusters were generated by laser vaporization of an aluminum rod and ionized by a high energy electron beam. Typical mass spectra showed that Al_7^+ exhibits substantially larger intensity than its neighbors. After mass selection, the size-selected Al_N^+ were reacted with O_2 in a gas cell and product ions were analyzed by a quadrupole mass filter. The product distribution indicated that Al_7^+ is slightly more favored than the other product ions. It is suggested that Al_7^+ is a magic cluster because it possesses 20 valence electrons to form a closed electronic shell. Anionic clusters, Al_N^- , also have been investigated by oxygen-etching reaction by Castleman's group.^[6] They reported that Al_{13}^- exhibits high resistant to oxygen etching because it formed a closed electronic shell with 40 valence electrons. Thus, it is possible to investigate electronic structures by reactivity with oxygen. Afterwards, a variety of metal clusters have been investigated by reaction measurements to explore the electronic and geometric structures.^[7,91-93]

For development of new catalytic clusters, heteroatom-doped metal clusters have been attracting much attention because the electronic and geometric structures of these clusters are modified by the dopant atom. Especially, transition-metal-doped clusters have been investigated by theoretical and experimental techniques. In the systems, d electrons of the dopant atom interact with s electrons of a host metal. It is known for bulk dilute magnetic alloys that d electrons are delocalized when the s-d interaction is strong.^[21-23] However, the s-d interaction is not trivial for doped clusters

because the electronic structure of the host metal is modified from the band structure of bulk metal. The study on such clusters was performed by photofragmentation of Ag_NM^+ ($\text{M} = \text{Sc-Ni}$).^[37,38] It is reported that these clusters show high abundance at magic sizes, which have 18 valence electrons including 3d electrons, except for $\text{M} = \text{Cr}$ and Mn . It is concluded that 3d electrons are delocalized to form a closed electronic shell with 18 electrons. Recently, the electronic and geometric structures of such Ag_NM^+ ($\text{M} = \text{Sc-Ni}$) have been investigated through reactivity toward O_2 and NO .^[45,94,95] It is also revealed that 18-e clusters showed the lowest reactivity due to the closed electronic shell structure with delocalized 3d electrons. Therefore, the electron counting is important to delocalize 3d electrons.

The author extended the reactivity measurement to anionic species. Since anionic clusters have two more electrons at the same size, it is possible to clarify importance of electron counting for delocalization of 3d electrons by comparing with corresponding cations. Anions should have geometric differences from those of cations due to two less Ag atoms at the same electron count. Therefore, in this chapter, the electronic and geometric structures of anions and cations are investigated by reactivity measurement and DFT calculations to explore the electron-counting and geometric effects on localization/delocalization of 3d electrons.

4.2. Analysis of experimental data

The experimental procedures have been described in Chapter 2. Each TOF mass spectrum for all the doped clusters as shown in Figs. 3.2–3.9 was fitted by a function described as Eq. (3.2), and then the branching fraction of the reactant was evaluated at each storage time, t_{st} . The time-dependent branching fraction of the reactant can be explained by the following differential equation:

$$\frac{d[\text{Ag}_N\text{M}^-]}{dt} = -k'(\text{M}, N)[\text{Ag}_N\text{M}^-], \quad (4.1)$$

where $[\text{Ag}_N\text{M}^-]$ is the branching fraction of the reactant and $k'(\text{M}, N)$ is the reaction-rate

constant for the dopant M and the size N. Therefore, the reaction-rate coefficient, $k(M, N)$, can be derived from the extinction rate of the reactant cluster ion as follows:

$$k(M, N) = -\frac{1}{[O_2]} \frac{d}{dt} \ln \left(\frac{[Ag_N M^-]_t}{[Ag_N M^-]_0} \right), \quad (4.2)$$

where the subscript, t , gives the storage time.

4.3. Results

4.3.1. The size-dependent reactivity of $Ag_N M^{+/-}$

Figure 4.1 shows reaction-rate coefficients of $Ag_N M^-$ ($M = Sc-Ni$) as a function of the number of Ag atoms, N ; those values evaluated for $Ag_N M^+$ are superimposed for comparison, which have been reported in the previous study^[45,46]. The plot displays relative values with respect to undoped Ag_8^+ that was measured to be $(5.8 \pm 1.8) \times 10^{-15} \text{ cm}^3 \text{ s}^{-1}$; ^[46] the absolute rate coefficient is subject to a systematic error as large as 30% due to uncertainty in the O_2 pressure in the ion trap. On the other hand, the relative values suffer only from statistical errors of about 10%, which allow us to show the size dependence in a more precise manner.

M = Sc. Fig. 4.1(a) shows size-dependent reactivity of $Ag_N Sc^-$ (open circles) and $Ag_N Sc^+$ (closed circles). In the small size range, $Ag_N Sc^-$ exhibited reactivity about 10^5 times higher than that of Ag_8^+ , which is comparable to the reactivity of $Ag_N Sc^+$. As the size increased up to $N = 14$, the reactivity of $Ag_N Sc^-$ decreased. $Ag_N Sc^-$ possesses $N + 4$ valence electrons, *i.e.*, N electrons from Ag 5s, plus 3 electrons from Sc 4s² and 3d¹, and plus one for the negative charge. $Ag_{14} Sc^-$ with 18 valence electrons exhibited the lowest reactivity in the size dependence reactivity, whereas the reactivity showed the lowest at $Ag_{16} Sc^+$ with 18 valence electrons. For large clusters, $Ag_N Sc^-$ exhibited reactivity as high as small-sized clusters.

M = Ti. Fig. 4.1(b) shows size-dependent reactivity of $Ag_N Ti^-$ (open circles) and $Ag_N Ti^+$ (closed circles). Similarly to $Ag_N Sc^{+/-}$, small sized $Ag_N Ti^-$ exhibited high

reactivity as well as Ag_NTi^+ , whereas the reactivity decreased from $N = 10$ for both anionic and cationic Ag_NTi . Ag_NTi^- possesses $N + 5$ valence electrons, *i.e.*, N from Ag 5s, plus 4 from Ti 4s² and 3d², and plus one for the negative charge. The 18-e cluster, $\text{Ag}_{13}\text{Ti}^-$, shows the lowest reactivity. For Ag_NTi^+ , the reactivity showed the lowest at $N = 15$, which also possesses 18 valence electrons. $\text{Ag}_{14}\text{Ti}^-$ exhibited high reactivity as well as small sized clusters, whereas the reactivity of $\text{Ag}_{15}\text{Ti}^-$ exhibited 10² times lower than that of $\text{Ag}_{14}\text{Ti}^-$.

M = V. Fig. 4.1(c) shows size-dependent reactivity of Ag_NV^- (open circles) and Ag_NV^+ (closed circles). Ag_NV^- shows size-dependent reactivity similar to that of $\text{Ag}_N\text{Sc}^{+/-}$ and $\text{Ag}_N\text{Ti}^{+/-}$. The reactivity decreased as the size increased, and then Ag_{12}V^- exhibited the lowest reactivity. Ag_{12}V^- possesses 18 valence electrons, *i.e.*, 12 from Ag 5s, plus 5 from V 4s² and 3d³, and plus one for the negative charge. For Ag_NV^+ , the size-dependence is similar to Ag_NV^- . Ag_{14}V^+ is isoelectronic with Ag_{12}V^- , which shows the lowest reactivity.

M = Cr. Fig. 4.1(d) shows size-dependent reactivity of Ag_NCr^- (open circles) and Ag_NCr^+ (closed circles). In small sizes, Ag_NCr^- exhibits high reactivity as well as the clusters explained above. Ag_NCr^- possesses $N + 7$ valence electrons, *i.e.*, N from Ag 5s, plus 6 from Cr 4s¹ and 3d⁵, and plus one for the negative charge. The size-dependent reactivity for Ag_NCr^- shows odd–even alternation in $N = 10$ –15, where odd electron clusters exhibit reactivity higher than that of even ones. The 18-e cluster, $\text{Ag}_{11}\text{Cr}^-$, does not exhibit the lowest reactivity in contrast to Sc-, Ti-, and V-doped clusters. The reactivity of Ag_NCr^+ decreased as the size increased, and then $\text{Ag}_{14}\text{Cr}^+$ showed the lowest reactivity in the case of $N = 5$ –14. Although $\text{Ag}_{13}\text{Cr}^+$ possesses 18 valence electrons, its reactivity does not exhibit the minimum reactivity as well as $\text{Ag}_{11}\text{Cr}^-$.

M = Mn. Fig. 4.1(e) shows size-dependent reactivity of Ag_NMn^- (open circles)

and Ag_NMn^+ (closed circles). Ag_NMn^- kept high reactivity up to $N = 13$, and then decreased as the size increased. $\text{Ag}_{16}\text{Mn}^-$ showed the lowest reactivity in the present study. Ag_NMn^- possesses $N + 8$ electrons, *i.e.*, N from Ag 5s, plus 7 from Mn 4s² and 3d⁵, and plus one for the negative charge. $\text{Ag}_{10}\text{Mn}^-$ did not exhibit the lowest reactivity even though the cluster have 18 valence electrons. For Ag_NMn^+ , the reactivity decreased from $N = 10$ as the size increased. $\text{Ag}_{12}\text{Mn}^+$ also does not exhibit to the lowest reactivity as well as $\text{Ag}_{10}\text{Mn}^-$.

M = Fe. Fig. 4.1(f) shows size-dependent reactivity of Ag_NFe^- (open circles) and Ag_NFe^+ (closed circles). Ag_NFe^- exhibit size dependence similar to other doped clusters explained above, *i.e.*, high reactivity at small sizes and comparable with Ag_8^+ at larger sizes. The reactivity of $\text{Ag}_{16}\text{Fe}^-$ is the lowest in the present study. Ag_NFe^- possesses $N + 9$ valence electrons, *i.e.*, N from Ag 5s, plus 8 from Fe 4s² and 3d⁶, and plus one for the negative charge. Ag_9Fe^- shows the high reactivity as well as the neighboring sizes, although the cluster has 18 valence electrons. On the other hand, Ag_NFe^+ exhibit the lowest reactivity at $N = 11$, which possesses 18 valence electrons.

M = Co. Fig. 4.1(g) shows size-dependent reactivity of Ag_NCo^- (open circles) and Ag_NCo^+ (closed circles). Ag_NCo^- exhibit reactivity 10³ times or much higher than that of Ag_8^+ . The cluster possesses $N + 10$ valence electrons, *i.e.*, N from Ag 5s, plus 9 from Co 4s² and 3d⁷, and plus one for the negative charge. The 18 valence-electron cluster is Ag_8Co^- , which shows high reactivity as well as neighboring sizes. In contrast, the reactivity of Ag_NCo^+ shows different size dependence, which decreases from Ag_7Co^+ as the size increased. The 18-e cluster, $\text{Ag}_{10}\text{Co}^+$, shows the lowest reactivity.

M = Ni. Fig. 4.1(h) shows size-dependent reactivity of Ag_NNi^- (open circles) and Ag_NNi^+ (closed circles). Ag_NNi^- exhibited reactivity 10⁴ times or higher than that of Ag_8^+ . The cluster possesses $N + 11$ valence electrons, *i.e.*, N from Ag 5s, plus 9 from

Co $4s^2$ and $3d^8$, and plus one for the negative charge. The odd–even alternation is observed in $N=7$ – 13 , where odd electron clusters exhibit higher reactivity than even ones. Although Ag_7Ni^- possesses 18 valence electrons, the cluster shows reactivity as high as neighboring sizes. On the other hand, the reactivity of Ag_NNi^+ decreased as the size increased, and then Ag_9Ni^+ showed the lowest reactivity, which has 18 valence electrons. These trends are similar to $\text{Ag}_N\text{Fe}^{+/-}$ and $\text{Ag}_N\text{Co}^{+/-}$.

4.3.2. Theoretical results of $\text{Ag}_N\text{M}^{+/-}$

Figures 4.2–4.17 show the electronic structure and molecular orbitals for 18-e anions and cations. The optimized geometric structures of cations are shown in each figure as panel (a). The geometric structures for 18-e anions were summarized in Fig. 3.12 in Chapter 3 as well.

M = Sc. For $\text{Ag}_{14}\text{Sc}^-$, the electronic structure and the corresponding molecular orbitals are shown in Fig. 4.2 along with the optimized geometric structure. The electronic structure is spin-unpolarized as shown in Fig. 4.2(b), where the energy levels of the Sc 3d orbital overlaps with those of sp orbitals of Ag and Sc. The contours of the molecular orbitals (Fig. 4.2c) show 1S, 1P, and 1D superatomic orbitals. As for cations, the theoretical results for $\text{Ag}_{16}\text{Sc}^+$ are shown in Fig. 4.3. The structure optimization performed on $\text{Ag}_{16}\text{Sc}^+$ found that the most stable isomer (Fig. 4.3a) has a T_d symmetry with the Sc atom fully encapsulated by Ag atoms, which is similar to $\text{Cu}_{16}\text{Sc}^+$ reported previously.^[40] The corresponding electronic structure (Fig. 4.3b) reveals that the energy levels originating from the Sc 3d orbital overlaps with those of sp orbitals of Ag and Sc. The contours of the molecular orbitals (Fig. 4.3c) illustrate 1S, 1P, and 1D superatomic orbitals, which accommodate 18 valence electrons including 3d electrons.

M = Ti. The features in the electronic structures and the molecular orbitals of Sc-doped clusters are common to Ti-doped ones. The electronic and the corresponding

molecular orbitals for $\text{Ag}_{13}\text{Ti}^-$ are shown in Fig. 4.4 along with the optimized geometric structure. As for cations, the results of DFT calculations for $\text{Ag}_{15}\text{Ti}^+$ are shown in Fig. 4.5. The geometric structures for these 18-e clusters were found to be endohedral geometries with the doped atom encapsulated as shown in Figs. 4.4(a) and 4.5(a). The most stable isomers are spin-unpolarized singlet states, where energy levels of the dopant 3d orbitals overlap with those of sp orbitals of Ag and Ti as shown in Figs. 4.4(b) and 4.5(b). The contours of the molecular orbitals (Figs. 4.4c and 4.5c) show 1S, 1P, and 1D superatomic orbitals, which are fully occupied by 18 valence electrons with 3d electrons.

M = V. The features in the electronic structures and the molecular orbitals of Sc- and Ti-doped clusters are common to V-doped ones. The geometric and electronic structures and the corresponding molecular orbitals for Ag_{12}V^- and Ag_{14}V^+ are shown in Figs. 4.6 and 4.7, respectively. The theoretical results for Ag_{14}V^+ have been reported in previous reactivity measurements of cationic Ag_NM^+ .^[46] The geometric structures of Ag_{12}V^- and Ag_{14}V^+ were found to be endohedral geometries with the doped atom encapsulated as shown in Figs. 4.6(a) and 4.7(a), respectively. The electronic structures for the most stable isomers (Figs. 4.6b and 4.7b) reveal that the energy levels of the dopant 3d orbital overlaps with those of sp orbitals of Ag and V. These clusters are a spin-unpolarized singlet state. The contours of the molecular orbitals (Figs. 4.6c and 4.7c) show 1S, 1P, and 1D superatomic orbitals, which are occupied by 18 valence electrons with 3d electrons. The present result of Ag_{14}V^+ is consistent with the previous theoretical studies,^[44,73] where Ag_{14}V^+ was reported to be in a singlet state with an endohedral geometry similar to $\text{Ag}_{14}\text{Sc}^-$ described above.

M = Cr. As for the anion, $\text{Ag}_{11}\text{Cr}^-$ shows an exohedral geometry (Fig. 4.8a) and the quintet state as the most stable isomer. Its electronic structure illustrates that 3d electrons occupy up-spin states as shown in Fig. 4.8b. DFT calculation for $\text{Ag}_{13}\text{Cr}^+$

shows the most stable isomer is a triplet state with a fully encapsulated Cr atom as shown in Fig. 4.9(a). The electronic structure (Fig. 4.9b) exhibits that the 3d orbitals of Cr separated from sp orbitals of Ag and Cr.

M = Mn. The results for the Cr-doped clusters manifest trends common to Mn-doped ones. The most stable isomer of $\text{Ag}_{10}\text{Mn}^-$ is a quintet state shown in Fig. 4.10(a). Its electronic structure (Fig. 4.10b) illustrates that five 3d electrons of Mn atom occupy up-spin states, which are separated from sp orbitals of Ag and Mn. As for cations, the results of DFT calculations for $\text{Ag}_{12}\text{Mn}^+$ are shown in Fig. 4.11. The geometric and electronic structures have been reported in previous reactivity measurements of cationic Ag_NM .^[46] The doped Mn in $\text{Ag}_{12}\text{Mn}^+$ is found to be partially encapsulated by Ag atoms as shown in Fig. 4.11(a). Its electronic structure (Fig. 4.11b) exhibits that 3d orbitals are separated from sp orbitals of Ag and Mn.

M = Fe. Figure 4.12 shows the electronic structure and the corresponding molecular orbitals of Ag_9Fe^- along with the optimized geometric structure. The electronic structure revealed that the 3d orbital of the Fe atom are separated from sp orbitals of Ag and Fe. The contours of the molecular orbitals illustrate that the 3d orbital are located on the Fe atom. These results are similar to those of Cr- and Mn-doped 18-e clusters. On the other hand, $\text{Ag}_{11}\text{Fe}^+$ exhibits features common with Sc-, Ti-, and V-doped clusters. Figure 4.13(a) shows the geometric structure of $\text{Ag}_{11}\text{Fe}^+$, where the doped Fe is almost encapsulated by Ag atoms. The corresponding electronic structure (Fig. 4.13b) reveals that the energy levels of Fe 3d orbital overlaps with sp orbital of Ag and Fe. The contours of the molecular orbitals (Fig. 4.13c) illustrate 1S, 1P, and 1D superatomic orbitals, which accommodate 18 valence electrons.

M = Co. The differences between Ag_9Fe^- and $\text{Ag}_{11}\text{Fe}^+$ are common to Co-doped clusters. As for the 18-e anion, Ag_8Co^- , 3d orbitals of the dopant are separated

from sp orbitals of Ag and Co, and are localized on the Co atom as shown in Fig. 4.14b. For the cationic 18-e cluster, $\text{Ag}_{10}\text{Co}^+$, the most stable isomer is a singlet state with an endohedral geometry as shown in Fig. 4.15(a). The electronic structure (Fig. 4.15b) shows that the 3d orbital of the dopant overlap sp orbitals of Ag and Co. The contours of the molecular orbitals (Fig. 4.15c) illustrate 1S, 1P, and 1D superatomic orbitals, which are occupied by 18 valence electrons.

M = Ni. The differences between anions and cations in Fe- and Co-doped 18-e clusters are also common to Ni-doped clusters. Figure 4.16 shows the electronic structure and the molecular orbitals of Ag_7Ni^- , which are calculated by B3LYP functional instead of B3LYP* functional. The results revealed that 3d orbitals of the dopant are separated from sp orbitals of Ag and Ni, and are located on the Ni atom. For the cations, the most stable isomer is a singlet state with an endohedral geometry as shown in Fig. 4.17(a). The electronic structure of Ag_9Ni^+ (Fig. 4.17b) shows that 3d orbital of the dopant overlaps with sp orbitals of Ag and Ni. The contours of the molecular orbitals (Fig. 4.17c) illustrate 1S, 1P, and 1D superatomic orbitals, which are occupied by 18 valence electrons.

4.4. Discussion

For all dopants in both the charge states, the small sized clusters show reactivity about 10^5 times higher than that of Ag_8^+ . The dopant M enhances the reactivity of silver clusters because the M atom acts as an active site. DFT calculations for highly reactive clusters, *e.g.*, Ag_7Ni^- , Ag_8Co^- , and Ag_9Fe^- revealed that 3d electrons may be localized on the doped atom. Therefore, the localized 3d electrons may affect the reactivity. In the section, the author will discuss the size-dependent reactivity, focusing especially on 18-e clusters.

4.4.1. Category 1; M = Sc, Ti, and V

For Sc-doped cluster ions, $\text{Ag}_{16}\text{Sc}^+$ and $\text{Ag}_{14}\text{Sc}^-$ show the lowest reactivity, both of which have 18 valence electrons. It is speculated that the Sc 3d electron must be delocalized both in the cation and in the anion to form the closed electronic shell with the 18 electrons. DFT calculations for these cluster ions supported the speculation as shown in Figs. 4.2 and 4.3. These clusters possess endohedral geometries with the encapsulated Sc. It is revealed that the Sc 3d orbital hybridizes with sp orbitals of Ag and Sc to form superatomic orbitals, which accommodate 18 valence electrons resulting in a singlet state. Neutral Ag_NSc clusters have been investigated by DFT calculations in the size range $N = 1-16$.^[81] It was shown that the most stable 18-e cluster, Ag_{15}Sc , is in a singlet state with an endohedral geometry, the largest HOMO-LUMO gap, and the smallest H_2 adsorption energy. Therefore, it is suggested that the 3d electron in $\text{Ag}_N\text{Sc}^{+/0/-}$ must be delocalized at least at $N = 16, 15, 14$ for the cation, the neutral, and the anion, respectively.

In common to $\text{Ag}_N\text{Sc}^{+/0/-}$, the 18-e clusters, $\text{Ag}_{15}\text{Ti}^+$, $\text{Ag}_{13}\text{Ti}^-$, Ag_{14}V^+ , and Ag_{12}V^- , exhibited the reactivity minimum, suggesting that the 3d electrons may be delocalized to form the closed electronic structure. The closed electronic shell is supported by the DFT calculations in Figs. 4.4–4.7, where superatomic orbitals of 1S, 1P, and 1D are clearly formed similar to $\text{Ag}_{16}\text{Sc}^+$ and $\text{Ag}_{14}\text{Sc}^-$. As for neutral species, it is reported that the most stable Ag_{14}Ti is in a closed-shell singlet state possessing an endohedral geometry with a D_{6d} symmetry,^[72] which is similar to $\text{Ag}_{14}\text{Sc}^-$ and Ag_{14}V^+ .

To summarize, the electron counting plays a role at the magic sizes for Sc-, Ti-, and V-doped clusters, where 3d electrons are delocalize to occupy superatomic orbitals resulting in the closed electronic shell with 18 valence electrons.

4.4.2. Category 2; M = Fe, Co, and Ni

In contrast to the above early 3d transition metals, late-transition-metal-doped systems resulted in different behavior. The 18-e cluster cations showed the lowest

reactivity, whereas the corresponding anions exhibited high reactivity comparable to neighboring sizes. DFT calculations for these cations revealed that 1S, 1P, and 1D superorbitals are formed by hybridization of M 3d orbital with sp orbitals of Ag and M, which are occupied by 18 electrons resulting in the closed electronic shell as shown in Figs. 4.13, 4.15, and 4.17. Thus, the electron counting effect is valid to these cations. The geometric structures showed endohedral geometries with an encapsulated dopant in similar to the Sc-, Ti-, and V-doped clusters. On the other hand, the electronic structure of the anions is spin polarized with an open shell because 3d orbital is separated from sp orbitals of Ag and M. The molecular orbitals shown in Figs. 4.12, 4.14, and 4.16 illustrate that the M 3d orbital is essentially localized on the M atom located on the surface of the cluster. Therefore, the 3d electrons are encourage to delocalize in the endohedral 18-electrons cation, whereas they tend to localize in the exohedral 18-electron anions. Then, it was found that encapsulation of the dopant atom is necessary for 3d electrons to contribute to electron counting via delocalization. It has been reviewed recently that the endohedral geometry has a significant influence on enhanced stability, magnetic properties, HOMO-LUMO gaps, etc.^[33] Here, it is found that the endohedral geometry also influences delocalization of 3d electrons of the dopant.

4.4.3. Category 3; M = Cr and Mn

For Cr- and Mn-doped clusters, neither cationic nor anionic 18-e clusters exhibited a minimum in the reactivity in contrast to the above elements. DFT calculations for these cluster cations (Figs. 4.9 and 4.11) showed that most of 3d orbital are separated from sp orbitals of Ag and M, even though the dopant is encapsulated. The electronic structure of these cations revealed that 3d electrons occupy five majority-spin states. For anionic 18-e clusters, the dopant is located on the surface of the clusters as shown in Figs. 4.8 and 4.10, and its electronic structure illustrated that 3d electrons occupy five majority-spin states in common to cations. The previous study for Ag_NM^+ pointed out the stability of the half-filled 3d orbital of Cr and Mn that is hard to

delocalize.^[37,46] Therefore, the missing reactivity minimum at 18-e clusters is ascribed to the half-filled nature of the 3d orbital.

4.5. Summary

In this chapter, the author reported the size-dependent reactivity of $\text{Ag}_N\text{M}^{+/-}$ ($\text{M} = \text{Sc-Ni}$) to investigate localization/delocalization of 3d electrons. Small sized clusters showed reactivity higher than that of Ag_8^+ because the dopant M acts an active site, where 3d electrons may be localized on the surface dopant M. Sc-, Ti-, and V-doped cations and anions exhibited minimum reactivity at the magic sizes, which have 18 valence electrons. For Fe-, Co-, and Ni-doping, the cationic 18-e clusters also showed a minimum in the size-dependent reactivity. The stability of these clusters was attributed to the closed electronic structure with delocalized 3d electrons. In contrast, Ag_9Fe^- , Ag_8Co^- , and Ag_7Ni^- were highly reactive as well as neighboring sizes, even though these ions are 18-e clusters. DFT calculations revealed that the transition-metal atom is endohedrally doped in the former stable clusters, whereas the dopant M is located on the surface of the cluster. Thus, it is concluded that the electron counting rule works only when the dopant atom is encapsulated by the host Ag atoms. For Cr- and Mn-doping, the half-filled 3d orbital of Cr and Mn is so stable that 3d electrons are localized both in endohedral $\text{Ag}_{13}\text{Cr}^+$ and $\text{Ag}_{12}\text{Mn}^+$ and in exohedral $\text{Ag}_{11}\text{Cr}^-$ and $\text{Ag}_{10}\text{Mn}^-$.

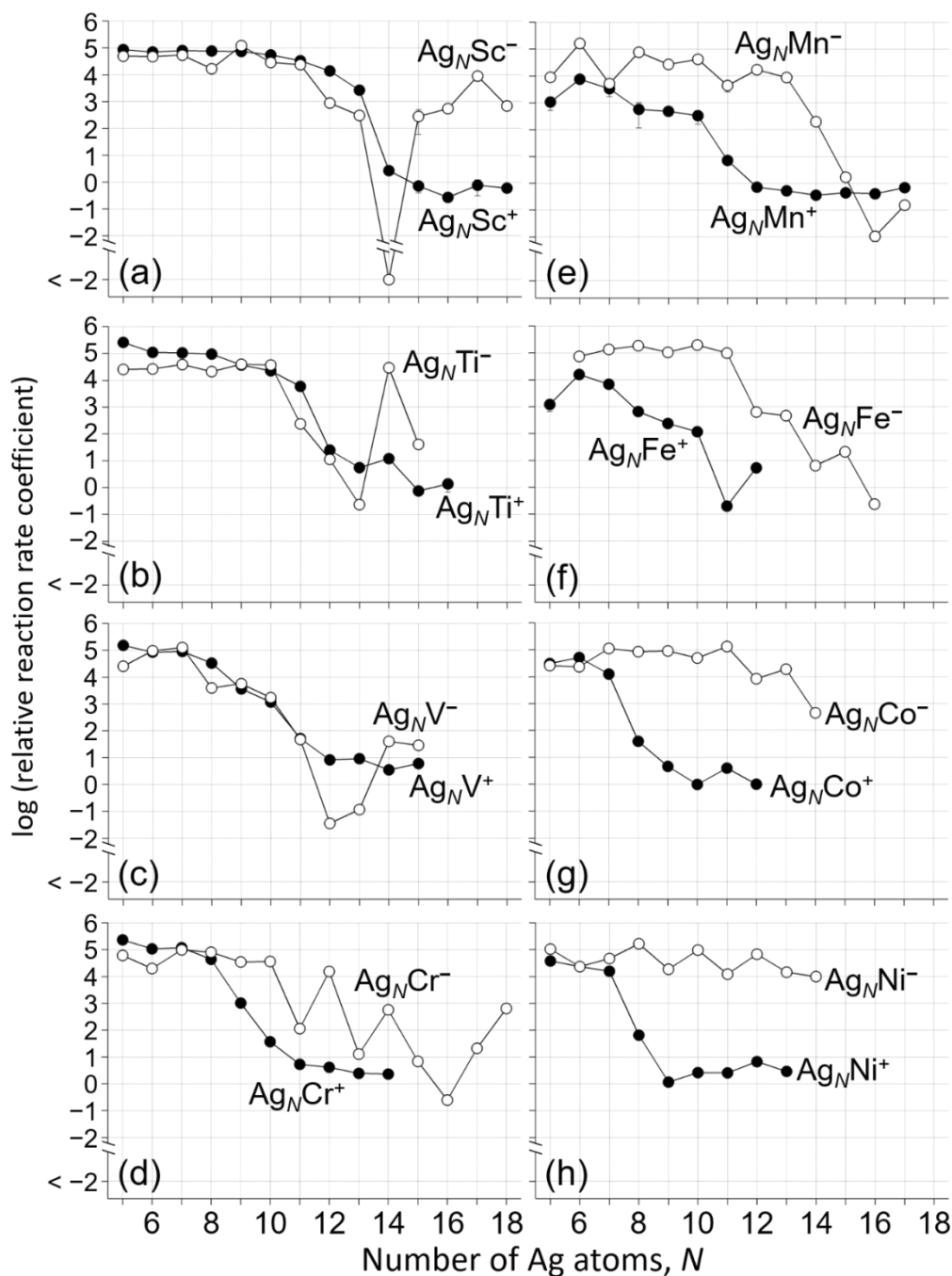


Figure 4.1. Reaction-rate coefficients of cations (solid circles) and anions (open circles) of Ag_NM ($\text{M} = \text{Sc-Ni}$) in reaction with O_2 as a function of the number of Ag atoms. The rate coefficients are relative value with respect to that of Ag_8^+ . The value $<10^{-2}$ indicates that no product ions are observed.

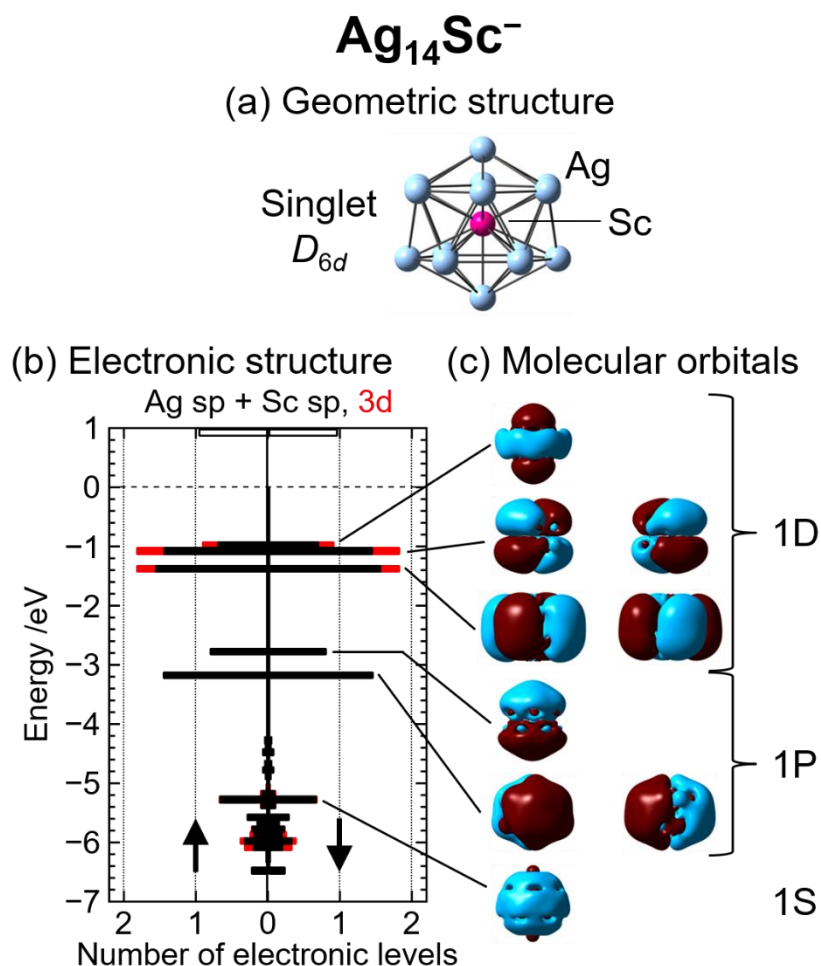


Figure 4.2. Results of DFT calculations on Ag₁₄Sc⁻. Panel (a): the optimized geometric structure along with its symmetry and spin multiplicity, which is reproduced from Fig. 3.12. Panel (b): the electronic structure depicted by density-of-state (DOS) diagrams for majority and minority spins. Bars in black and red show the DOS of sp and 3d orbitals, respectively. The number of electronic levels is shown by histograms with 0.1-eV energy windows. The dashed line at 0 eV represents the chemical potential, below which the levels are occupied. Panel (c): isosurfaces of molecular-orbital wave functions with isovalue of 0.0035.

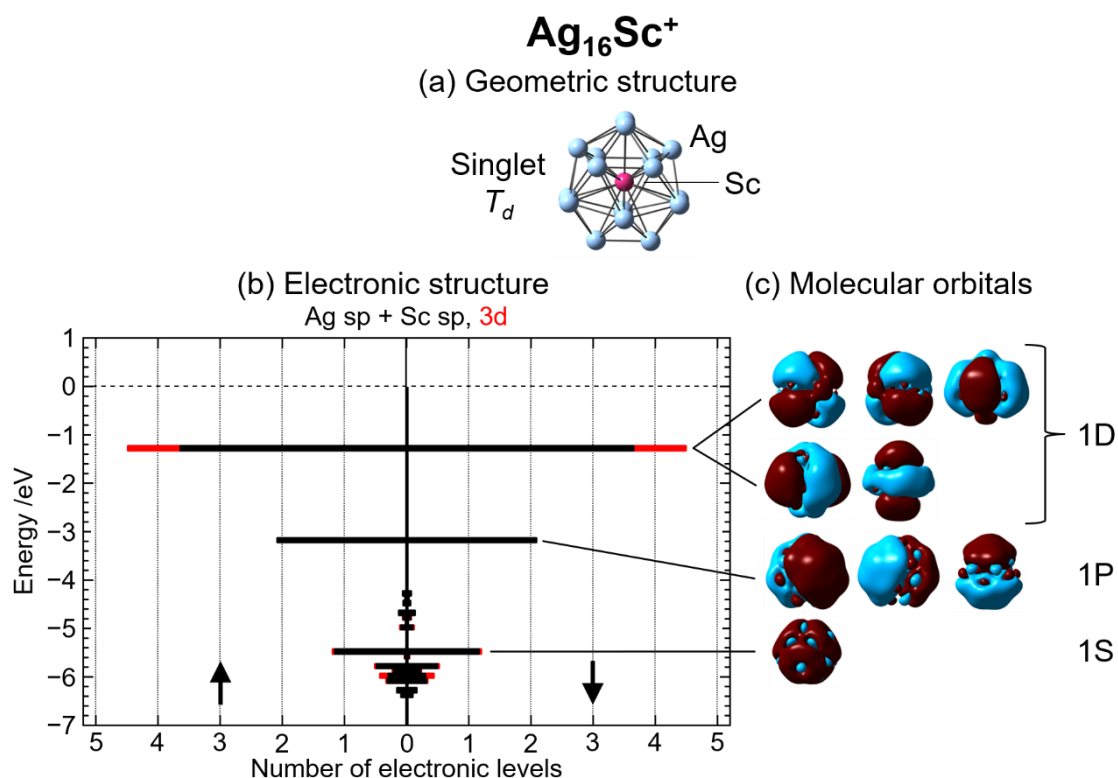


Figure 4.3. Results of DFT calculations on $\text{Ag}_{16}\text{Sc}^+$. Panel (a): the optimized geometric structure along with its symmetry and spin multiplicity. Panel (b): the electronic structure depicted by density-of-state (DOS) diagrams for majority and minority spins. Bars in black and red show the DOS of sp and 3d orbitals, respectively. The number of electronic levels is shown by histograms with 0.1-eV energy windows. The dashed line at 0 eV represents the chemical potential, below which the levels are occupied. Panel (c): isosurfaces of molecular-orbital wave functions with isovalue of 0.0035.

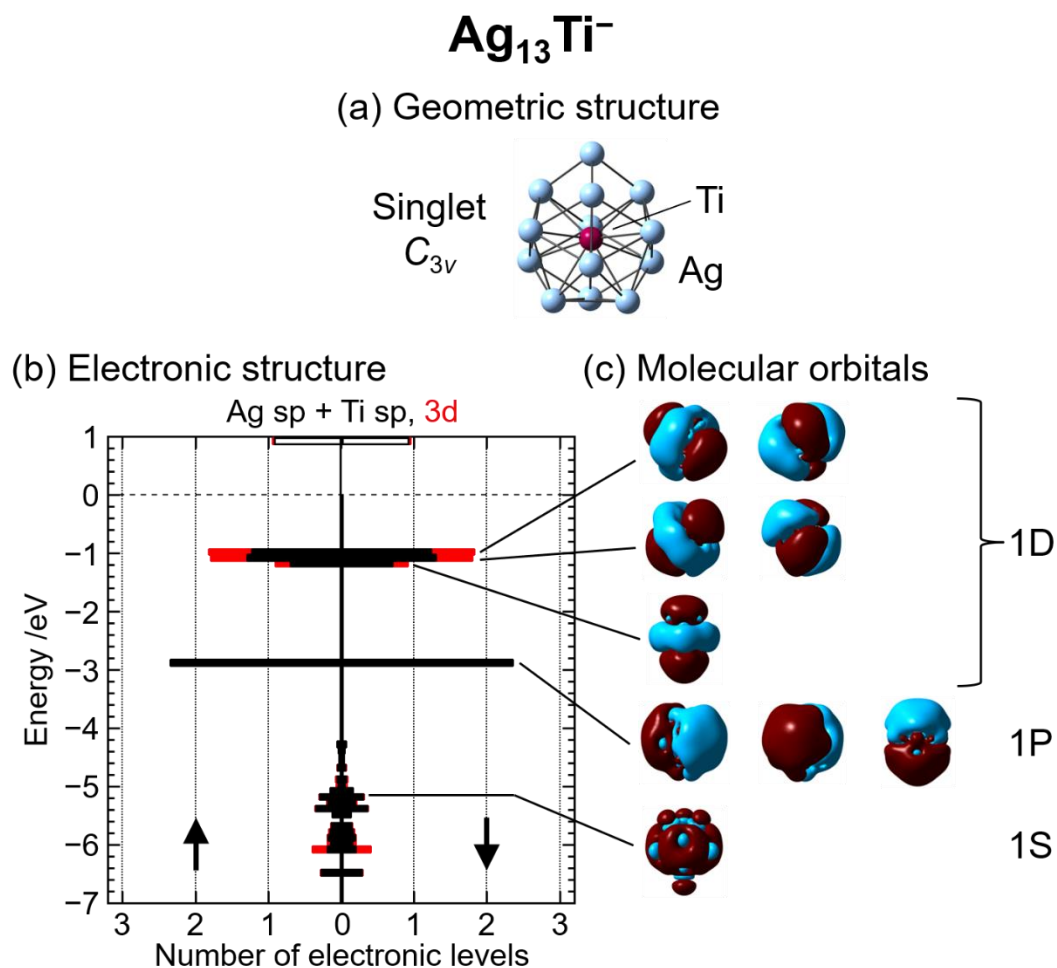


Figure 4.4. Results of DFT calculations on Ag₁₃Ti⁻. Panel (a): the optimized geometric structure along with its symmetry and spin multiplicity, which is reproduced from Fig. 3.12. Panel (b): the electronic structure depicted by density-of-state (DOS) diagrams for majority and minority spins. Bars in black and red show the DOS of sp and 3d orbitals, respectively. The number of electronic levels is shown by histograms with 0.1-eV energy windows. The dashed line at 0 eV represents the chemical potential, below which the levels are occupied. Panel (c): isosurfaces of molecular-orbital wave functions with isovalue of 0.0035.

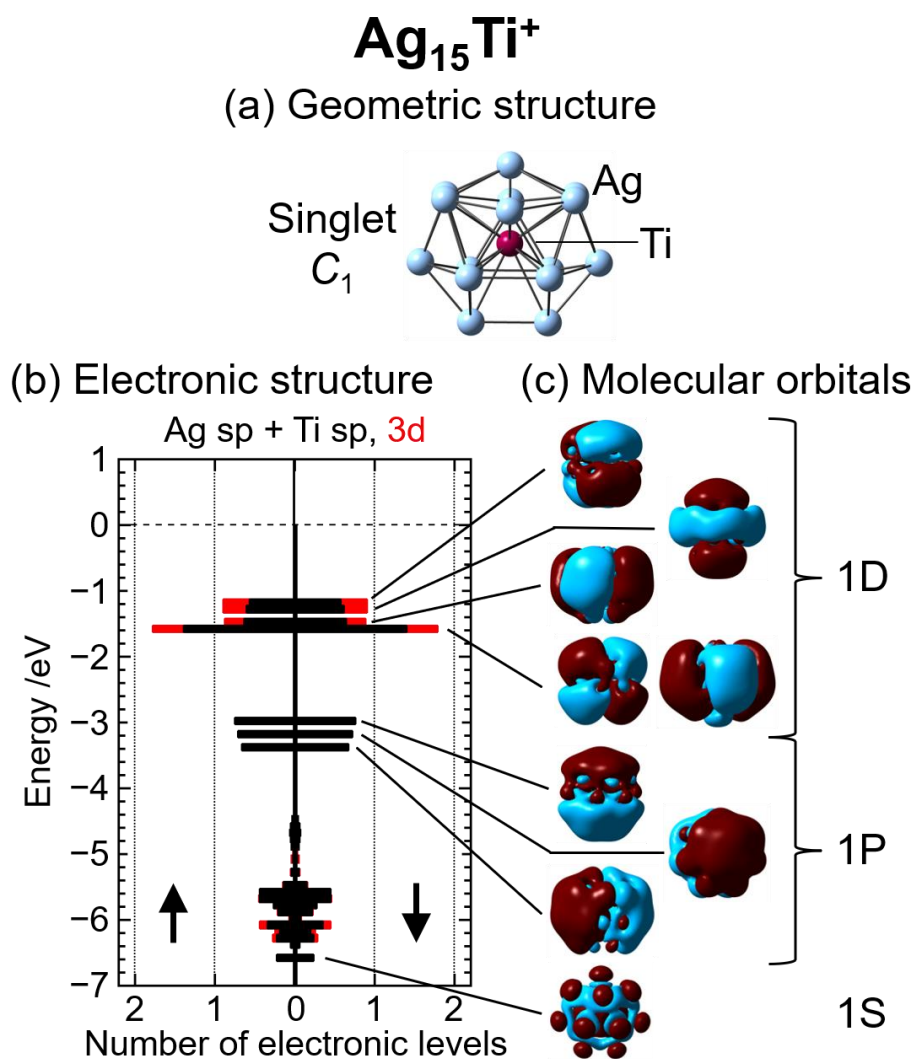


Figure 4.5. Results of DFT calculations on Ag₁₅Ti⁺. Panel (a): the optimized geometric structure along with its symmetry and spin multiplicity. Panel (b): the electronic structure depicted by density-of-state (DOS) diagrams for majority and minority spins. Bars in black and red show the DOS of sp and 3d orbitals, respectively. The number of electronic levels is shown by histograms with 0.1-eV energy windows. The dashed line at 0 eV represents the chemical potential, below which the levels are occupied. Panel (c): isosurfaces of molecular-orbital wave functions with isovalue of 0.0035.

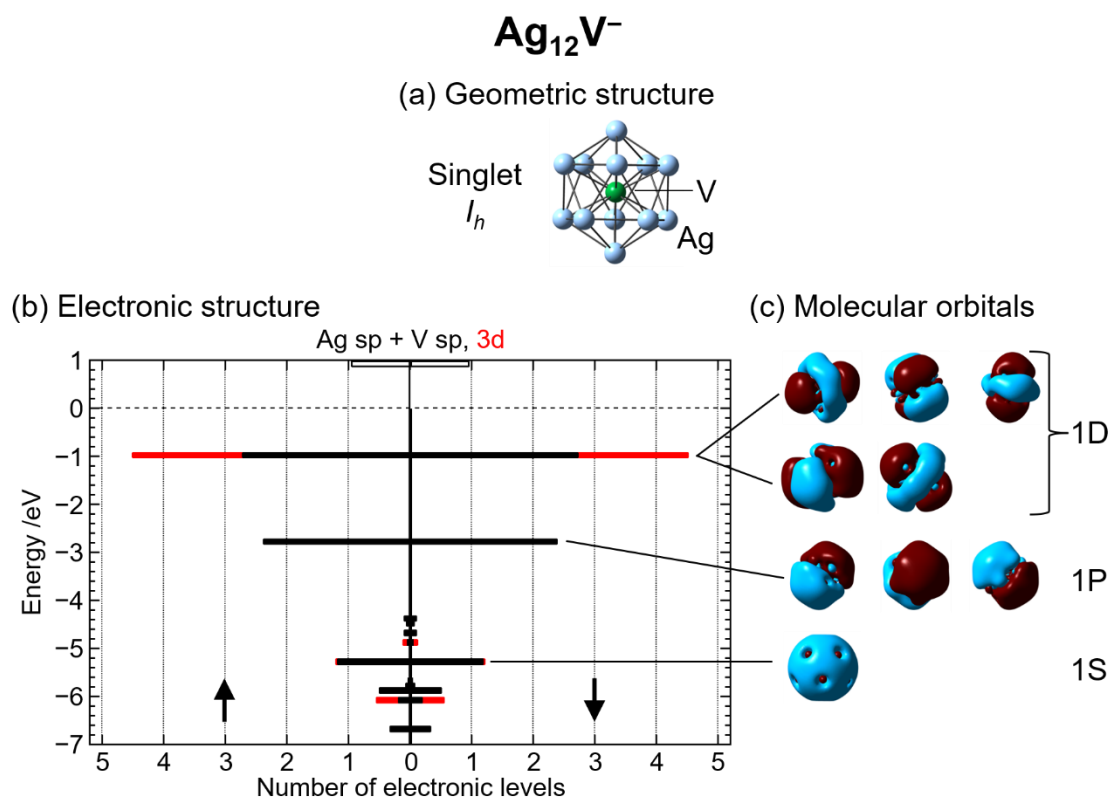


Figure 4.6. Results of DFT calculations on Ag₁₂V⁻. Panel (a): the optimized geometric structure along with its symmetry and spin multiplicity, which is reproduced from Fig. 3.12. Panel (b): electronic structure depicted by density-of-state (DOS) diagrams for majority and minority spins. Bars in black and red show the DOS of sp and 3d orbitals, respectively. The number of electronic levels is shown by histograms with 0.1-eV energy windows. The dashed line at 0 eV represents the chemical potential, below which the levels are occupied. Panel (c): isosurfaces of molecular-orbital wave functions with isovalue of 0.0035.

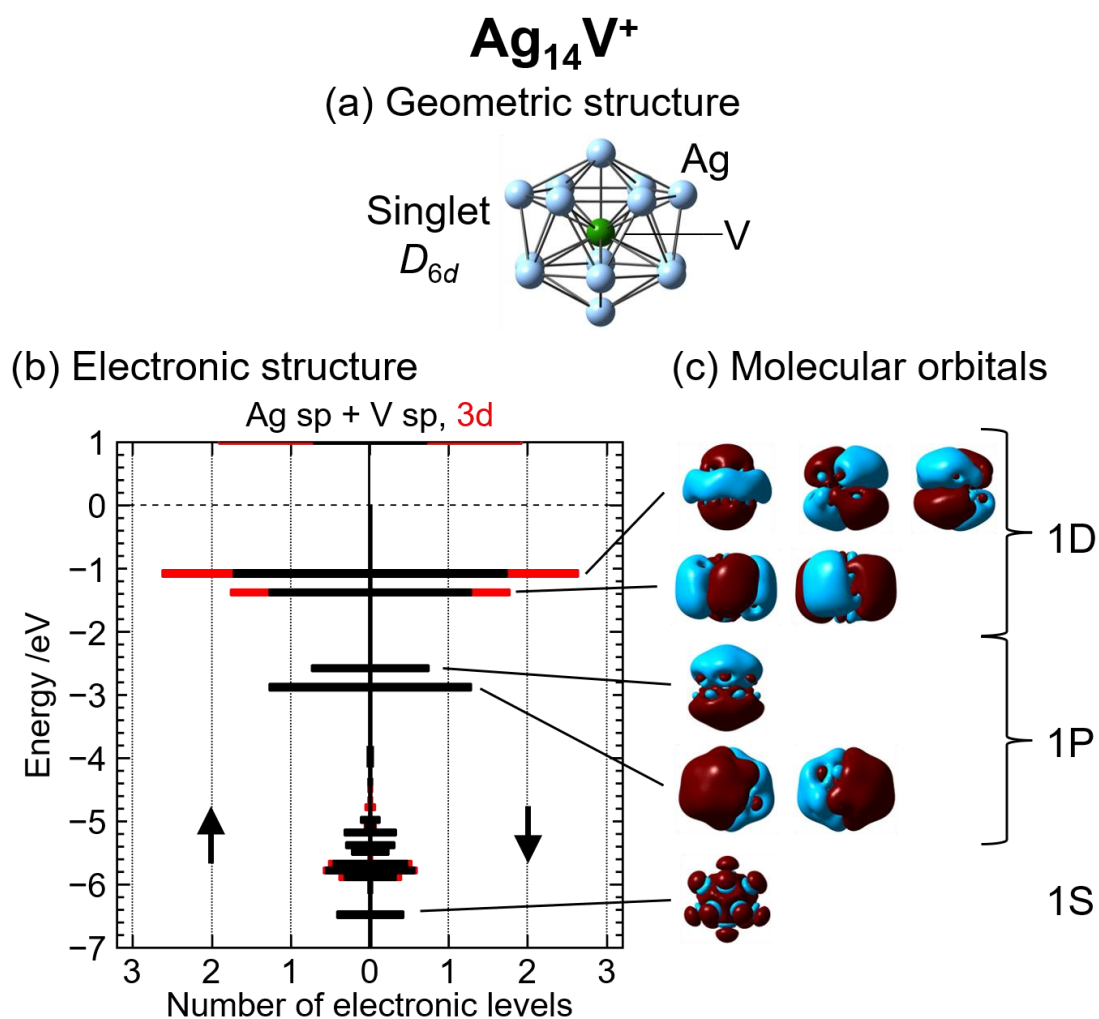


Figure 4.7. Results of DFT calculations on Ag₁₄V⁺. Panel (a): the optimized geometric structure along with its symmetry and spin multiplicity. Panel (b): the electronic structure depicted by density-of-state (DOS) diagrams for majority and minority spins. Bars in black and red show the DOS of sp and 3d orbitals, respectively. The number of electronic levels is shown by histograms with 0.1-eV energy windows. The dashed line at 0 eV represents the chemical potential, below which the levels are occupied. Panel (c): isosurfaces of molecular-orbital wave functions with isovalue of 0.0035.

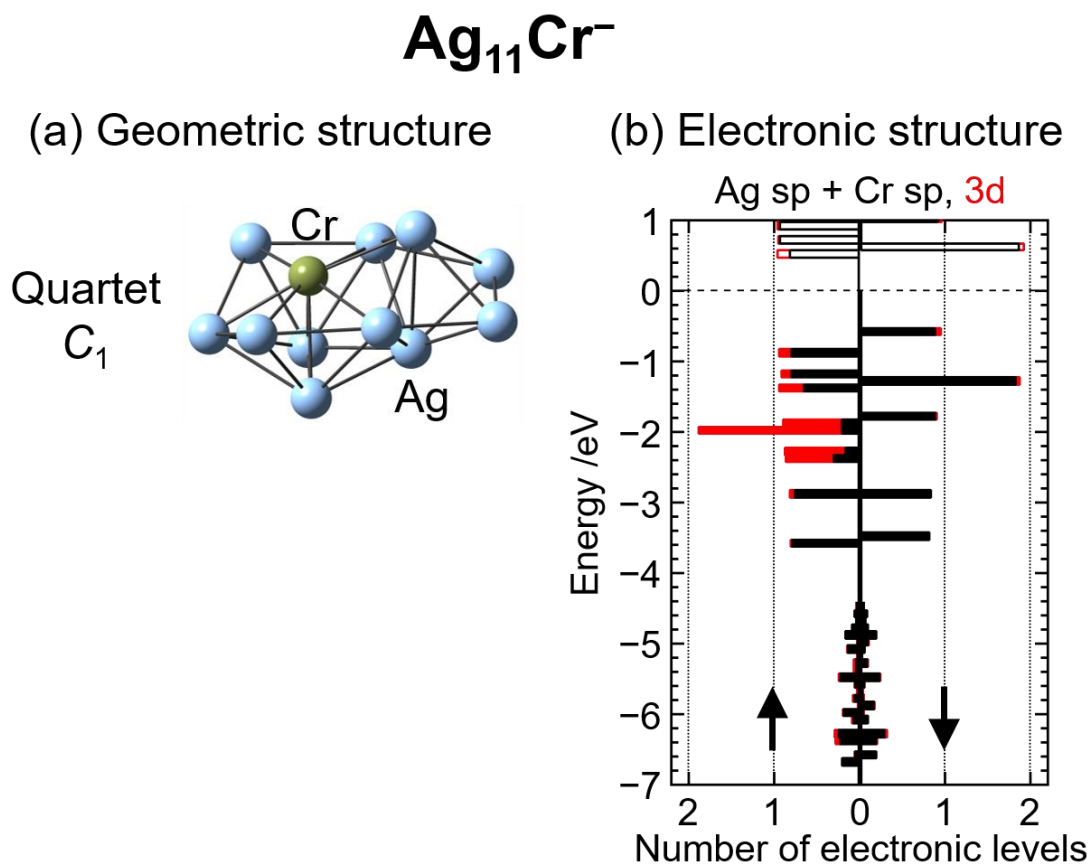


Figure 4.8. Results of DFT calculations on $\text{Ag}_{11}\text{Cr}^-$. Panel (a): the optimized geometric structure along with its symmetry and spin multiplicity, which is reproduced from Fig. 3.12. Panel (b): the electronic structure depicted by density-of-state (DOS) diagrams for majority and minority spins. Bars in black and red show the DOS of sp and 3d orbitals, respectively. The number of electronic levels is shown by histograms with 0.1-eV energy windows. The dashed line at 0 eV represents the chemical potential, below which the levels are occupied.

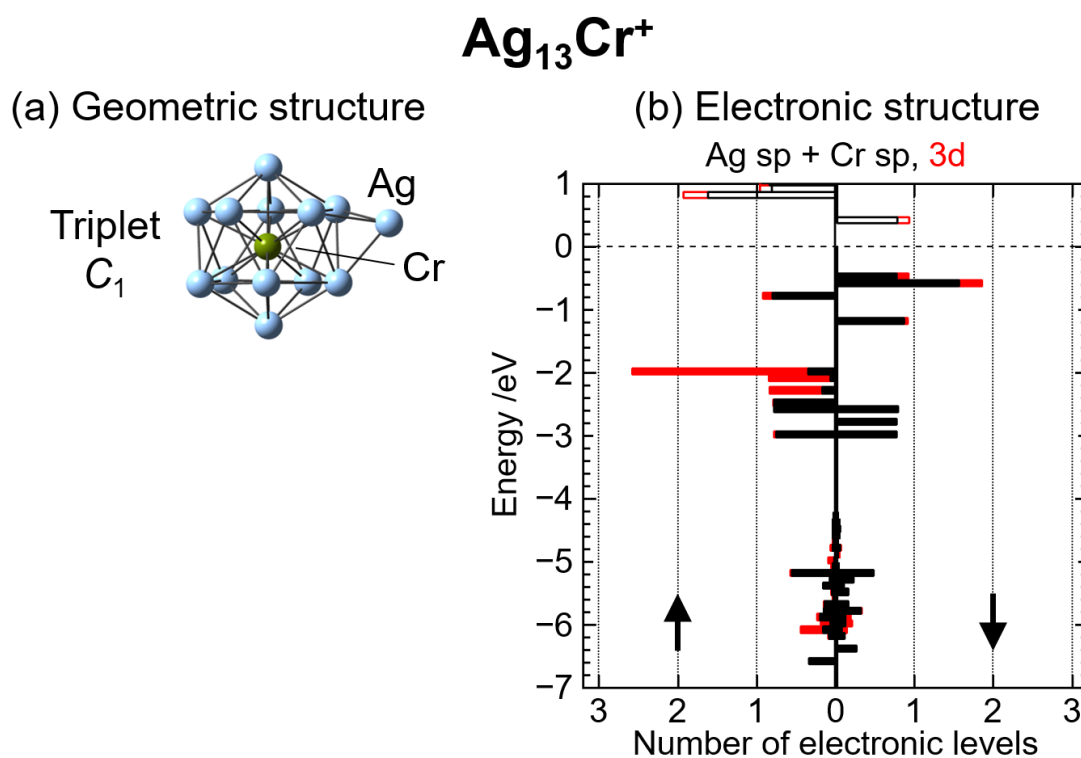


Figure 4.9. Results of DFT calculations on Ag₁₃Cr⁺. Panel (a): the optimized geometric structure along with its symmetry and spin multiplicity. Panel (b): the electronic structure depicted by density-of-state (DOS) diagrams for majority and minority spins. Bars in black and red show the DOS of sp and 3d orbitals, respectively. The number of electronic levels is shown by histograms with 0.1-eV energy windows. The dashed line at 0 eV represents the chemical potential, below which the levels are occupied.

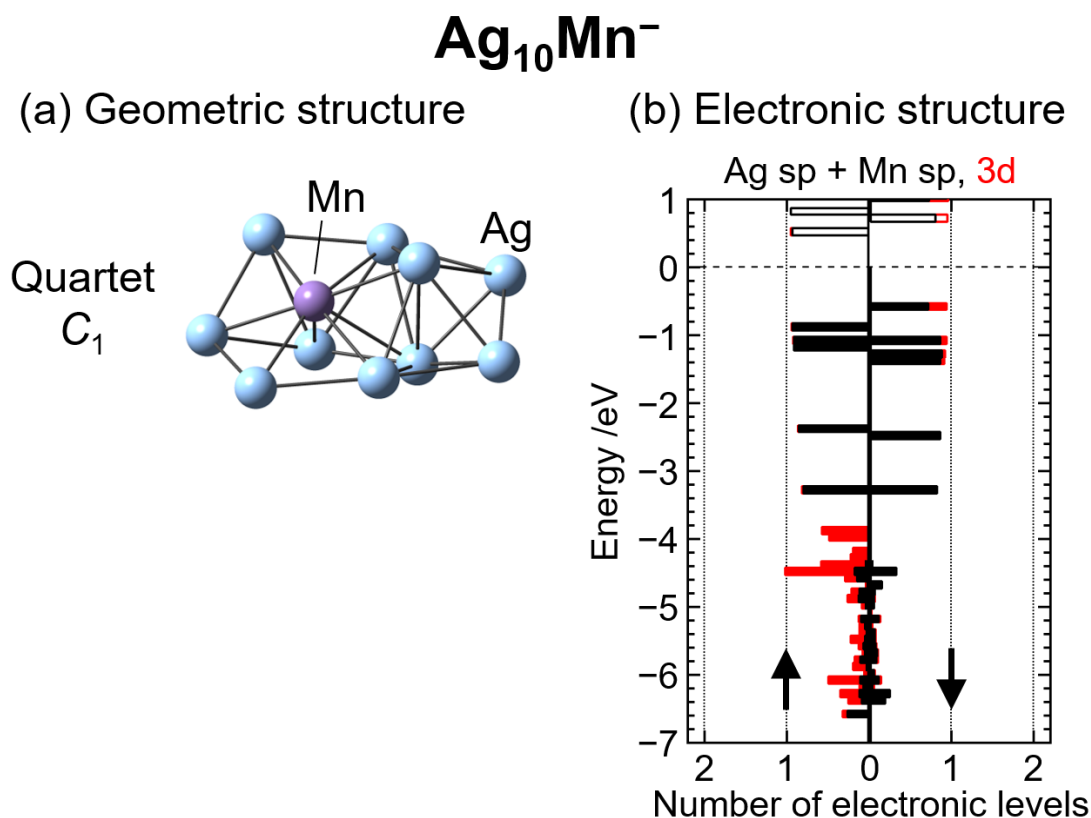


Figure 4.10. Results of DFT calculations on Ag₁₀Mn⁻. Panel (a): the optimized geometric structure along with its symmetry and spin multiplicity, which is reproduced from Fig. 3.12. Panel (b): the electronic structure depicted by density-of-state (DOS) diagrams for majority and minority spins. Bars in black and red show the DOS of sp and 3d orbitals, respectively. The number of electronic levels is shown by histograms with 0.1-eV energy windows. The dashed line at 0 eV represents the chemical potential, below which the levels are occupied.

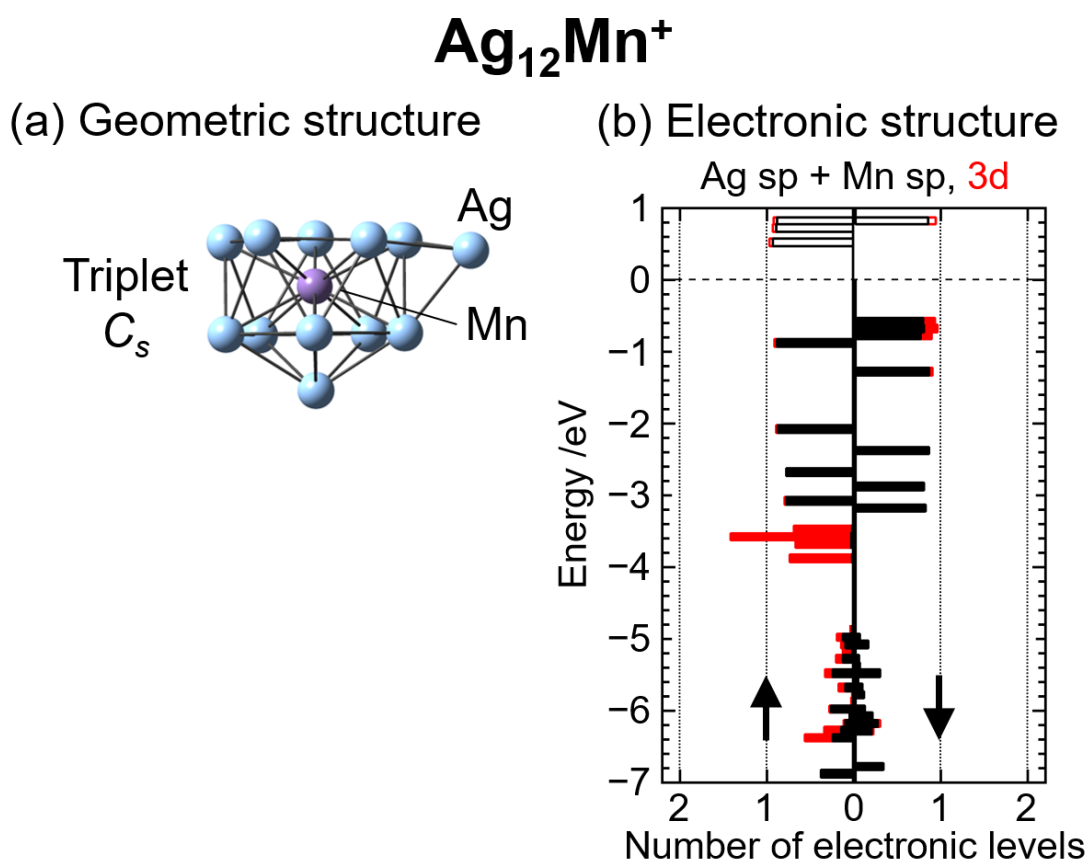


Figure 4.11. Results of DFT calculations on Ag₁₂Mn⁺. Panel (a): the optimized geometric structure along with its symmetry and spin multiplicity. Panel (b): the electronic structure depicted by density-of-state (DOS) diagrams for majority and minority spins. Bars in black and red show the DOS of sp and 3d orbitals, respectively. The number of electronic levels is shown by histograms with 0.1-eV energy windows. The dashed line at 0 eV represents the chemical potential, below which the levels are occupied.

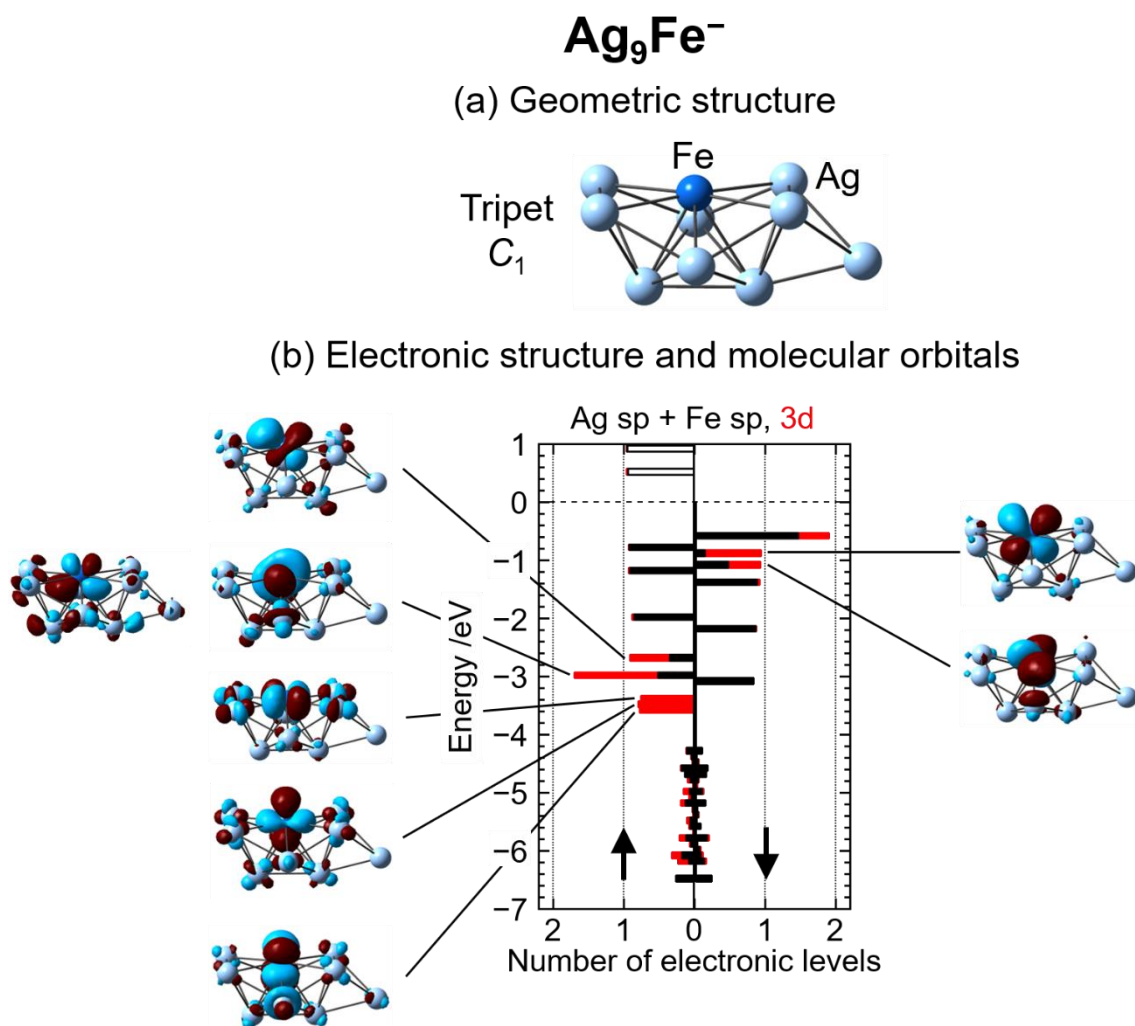


Figure 4.12. Results of DFT calculations on Ag₉Fe⁻. Panel (a): the optimized geometric structure along with its symmetry and spin multiplicity, which is reproduced from Fig. 3.12. Panel (b): electronic structure and isosurfaces of molecular-orbital wave functions. The electronic structure is depicted by density-of-states (DOS) diagrams for majority and minority spins. Bars in the diagrams show the DOS of sp and 3d orbitals by black and red, respectively. The number of electronic levels is shown by histograms with 0.1-eV energy windows. The dashed line at 0 eV represents the chemical potential, below which the levels are occupied. The isovalue of molecular orbitals is 0.03.

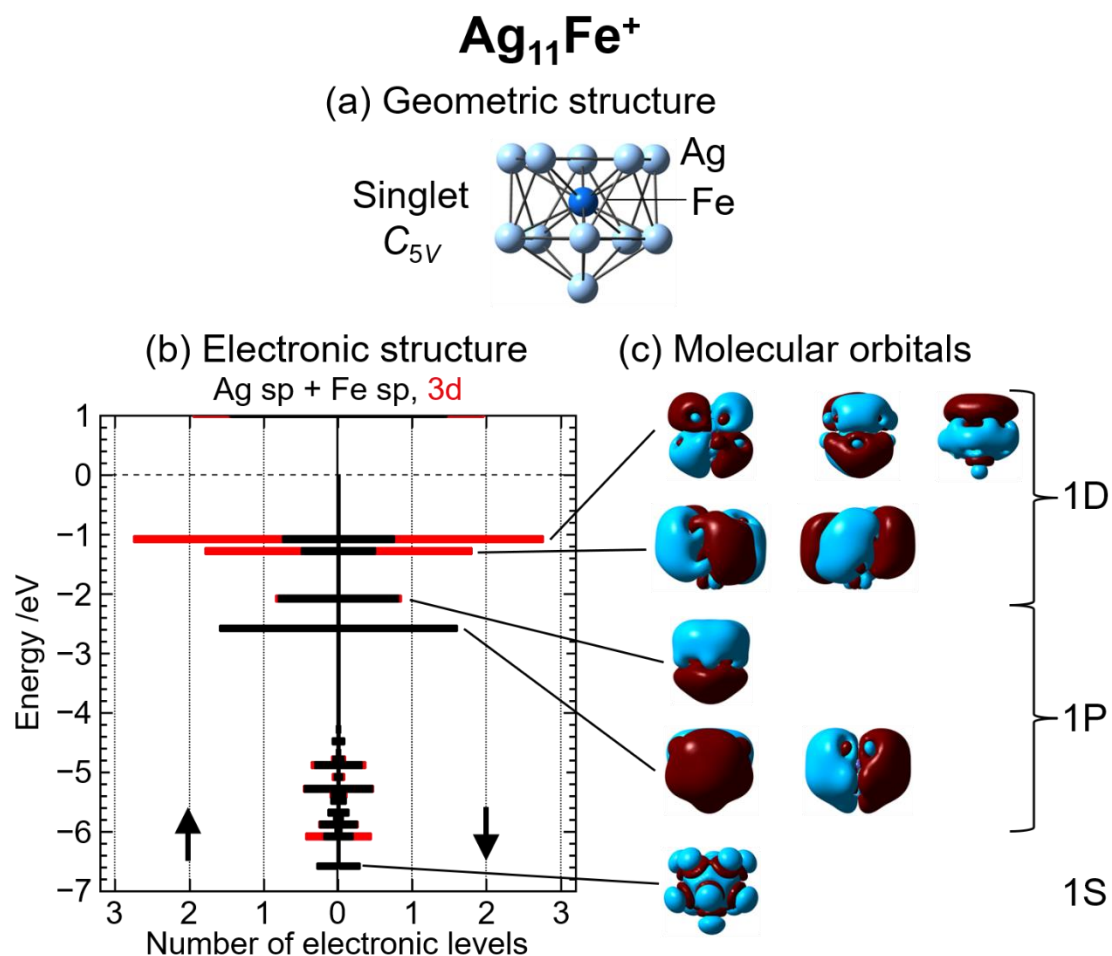


Figure 4.13. Results of DFT calculations on Ag₁₁Fe⁺. Panel (a): the optimized geometric structure along with its symmetry and spin multiplicity. Panel (b): the electronic structure depicted by density-of-state (DOS) diagrams for majority and minority spins. Bars in black and red show the DOS of sp and 3d orbitals, respectively. The number of electronic levels is shown by histograms with 0.1-eV energy windows. The dashed line at 0 eV represents the chemical potential, below which the levels are occupied. Panel (c): isosurfaces of molecular-orbital wave functions with isovalue of 0.0035.

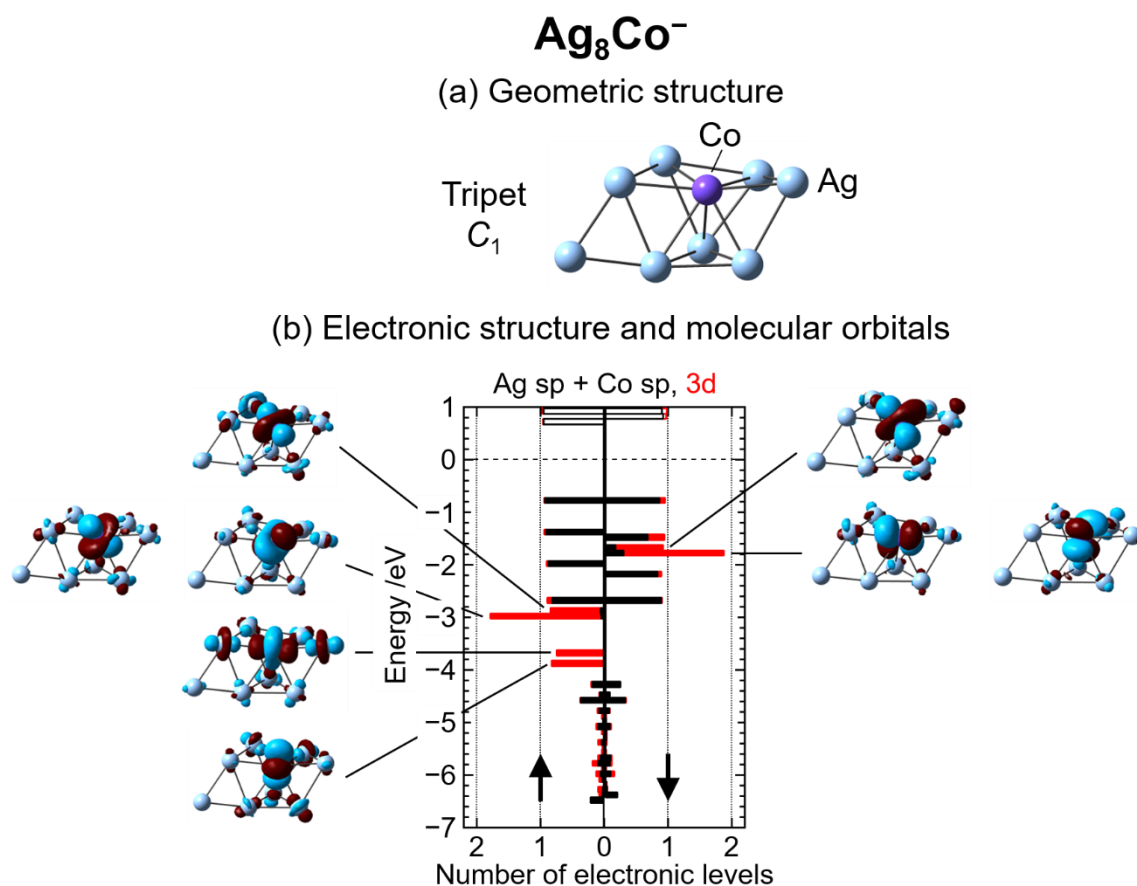


Figure 4.14. Results of DFT calculations on Ag₈Co⁻. Panel (a): the optimized geometric structure along with its symmetry and spin multiplicity, which is reproduced from Fig. 3.12. Panel (b): the electronic structure and isosurfaces of molecular-orbital wave functions. The electronic structure is depicted by density-of-states (DOS) diagrams for majority and minority spins. Bars in the diagrams show the DOS of sp and 3d orbitals by black and red, respectively. The number of electronic levels is shown by histograms with 0.1-eV energy windows. The dashed line at 0 eV represents the chemical potential, below which the levels are occupied. The isovalue of molecular orbitals is 0.03.

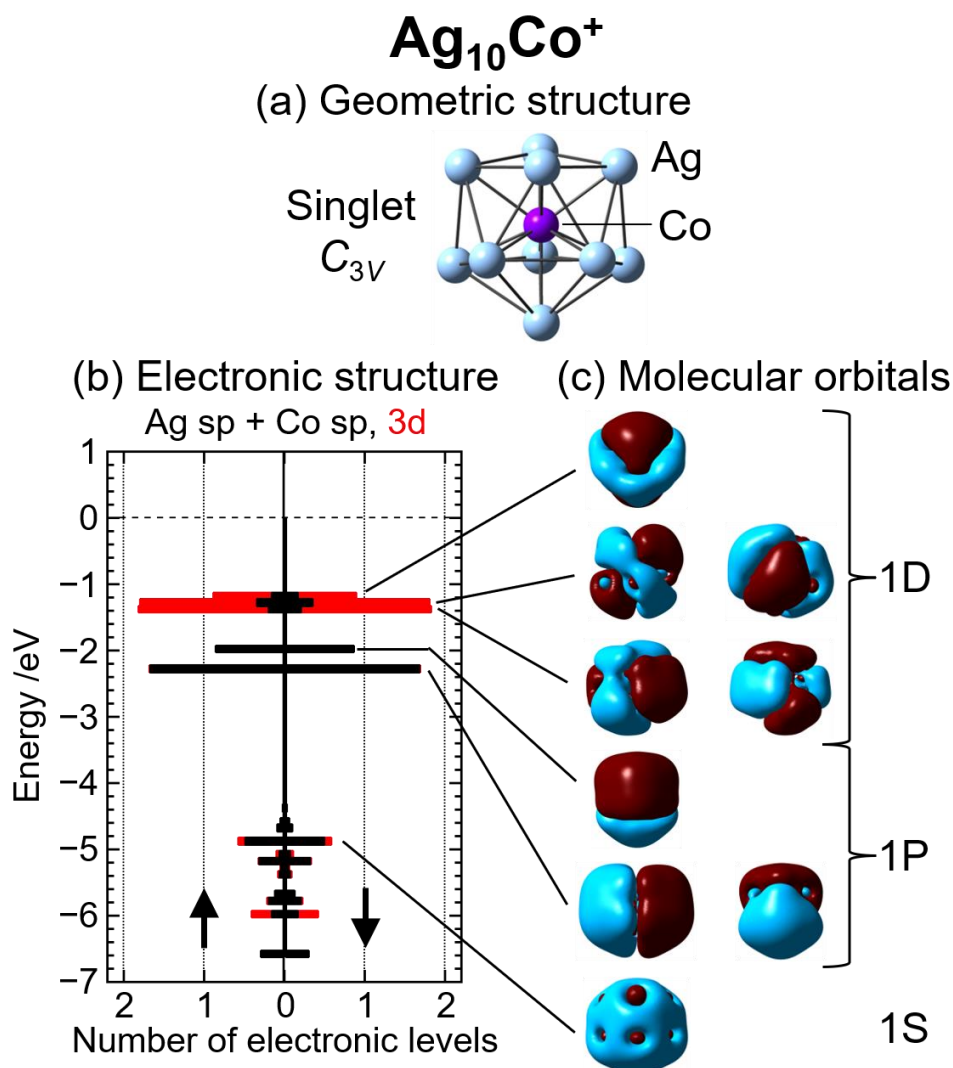


Figure 4.15. Results of DFT calculations on $\text{Ag}_{10}\text{Co}^+$. Panel (a): the optimized geometric structure along with its symmetry and spin multiplicity. Panel (b): the electronic structure depicted by density-of-state (DOS) diagrams for majority and minority spins. Bars in black and red show the DOS of sp and 3d orbitals, respectively. The number of electronic levels is shown by histograms with 0.1-eV energy windows. The dashed line at 0 eV represents the chemical potential, below which the levels are occupied. Panel (c): isosurfaces of molecular-orbital wave functions with isovalue of 0.0035.

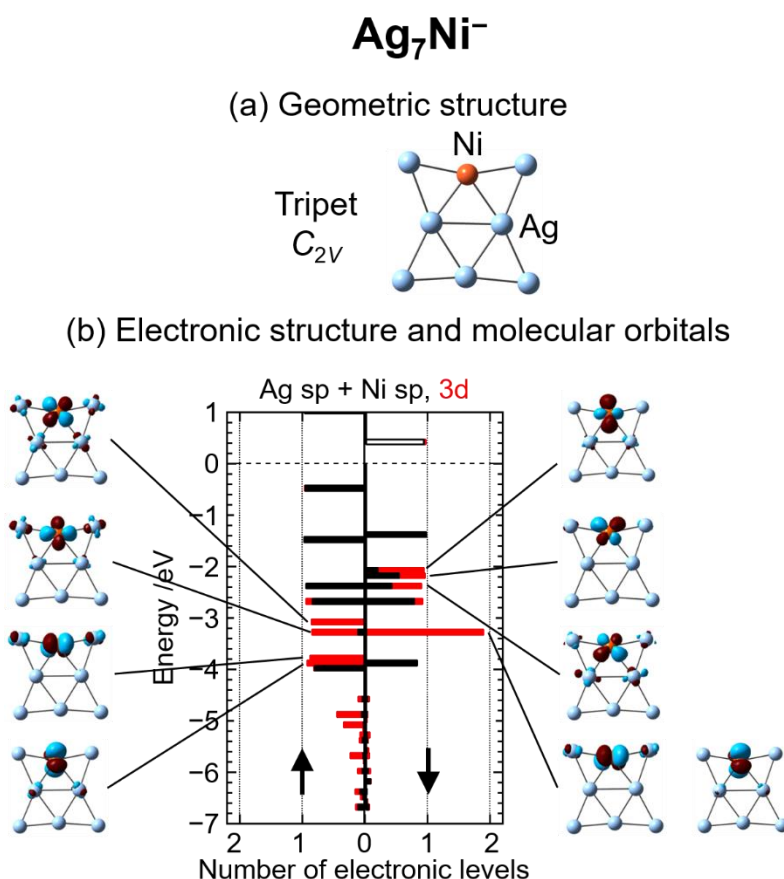


Figure 4.16. Results of DFT calculations on Ag₇Ni⁻. Panel (a): the optimized geometric structure along with its symmetry and spin multiplicity, which is reproduced from Fig. 3.12. Panel (b): the electronic structure and isosurfaces of molecular-orbital wave functions. Bars in black and red show the DOS of sp and 3d orbitals, respectively. The number of electronic levels is shown by histograms with 0.1-eV energy windows. The dashed line at 0 eV represents the chemical potential, below which the levels are occupied. The isovalue of molecular orbitals is 0.03. Note that the calculation of Ag₇Ni⁻ was performed with the B3LYP functional instead of B3LYP[★] employed for all other species; B3LYP[★] led Ag₇Ni⁻ to a spin-unpolarized singlet state with an endohedral geometry, which does not explain its high reactivity observed in the experiment.

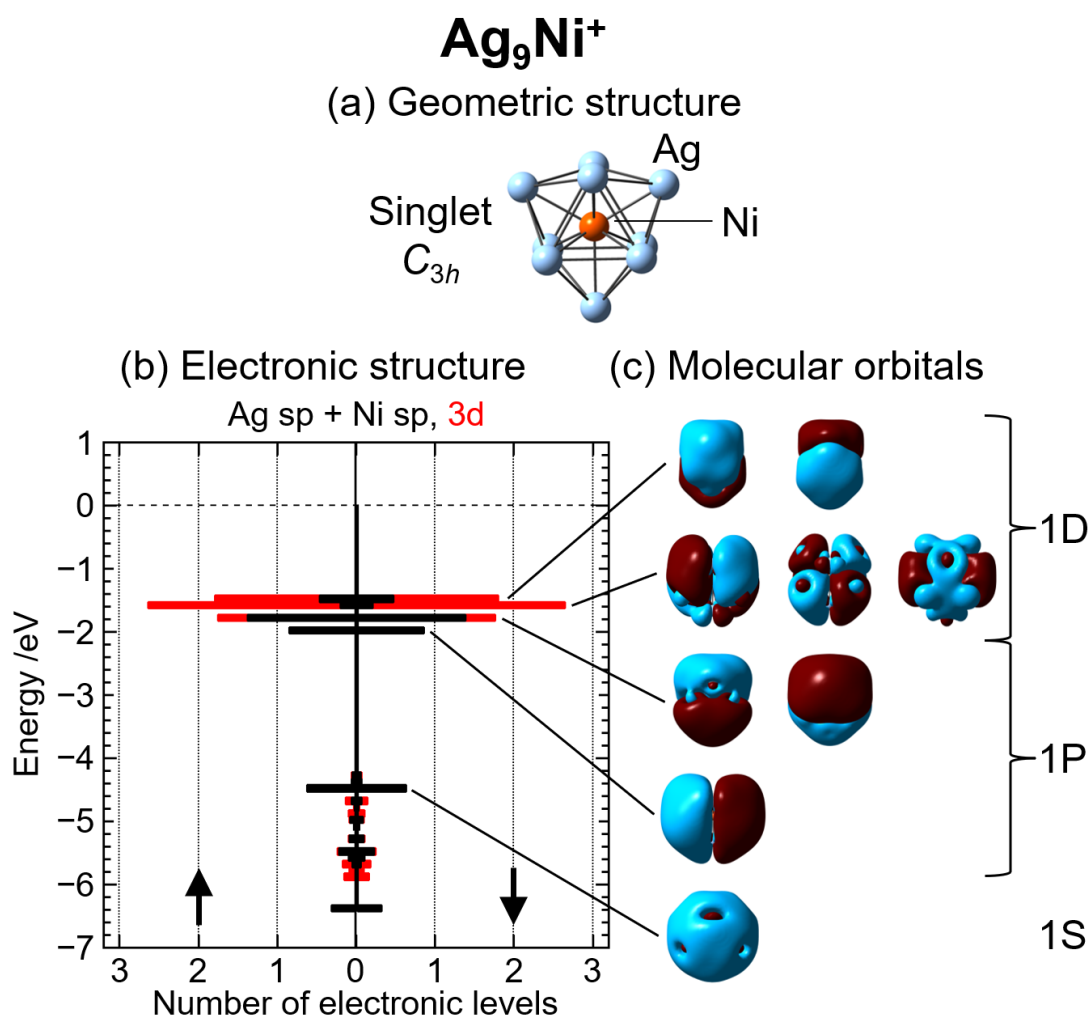


Figure 4.17. Results of DFT calculations on Ag₉Ni⁺. Panel (a): the optimized geometric structure along with its symmetry and spin multiplicity. Panel (b): the electronic structure depicted by density-of-state (DOS) diagrams for majority and minority spins. Bars in black and red show the DOS of sp and 3d orbitals, respectively. The number of electronic levels is shown by histograms with 0.1-eV energy windows. The dashed line at 0 eV represents the chemical potential, below which the levels are occupied. Panel (c): isosurfaces of molecular-orbital wave functions with isovalue of 0.0035.

Chapter 5. A Revisit to Electronic Structure of Ag_NCo^-

5.1. Introduction

Photoelectron spectroscopy is a gold standard to investigate electronic structures of anions because it allows determination of the electron binding energies (EBEs) of anions by the difference between photoelectron kinetic energy and photon energy of laser light. Firstly, Leopold and co-workers reported photoelectron spectra (PES) of mass-selected Cu_N^- ($N = 1-10$), which were produced in a flowing afterglow ion source and photodetached by a continuous-wave (CW) argon ion laser (2.540 or 2.707 eV).^[96] Electron affinities of Cu_N^- were evaluated by the corresponding PES, which agreed with those predicted by a simple effective radius of a conductive sphere. The series of the electron affinities showed odd–even alternation up to $N = 16$, where Cu_N^- with odd N have larger electron affinities than Cu_N^- with even N . They concluded that the observed alternations were consistent with the greater stability of a closed electronic shell with even electrons in odd atom clusters. For other metal cluster anions, *e.g.*, Ag_N^- , Au_N^- , Fe_N^- , Co_N^- , and Ni_N^- , the electronic and geometric structures have been investigated by photoelectron spectroscopy combined with DFT calculations.^[8,43,97–100]

The photoelectron spectroscopy combined with theoretical calculations is also applied to explore the electronic and geometric structures of 3d-transition-metal doped silver cluster anions that the author focuses on in the present thesis. Tono and co-workers investigated localization/delocalization of Co 3d electrons in Ag_NCo^- .^[47] DFT calculations for $N = 6, 7$, and 8 revealed that the Co atom is located at the center of the cluster, which is encapsulated by Ag atoms. The electronic structures of Ag_6Co^- and Ag_7Co^- showed that the energy levels of Co 3d orbitals are separated from those of sp ones of Ag and Co, suggesting an open electronic shell. On the other hand, theoretical calculations of Ag_8Co^- implied a closed electronic shell with 18 valence electrons. They simulated PES of these endohedral clusters, which reproduced the experimental PES. Therefore, they concluded that 3d electrons of the Co atom are delocalized in Ag_8Co^- to

form electronic shell closure. However, as described in Chapter 4, the reactivity measurement combined with the latest DFT calculations for Ag_8Co^- suggested that 3d electrons are localized on the Co atom, which is an active site at the surface of the cluster.

In this chapter, the author revisits electronic structures of Ag_NCo^- by theoretical calculations. DFT calculations are performed for $N = 4-9$ to discuss geometric and electronic structures. Time-dependent DFT (TDDFT) calculations are further performed for $N = 6-8$ to revise analysis of PES previously reported by Tono and co-workers.

5.2. Theoretical results

5.2.1. Geometric structures of Ag_NCo^- for $N = 4-9$

Details of theoretical procedures have been described in Chapter 2. The optimized geometric structures of Ag_NCo^- are shown in Fig. 5.1 along with spin multiplicity, symmetry, and a local magnetic moment on Co atom. Ag_4Co^- , Ag_5Co^- , and Ag_7Co^- prefer two-dimensional (2D) geometry, while the geometric structures of Ag_6Co^- , Ag_8Co^- , and Ag_9Co^- prefer three dimensions (3D) rather than 2D. The most stable isomer is the triplet and the doublet state for even N and odd N , respectively. The isomers for even N clusters with a singlet and a quintet state have relative energies at least 0.6 eV higher than the triplet state. The total energies of quartet states for $N = 5, 7$, and 9 are about 0.09, 0.2, and 0.04 eV higher than the doublet states. These clusters have about $2 \mu_B$ on the doped Co atom, which is located on the surface of the cluster. The result for Ag_5Co^- agrees with the previous theoretical calculations by Hou *et al.*, where the most stable 2D isomer is reported to be a doublet state with a magnetic moment of $1.99 \mu_B$ on Co,^[101] although the geometric structure shown in Fig. 5.1 is different from that in the previous study due to different functional and basis sets. On the other hand, the geometric structures for $N = 6-8$ contradict a previous report^[47] with a Co atom fully encapsulated by Ag atoms; the present calculation did not find encapsulated structures even among metastable structural isomers.

5.2.2. Electronic structures of Ag_NCo^- for $N = 6$ and 7

The electronic energy levels and the contours of corresponding molecular orbitals of Ag_6Co^- are shown in Fig. 5.2. The DOS shows that the energy levels of Co 3d orbital are separated from those of Ag sp and Co sp orbitals. The contours of its molecular orbitals indicate that the Co 3d orbital is localized on the Co atom.

Figure 5.3 shows the results of DFT calculations for Ag_7Co^- . The electronic structure and the contours of corresponding molecular orbitals reveal that Co 3d orbital is localized on the Co atom, the energy levels of which are separated from sp orbitals of Ag and Co.

5.3. Discussion

5.3.1. Localization of 3d electrons

In the reaction measurement for Ag_NCo^- , the dissociation products were mainly observed in TOF spectra as shown in Fig. 3.8, and accordingly these clusters exhibited high reactivity as shown in Fig. 4.1(g). The results suggested that Co 3d electrons may be localized on the Co atom, which may be located on the surface of the cluster. The speculation is supported by DFT calculations. These small sized Ag_NCo^- showed the exohedral geometry with a surface Co atom as shown in Fig. 5.1. The electronic structure for Ag_NCo^- ($N = 6, 7$, and 8) revealed that Co 3d orbitals are separated from sp orbitals of Ag and Co. The 3d orbitals are localized on the Co atom by analysis of the contours of molecular orbitals. Therefore, it is suggested that 3d electrons are localized on the Co atom, resulting in the local magnetic moment as large as $2 \mu_B$.

5.3.2. Revisit to photoelectron spectra previously reported

The discussion in Chapters 3 and 4 suggests that Ag_8Co^- should possess an open electronic shell. As this finding contradicts the previous report based on PES^[47], the author examines if the reported PES are reproduced as well by the present analysis. Simulation of PES was performed for $N = 6-8$ by the procedure described in Chapter 2.

The computational results are shown in Fig. 5.4 along with experimental spectra. The PES calculated for the triplet Ag_8Co^- is shown in Fig. 5.4(e), which exhibits two major peaks at 2.3 and 3.2 eV labeled as D' and E', respectively. This simulated PES explains the experimental one displayed in Fig. 5.4(f) very well in that the two peaks observed at 2.4 and 3.2 eV labeled as D and E, respectively, are indeed reproduced. Therefore, the present interpretation of Ag_8Co^- is consistent both with the previous PES experiment and with the present reactivity measurement as discussed in Chapter 4. Similarly, the experimental spectra of Ag_6Co^- (Fig. 5.4b) and Ag_7Co^- (Fig. 5.4d) are also reproduced well by the present analysis as shown in Figs. 5.4(a) and 5.4(c), respectively, although the geometric structures are different from those reported previously. These agreements with the PES experiment rationalize the reliability of the present analysis on the geometric and electronic structures of Ag_NCo^- clusters.

5.4. Summary

The author revisited electronic and geometric structures of Ag_NCo^- by reaction experiment with oxygen reported in Chapter 4 and DFT calculations. Ag_NCo^- for $N = 4-9$ exhibited reactivity higher than that of Ag_8^- , suggesting that the Co atom is an active site as discussed in Chapter 4. The speculation is supported by DFT calculations, which revealed that 3d electrons are localized on the Co atom, which is located on the surface of the cluster. The present reactivity measurement raised a question, in particular, about a closed electronic shell of Ag_8Co^- , an 18-e cluster, reported previously on the basis of PES experiment. The updated DFT calculation solved this contradiction, which explains both the reactivity and the PES spectra consistently. The present study thus provides a revised understanding of Ag_8Co^- ; s-d interaction is essentially weak such that Co 3d electrons are localized, resulting in an open-shell triplet state.

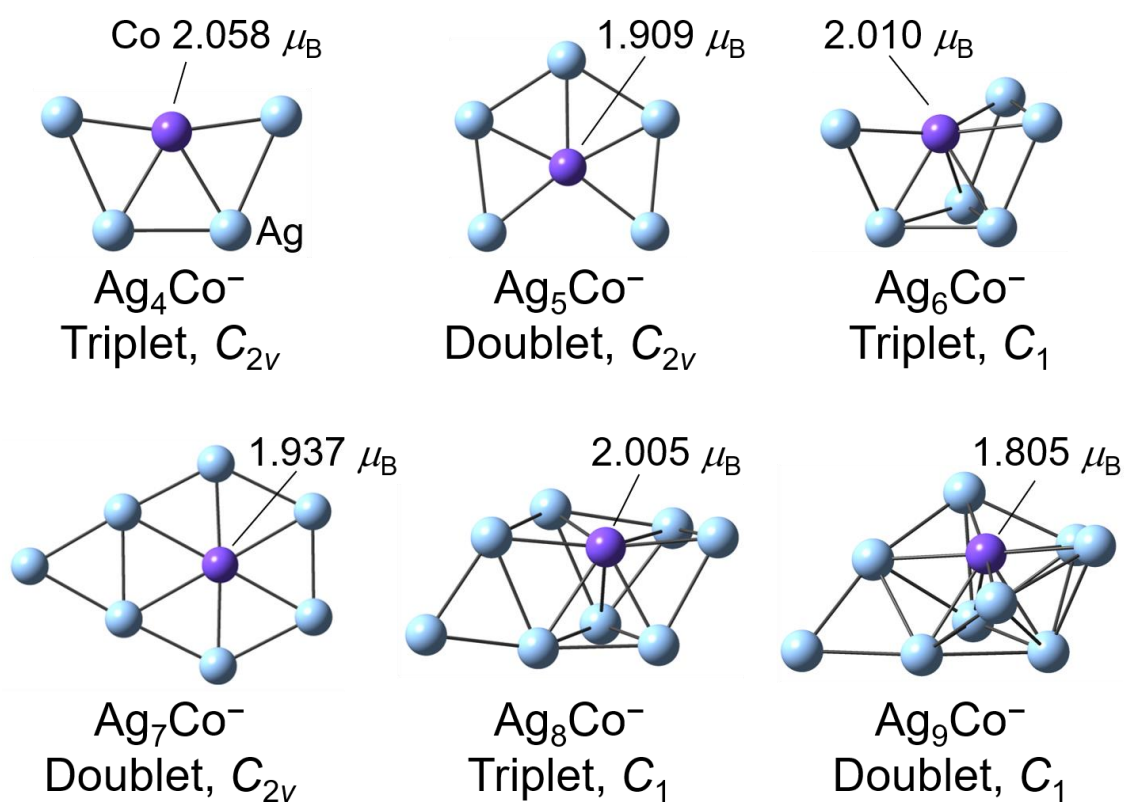


Figure 5.1. The most stable geometric structures of Ag_NCo^- ($N = 4-9$) optimized by DFT calculation. Spin multiplicity, symmetry, and the local magnetic moment on the Co atom are denoted.

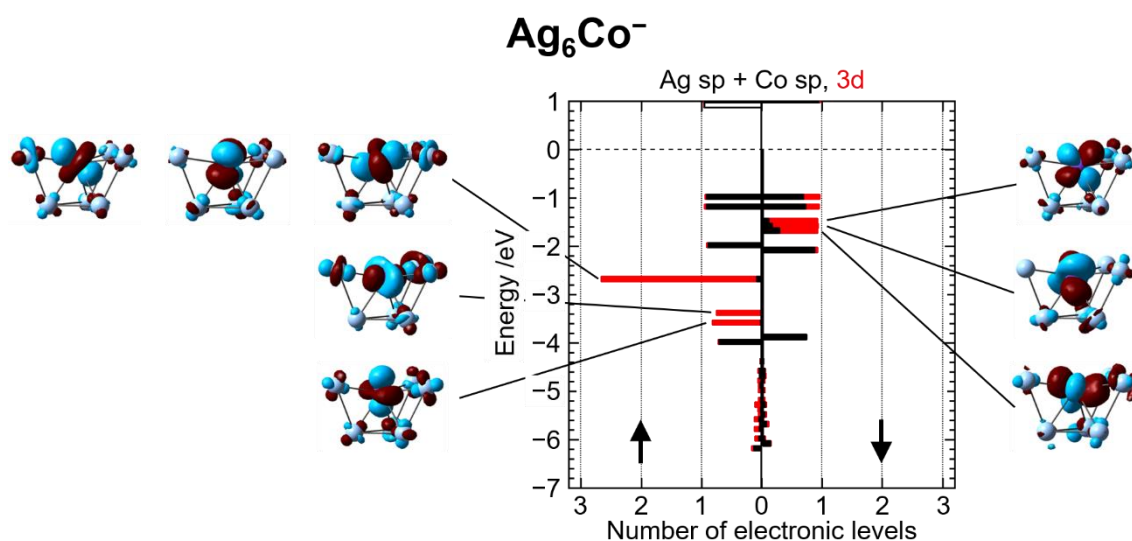


Figure 5.2. The electronic structure and isosurfaces of molecular-orbital wave functions (isovalue: 0.03) of Ag_6Co^- . The electronic structure is depicted by density-of-states (DOS) diagrams for majority and minority spins. Bars in the diagrams show the DOS of sp and 3d orbitals by black and red, respectively. The number of electronic levels is shown by histograms with 0.1-eV energy windows. The dashed line at 0 eV represents the chemical potential, below which the levels are occupied.

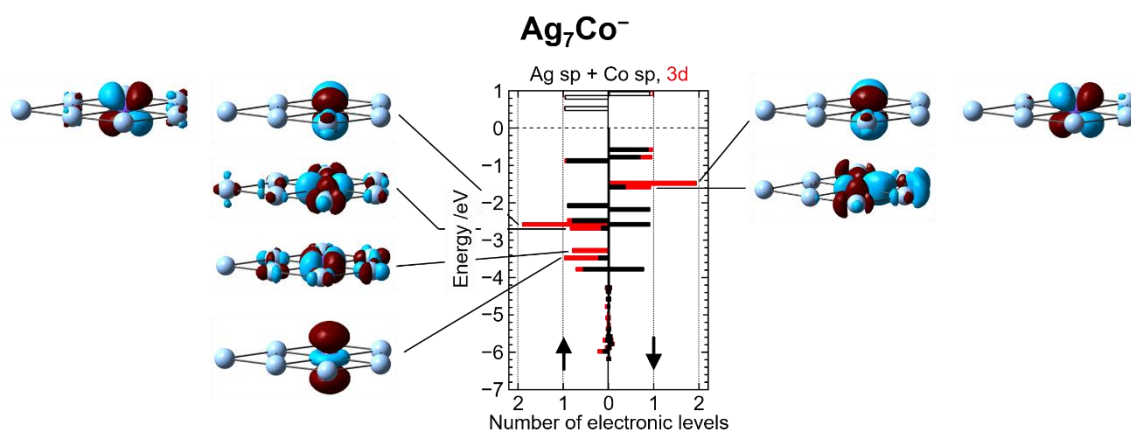


Figure 5.3. The electronic structure and isosurfaces of molecular-orbital wave functions (isovalue: 0.03) of Ag_7Co^- . The electronic structure is depicted by density-of-states (DOS) diagrams for majority and minority spins. Bars in the diagrams show the DOS of sp and 3d orbitals by black and red, respectively. The number of electronic levels is shown by histograms with 0.1-eV energy windows. The dashed line at 0 eV represents the chemical potential, below which the levels are occupied.

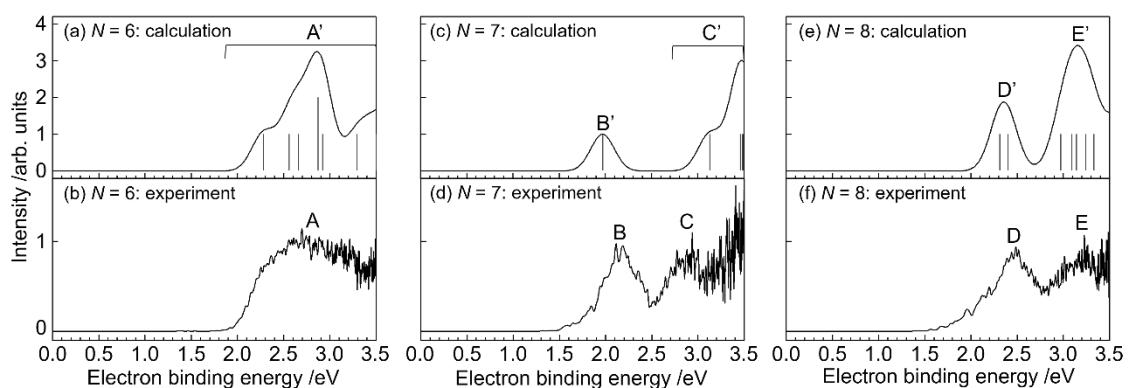


Figure 5.4. Photoelectron spectra of Ag_NCo^- ($N = 6-8$) obtained by the present DFT calculations (a, c and e) and by the previous experiment (b, d and f)^[47]. The bars in (a), (c) and (e) for $N = 6, 7$ and 8 , respectively, indicate electron binding energies (EBEs) calculated for their optimized structures; the solid curves show simulated spectra obtained by convolution of each EBE with a Gaussian profile with a 0.3-eV width in full width of half maximum.

Chapter 6. Photoelectron Velocity Map Imaging

6.1. Introduction

Under the spherical jellium model^[1], it is well known for metal clusters that valence electrons occupy discrete energy levels, which are described by 1S, 1P, 1D, ... superatomic orbitals. Knight and co-workers reported mass spectra of Na_N , where Na_N with specific sizes show rich abundance due to closed electronic shells.^[3] Sun and co-workers performed theoretical calculations for Na_{20} and revealed that 20 valence electrons in Na_{20} occupy 1S, 1P, 1D, and 2S orbitals to show electronic shell closure.^[13]

Photoelectron imaging (PEI)^[102] allows for simultaneous measurements of photoelectron kinetic-energy and angular distributions, providing a powerful means for exploring the superatomic orbitals experimentally. In fact, the angular momentum characters of the superatomic orbitals have recently been investigated by PEI for Na_N^- .^[103] Na_{40}^- occupy 1S, 1P, 1D, 2S, 1F, 2P, and 1G orbitals with 41 valence electrons, and the uppermost 1F, 2P, and 1G shells were clearly identified in the PES.^[103] They further reported significantly different angular distributions for the corresponding photoelectrons: essentially isotropic distribution is observed for electrons detached from the 1G shell, whereas it is parallel and perpendicular with respect to the laser polarization direction for 2P and 1F electrons, respectively.

In Chapter 4, the reactivity measurement combined with DFT calculations revealed that $\text{Ag}_{14}\text{Sc}^-$, $\text{Ag}_{13}\text{Ti}^-$, and Ag_{12}V^- form closed electronic shell structures with delocalized 3d electrons. The contour of molecular orbitals indeed illustrated 1S, 1P, and 1D superatomic orbitals. Using the PEI technique, it is possible to examine the angular momentum character as well as the quantized energy levels. In this Chapter, the author performs PEI of 18-e clusters for Ag_MM^- ($M = \text{Sc}, \text{Ti}, \text{and V}$) to further explore their electronic structures, using a newly developed photoelectron imaging (PEI) apparatus. In addition to the 18-e clusters, the author also investigates the electronic and geometric structures of 17-e and 19-e clusters to explore the origin of high stability of the

18-e clusters. To our knowledge, this is the first PEI studies for Ag_NM^- .

6.2. The analysis of experimental data

The experimental procedures for obtaining a 2D projection of photoelectrons detached from a quasi-continuous beam of Ag_NM^- have been described in detail in Chapter 2. The 2D projection thus obtained is analyzed to reconstruct the original 3D distribution using a polar-onion peeling (POP) algorithm developed by Verlet and co-workers.^[104] The algorithm uses a polar coordinate system as shown in Fig. 6.1 to calculate intensities at the azimuthal angle $\phi \sim 0$ in the 3D distributions, namely a 2D slice image. Briefly, the author set the maximum radial distance, r_{max} , in an obvious image, which corresponds to the outermost ring radius in the 2D projection. The 2D projection at $R = r_{\text{max}}$ is fitted by a well-known formula, $I(\theta) = N(r) \sum_n \beta_n(r) P_n[\cos(\theta)]$, where $P_n[\cos(\theta)]$ is the n -th order Legendre polynomial, r is the radial distance, and θ is the polar angle in the 3D distribution. The fit provides an intensity factor, $N(r)$, and the anisotropy parameters, $\beta_n(r)$. In our experiments we use linearly polarized light for photodetachment, where single-photon process is predominant. Thus, we consider only even terms of $\beta_n(r)$ and $P_n[\cos(\theta)]$, and the expansion is truncated at $n = 4$. Using $N(r)$ and $\beta_n(r)$, the intensities of the 3D distribution at $r = r_{\text{max}}$ can be calculated for all θ and ϕ , which is further converted into a 2D projection. After that, the calculated 2D distribution is subtracted from the measured 2D projection, yielding a modified 2D projection image is obtained for $r < r_{\text{max}}$. The process is repeated as a function of r at an interval of dr until $r = 0$ is reached. A 2D slice image of the original 3D distribution is obtained by coordinate transformation from the polar to cartesian pixels. To obtain a photoelectron spectrum from the 2D slice image, the intensities were multiplied by $\sqrt{r} \sin \theta$, which is different from $r \sin \theta$ usually employed to account for ϕ -dependence of the 3D distribution.^[104] Further integration of the weighted intensities over θ at each r yielded the radial distribution. It can be converted to a photoelectron spectrum via Jacobian transformation, $1/r$. The Photoelectron kinetic energy is calibrated with the

vertical electron detachment energy (VDE) for Ag_{14}^- .^[43]

6.3. Results

6.3.1. Sc-doped silver clusters

The 2D projections of photoelectrons detached from Ag_NSc^- for $N = 13, 14$, and 15 are shown in Figs. 6.2(a), 6.2(c) and 6.2(e), respectively. A laser-off background image has already been subtracted from each image. As shown in Fig. 6.2(a), the photoelectron image of $\text{Ag}_{13}\text{Sc}^-$ (17-e) is almost isotropic, and the intensity is the strongest at the center and becomes weaker away from the center. While the intensity of the $\text{Ag}_{14}\text{Sc}^-$ (18-e) image is also the strongest at the center, as seen in Fig. 6.2(c), photoelectrons detached from $\text{Ag}_{14}\text{Sc}^-$ were detected in an area narrower than those from $\text{Ag}_{13}\text{Sc}^-$. On the other hand, it is clear from Figs. 6.2(a), 6.2(c), and 6.2(e) that the photoelectron image for $\text{Ag}_{15}\text{Sc}^-$ (19-e) is quite different from that observed for the other two clusters. First, the area of the signal distribution for $\text{Ag}_{15}\text{Sc}^-$ is much larger than that for $\text{Ag}_{13}\text{Sc}^-$ and $\text{Ag}_{14}\text{Sc}^-$. Second, the $\text{Ag}_{15}\text{Sc}^-$ (19-e) image exhibits anisotropy along the laser polarization vector, ϵ . To visualize the photoelectron anisotropy more clearly, 2D slice images of the original 3D distributions, which are calculated by the procedure described above, are presented in Figs. 6.2(b), 6.2(d), and 6.2(f), respectively, for $\text{Ag}_{13}\text{Sc}^-$, $\text{Ag}_{14}\text{Sc}^-$, and $\text{Ag}_{15}\text{Sc}^-$. It is thus clear that the photoelectrons detached from $\text{Ag}_{15}\text{Sc}^-$ exhibit strong anisotropy with more intensity parallel to ϵ , as seen in Fig. 6.2(f).

DFT calculations of $\text{Ag}_{13}\text{Sc}^-$ and $\text{Ag}_{15}\text{Sc}^-$ were also performed to characterize their electronic and geometric structures. Figure 6.3 shows the optimized geometric and electronic structures of $\text{Ag}_{13}\text{Sc}^-$. The most stable isomer has an endohedral geometry (C_1) with doublet spin multiplicity, which is energetically lower than the most stable quartet state by 1.2 eV. As seen from the calculated electronic structure, the energy levels of the Sc 3d electrons are close to those of Ag sp and Sc sp electrons, and the contours of molecular orbitals illustrate 1S, 1P, and 1D orbitals. Theoretical results obtained for $\text{Ag}_{15}\text{Sc}^-$ are shown in Fig. 6.4. Geometric optimization reveals that the

most stable isomer has also an endohedral geometry (C_1) with doublet spin multiplicity, which is energetically lower than the most stable quartet state by 1.5 eV. As also seen for $\text{Ag}_{13}\text{Sc}^-$, Sc 3d orbital overlaps with Ag sp and Sc sp orbitals in $\text{Ag}_{15}\text{Sc}^-$, which results in formation of 1S, 1P, 1D, and 2S superatomic orbitals.

Figures 6.5(a), 6.5(c), and 6.5(e) represent PES for $\text{Ag}_{13}\text{Sc}^-$, $\text{Ag}_{14}\text{Sc}^-$, and $\text{Ag}_{15}\text{Sc}^-$, respectively. As shown in Figs. 6.5(a) and 6.5(c), the PES for $N = 13$ and 14 are almost the same: the spectral intensities are concentrated at EBEs around 3 eV, and each spectrum exhibits a tail towards lower EBEs. However, as clearly shown in Fig. 6.5(e), the PES dramatically changes when the clusters grow up to $\text{Ag}_{15}\text{Sc}^-$: it exhibits an intense peak around 1.90 eV. This value corresponds to VDE for this cluster anion, which is much smaller than 2.96 and 2.99 eV obtained for $\text{Ag}_{13}\text{Sc}^-$ and $\text{Ag}_{14}\text{Sc}^-$, respectively.

Figures 6.5(b), 6.5(d), and 6.5(f) show simulated PES for the most stable structures, which is obtained by the procedure already described in the computational method in Chapter 2. EBEs are shown by sticks, while the simulated spectra are obtained by convolution of each EBE with a Gaussian profile with 0.3-eV full-width at half-maximum (FWHM). As shown in Figs. 6.5(b) and 6.5(d), the simulated spectrum for $\text{Ag}_{13}\text{Sc}^-$ exhibits one major peak at around 2.7 eV, and that for $\text{Ag}_{14}\text{Sc}^-$ exhibits only a single peak at 2.8 eV. It should be noted for $\text{Ag}_{13}\text{Sc}^-$ that a small hump is predicted at 2.43 eV, which corresponds to the calculated VDE of the cluster. On the other hand, as shown in Fig. 6.5(f), the simulated PES for $N = 15$ shows two major peaks. The first peak appears at 1.79 eV, which corresponds to the calculated VDE and is significantly lower than those calculated for $\text{Ag}_{13}\text{Sc}^-$ and $\text{Ag}_{14}\text{Sc}^-$. Table 6.1 summarizes the experimental and calculated VDEs for these clusters.

6.3.2. Ti-doped silver clusters

The 2D projections of photoelectrons detached from Ag_NTi^- for $N = 12, 13$, and 14 are shown in Figs. 6.6(a), 6.6(c), and 6.6(e), respectively. A laser-off background

image has already been subtracted from each image. As seen from Figs. 6.6(a) and 6.6(c), the images for $\text{Ag}_{12}\text{Ti}^-$ (17-e) and $\text{Ag}_{13}\text{Ti}^-$ (18-e) are almost isotropic, and the photoelectrons detached from $\text{Ag}_{13}\text{Ti}^-$ were detected in an area smaller than those from $\text{Ag}_{12}\text{Ti}^-$. On the other hand, it is clear from Figs. 6.6(a), 6.6(c), and 6.6(e) that the photoelectron image for $\text{Ag}_{14}\text{Ti}^-$ (19-e) is notably different from that for the other two clusters. First, the area of the signal distribution for $\text{Ag}_{14}\text{Ti}^-$ is much larger than that for $\text{Ag}_{12}\text{Ti}^-$ and $\text{Ag}_{13}\text{Ti}^-$. Second, the $\text{Ag}_{14}\text{Ti}^-$ (19-e) image exhibits anisotropy along the laser polarization vector, ε . To visualize the photoelectron anisotropy more clearly, 2D slice images for $N = 12, 13$, and 14 are shown in Figs. 6.6(b), 6.6(d), and 6.6(f), respectively. It is now obvious from Fig. 6.6(f) that the photoelectrons detached from $\text{Ag}_{14}\text{Ti}^-$ exhibit strong anisotropy with more intensity parallel to ε . Thus, these features observed for Ag_NTi^- closely resemble those observed for Ag_NSc^- .

DFT calculations were performed to characterize electronic and geometric structures of $\text{Ag}_{12}\text{Ti}^-$ and $\text{Ag}_{14}\text{Ti}^-$. Figure 6.7 shows the optimized geometric and electronic structures of $\text{Ag}_{12}\text{Ti}^-$. The most stable isomer has an endohedral geometry with D_{3d} symmetry, which is slightly distorted from the optimized geometry for Ag_{12}V^- that has I_h symmetry (see Fig. 3.12). While the most stable structure of $\text{Ag}_{12}\text{Ti}^-$ has doublet spin multiplicity, the most stable quartet state of $\text{Ag}_{12}\text{Ti}^-$ lies 1.0 eV higher than the doublet state. The local magnetic moment on the encapsulated Ti atom is estimated to be $0.94 \mu_B$. As clearly seen in Fig. 6.7, the DFT calculations reveal that energy levels of the Ti 3d electrons overlap with those of Ag sp and Ti sp electrons to form 1S, 1P, and 1D orbitals. Figure 6.8 shows the geometric and electronic structures of $\text{Ag}_{14}\text{Ti}^-$. The cluster has an endohedral geometry (C_1) with doublet spin multiplicity, and thus the situation is different from that of $\text{Ag}_{14}\text{Sc}^-$ shown in Fig. 3.12. It is noted that the most stable quartet state lies 0.76 eV higher than the doublet state. The local magnetic moment on the Ti atom is calculated to be $1.15 \mu_B$. While superatomic character is also seen from the contour of molecular orbitals shown in Fig. 6.8, close inspection reveals that the electron cloud of HOMO is mostly localized on the outermost Ag and the

encapsulated Ti atom.

Figures 6.9(a), 6.9(c), and 6.9(e) represent PES for $\text{Ag}_{12}\text{Ti}^-$, $\text{Ag}_{13}\text{Ti}^-$, and $\text{Ag}_{14}\text{Ti}^-$, respectively. As shown in Figs. 6.9(a) and 6.9(c), the PES for $N = 12$ and 13 are almost the same: the spectral intensities are concentrated on EBEs around 2.9 eV and each spectrum exhibits a tail towards lower EBEs. From the figures, the VDEs for $\text{Ag}_{12}\text{Ti}^-$ and $\text{Ag}_{13}\text{Ti}^-$ are estimated to be 2.89 and 3.00 eV, respectively. It should be noted that the VDE of $\text{Ag}_{13}\text{Ti}^-$, a 18-e cluster, is slightly higher than that of $\text{Ag}_{12}\text{Ti}^-$. As clearly seen from Fig. 6.9(e), the PES drastically changes when the clusters grow up to $N = 14$. The VDE of $\text{Ag}_{14}\text{Ti}^-$ is evaluated to be 1.8 eV from an intense peak in the PES, which is much smaller than those obtained for $\text{Ag}_{12}\text{Ti}^-$ and $\text{Ag}_{13}\text{Ti}^-$. Again, this trend is exactly similar to that observed for Ag_NSc^- .

Fig. 6.9(b), 6.9(d), and 6.9(f) show simulated PES for the most stable structures for $\text{Ag}_{12}\text{Ti}^-$, $\text{Ag}_{13}\text{Ti}^-$, and $\text{Ag}_{14}\text{Ti}^-$, respectively. EBEs are shown by sticks, while the simulated spectra are obtained by convolution of each EBE with a Gaussian profile with FWHM of 0.3-eV. While the simulation PES for $\text{Ag}_{12}\text{Ti}^-$ (17-e) and $\text{Ag}_{13}\text{Ti}^-$ (18-e) both exhibit a single peak in 2.7–2.8 eV, the simulated PES for $\text{Ag}_{14}\text{Ti}^-$ (19-e) shows two peaks at 2.3 and 2.9 eV, as shown in the figures. The calculated VDEs are summarized in Table 6.2 along with the experimental values.

6.3.3. V-doped silver clusters

The 2D projections of photoelectrons detached from Ag_NV^- for $N = 11, 12$, and 13 are shown in Figs. 6.10(a), 6.10(c), and 6.10(e), respectively. A laser-off background image has already been subtracted from each image. Close inspection of the photoelectron image for Ag_{11}V^- (17-e) shown in Fig. 6.10(a) reveals two nearly isotropic components with different radii. The image of Ag_{12}V^- (18-e) consists of a single component, and the distribution is almost isotropic. As shown in Fig. 6.10(e), photoelectrons from Ag_{13}V^- (19-e) spread over a significantly larger area than those from other sizes. Calculated 2D slice images are presented in Figs. 6.10(b), 6.10(d), and

6.10(f). It is obvious that the features observed for Ag_NV^- are different from those observed for Ag_NSc^- and Ag_NTi^- .

DFT calculations were performed to characterize electronic and geometric structures of Ag_{11}V^- and Ag_{13}V^- . Figure 6.11 shows the optimized geometric and electronic structures of Ag_{11}V^- , which reveals that encapsulation of the dopant atom is incomplete. The spin multiplicity is doublet, which is common to the other 17-e clusters of $\text{Ag}_{13}\text{Sc}^-$ and $\text{Ag}_{12}\text{Ti}^-$. A quartet state is higher than the doublet state by 0.42 eV. The local magnetic moment on the V atom is estimated to be $2.8 \mu_B$, whereas Ag atoms have $-1.8 \mu_B$ in total, resulting in the doublet state. As seen in Fig. 6.11, while the energy levels of V 3d electrons overlap with those of Ag sp and V sp electrons, the contours of the molecular orbitals reveal that the top nine orbitals mainly consist of V 3d orbitals. Figure 6.12 shows the geometric and electronic structures of Ag_{13}V^- , which exhibit some similarity to those found for Ag_{11}V^- . The theoretical results shown in Fig. 6.12 are of a metastable isomer because a simulated PES based on the metastable structure better reproduces the experimental PES than that based on the most stable isomer, as discussed below. The metastable isomer lies higher than the most stable one by 0.68 eV and has an incomplete endohedral geometry with doublet spin multiplicity. As shown in Fig. 6.11, the 3d orbital of the V atom overlaps with sp orbitals of Ag and V, whereas the 3d orbitals may be localized on V atom, which is seen from the contour of HOMO.

Figures 6.13(a), 6.13(c), and 6.13(e) represent PESs for Ag_{11}V^- , Ag_{12}V^- , and Ag_{13}V^- . The PES for $N=11$ shows two features at 2.61 eV and at about 2.9 eV, and the first peak corresponds to VDE. The PES for $N=13$ also exhibits two peaks at 2.27 eV and at about 2.9 eV, whereas that for $N=12$ shows only one peak at 2.87 eV as VDE by a tentative assignment.

Figures 6.13(b), 6.13(d), and 6.13(f) show simulated PES for the optimized stable structures. EBEs are shown by sticks, while the simulated spectra are obtained by convolution of each EBE with a Gaussian profile with FWHM of 0.3-eV. The simulated PES for $N=11$ exhibits one major peak at 2.5 eV, where the VDE is calculated

to be 2.34 eV. For $N = 12$, an 18-e cluster, the spectrum shows one peak at 2.6 eV, and the calculated VDE is 2.55 eV, which is higher than that of Ag_{11}V^- with 17 valence electrons. On the other hand, the simulated spectrum for $N = 13$, a 19-e clusters, shows two major peaks, as shown in Fig. 6.13(f). The first peak emerges at 2.24 eV, as VDE, and the value is lower than those of the other sizes. The experimental and theoretical VDEs are summarized in Table 6.3.

6.4. Discussion

Here the author discusses the electronic structures of Sc-, Ti-, and V-doped silver cluster anions with 17, 18, and 19 valence electrons, focusing on localization/delocalization of 3d electrons of the transition metals.

6.4.1. Behavior of 3d electrons in Ag_NSc^-

The photoelectron image and spectrum for $\text{Ag}_{14}\text{Sc}^-$ reveals the largest EBE among 17-e, 18-e, and 19-e clusters, suggesting that the closed electronic shell is formed by 18 valence electrons. This is fully consistent with the conclusion drawn from the reactivity measurement combined with DFT calculations described in Chapter 4. The simulated spectrum for $\text{Ag}_{14}\text{Sc}^-$ (Fig. 6.5d) well reproduces the observed one (Fig. 6.5c), which verifies the validity of the calculated electronic structure presented in Fig. 4.2(a). Therefore, a 3d electron of Sc is indeed delocalized and contribute to the formation of 1S, 1P, and 1D superatomic orbitals, as clearly visualized in Fig. 4.2(b). This is the first photoelectron spectroscopic evidence for participation of a 3d electron of a foreign atom doped in a coinage metal cluster.

As shown in Figs. 6.2 and 6.5, the photoelectron image and spectrum for $\text{Ag}_{13}\text{Sc}^-$ (17-e) exhibit features similar to those observed for $\text{Ag}_{14}\text{Sc}^-$, suggesting that their electronic structures resemble each other. However, as shown in Fig. 6.3(b), $\text{Ag}_{13}\text{Sc}^-$ has a singly occupied molecular orbital (SOMO), from which the occupied electron can be detached upon the laser irradiation. While the calculated PES for $\text{Ag}_{13}\text{Sc}^-$ exhibits a

hump around 2.4 eV that corresponds to the photodetachment signal from the SOMO, such a hump is not clearly identified in the experimental spectrum owing to a broad component extending towards a lower EBE region. As presented in Chapter 4, the reactivity of $\text{Ag}_{13}\text{Sc}^-$ towards molecular oxygen is much higher than that of $\text{Ag}_{14}\text{Sc}^-$. Since the reaction may be triggered by electron transfer from the cluster anion to O_2 , the author conjectures that the SOMO electron of $\text{Ag}_{13}\text{Sc}^-$ with much lower binding energy than VDE of $\text{Ag}_{14}\text{Sc}^-$ (~ 3 eV) is responsible for the high reactivity. Agreement between the observed and simulated PES for $\text{Ag}_{13}\text{Sc}^-$ is reasonably well, which verifies that the 3d electron of Sc is also delocalized in the cluster.

As shown in subsection 6.3.1, the photoelectron image and spectrum for $\text{Ag}_{15}\text{Sc}^-$ (19-e) are significantly different from those observed for the other two sizes. Most strikingly, the 2D slice image shown in Fig. 6.2(f) exhibits strong anisotropy with more photoelectrons detected parallel to the laser polarization (ε). In an analogy to photodetachment of atomic anions, this behavior is typically observed for photodetachment of s-electrons, because the selection rule for the orbital angular momentum, $\Delta l = \pm 1$, predicts that only p-wave is allowed for a photoelectron partial wave.^[105] The calculated electronic structure shown in Fig. 6.4(a) reveals that the SOMO is indeed characterized as 2S superatomic orbital, from which the singly-occupying electron is ejected upon photodetachment to yield the large ring shown in Fig. 6.2(f). The present DFT calculation thus supports the above scenario regarding photoelectron angular distribution. The calculated VDE (1.79 eV) is in good agreement with the observed one (~ 1.9 eV), which further confirms the validity of the present calculation. Again, this is a clear evidence rationalizing that a 3d electron of Sc participates in electron counting to form superatomic orbitals of 1S, 1P, 1D, and 2S. The high reactivity of $\text{Ag}_{15}\text{Sc}^-$ toward O_2 is probably due to its considerably low VDE compared to that for the closed shell system, $\text{Ag}_{14}\text{Sc}^-$.

It is found that the Sc 3d electron is delocalized in all the clusters investigated here. As already described, the open-shell clusters, $\text{Ag}_{13}\text{Sc}^-$ (17-e) and $\text{Ag}_{15}\text{Sc}^-$ (19-e)

exhibit much higher reactivity toward O_2 than the 18-e closed-shell cluster of $Ag_{14}Sc^-$, suggesting that delocalization of a 3d electron is not a decisive factor on the reactivity toward O_2 . Very recently, reactivities of 17-e, 18-e, and 19-e silver clusters, *i.e.*, Ag_{16}^- , Ag_{17}^- , and Ag_{18}^- , toward O_2 were investigated by Luo and co-workers.^[106] They found that these silver cluster anions exhibit exceptionally low reactivity compared to the other cluster sizes. These results on Ag_{16}^- and Ag_{18}^- exemplify chemically stable clusters even when they are open-shell species. While reactivity toward small molecules is a good measure to explore closed-shell nature of metal clusters, further investigation is necessary to characterize and rationalize the electron-counting dependent reactivity of these clusters found in the present thesis.

6.4.2. Behavior of 3d electrons in Ag_NTi^-

The features of photoelectron images and spectrum for Ag_NTi^- are similar to those for Ag_NSc^- . The observed spectrum for $Ag_{13}Ti^-$ (18-e) shows the largest EBE among the three clusters, suggesting that a closed electronic shell by 18 valence electrons is formed in the cluster. This is consistent with the conclusion drawn from reactivity measurement combined with the DFT calculations described in Chapter 4. The simulated spectrum for $Ag_{13}Ti^-$ (Fig. 6.9d) well reproduces the observed one (Fig. 6.9c), which verifies the validity of the calculated electronic structure shown in Fig. 4.4(b). Therefore, it is concluded that 3d electrons of Ti are delocalized in $Ag_{13}Ti^-$.

As shown in Figs. 6.6 and 6.9, the observed spectrum for $Ag_{12}Ti^-$ (17-e) closely resembles that for $Ag_{13}Ti^-$, suggesting that their electronic structures are similar to each other. However, $Ag_{12}Ti^-$ has a SOMO, from which the occupied electron can be detached easier than that from fully occupied orbitals. The simulated spectrum for $Ag_{12}Ti^-$ based on the geometry shown in Fig. 6.6 reproduces the experimental one, which actually shows VDE lower than that of $Ag_{13}Ti^-$. The result also verifies the validity of the present DFT calculations. It is therefore concluded that Ti 3d electrons are delocalized also in the 17-e cluster.

The photoelectron image for $\text{Ag}_{14}\text{Ti}^-$ (19-e) shows noticeable anisotropy along the laser polarization direction, suggesting that the detached photoelectrons may originate from s-like orbital. The contour of SOMO (Fig. 6.8b) illustrates s-like orbital on the outermost Ag atom and 3d orbital on the Ti atom. It is thus speculated that the anisotropic feature in the photoelectron image is attributed to the SOMO. The cluster may form a closed electronic shell by a release of an unpaired electron in SOMO, yielding a low VDE value. This is well reproduced by the simulated PES shown in Fig. 6.9(f). Therefore, it is suggested that the Ti 3d electrons are partially delocalized in the $\text{Ag}_{14}\text{Ti}^-$. However, the calculated PES for the optimized geometry of $\text{Ag}_{14}\text{Ti}^-$ (Fig. 6.8) does not fully reproduce the experimental ones. Thus, further theoretical investigation is needed for $\text{Ag}_{14}\text{Ti}^-$.

In the case of Ti-doped systems, Ti 3d electrons may be delocalized in all the clusters investigated here, whereas the 17-e and 19-e clusters exhibited the reactivity higher than the 18-e cluster, as reported in Chapter 4. As discussed above for the Sc-doped clusters, these highly reactive clusters have an unpaired electron in HOMO (SOMO), and both of the VDEs are lower than that of $\text{Ag}_{13}\text{Ti}^-$. Therefore, the open electronic shell structure is partly responsible for the higher reactivity towards molecular oxygen that acts as an electron acceptor.

6.4.3. Behavior of 3d electrons in Ag_NV^-

As shown in Figs. 6.13(c) and 6.13(d), the observed spectrum of Ag_{12}V^- exhibited one major peak at 2.6 eV, which is reproduced by the simulated spectrum shown in Fig. 6.13(d). The VDE is the largest among the 17-e, 18-e, and 19-e clusters, suggesting that the closed electronic shell is formed in Ag_{12}V^- . As shown in Fig. 4.6, this is supported by the DFT calculations predicting that the V 3d electrons are delocalized in the cluster.

It is noted that the photoelectron image and spectrum observed for Ag_{12}V^- , an 18-e cluster, exhibit similar features to those observed for the other 18-e clusters, $\text{Ag}_{14}\text{Sc}^-$

and $\text{Ag}_{13}\text{Ti}^-$. On the other hand, the photoelectron image and spectrum observed for Ag_{11}V^- (17-e) are notably different from those observed for the other 17-e clusters, $\text{Ag}_{13}\text{Sc}^-$ and $\text{Ag}_{12}\text{Ti}^-$: the Ag_{11}V^- spectrum clearly exhibits a doublet peak in 2.5 – 3.0 eV with a small shoulder in a lower EBE region. Although the simulated PES does not fully reproduce the experimental one, the situation for Ag_{11}V^- is clearly different from that for the other 17-e clusters, implying that the V 3d electrons may be localized to result in the $2.8 \mu_B$ on V atom. This suggests that s–d interaction should be weak in Ag_{11}V^- .

Ag_{13}V^- also shows a trend different from the other 19-e clusters, $\text{Ag}_{15}\text{Sc}^-$ and $\text{Ag}_{14}\text{Ti}^-$, in the observed photoelectron image and spectrum. The photoelectron image illustrates an isotropic feature similar to the other V-doped clusters, suggesting that the SOMO may not be spherical. The DFT calculations reveal that the HOMO has an anisotropic shape, which is consistent with the speculation. In addition, the simulated spectrum reproduces the two peaks that are observed in the experimental result, as shown in Figs. 6.13(e) and (f), which confirms the DFT calculations illustrating that 3d electrons are localized on the V atom with a local magnetic moment of $2.6 \mu_B$. Therefore, it is concluded that the V 3d electrons are localized in Ag_{13}V^- as well as in Ag_{11}V^- .

Referring to fundamental principles in molecular orbital theory, the strength of the s–d interaction should be related to orbital energy difference between the V 3d orbital and Ag 5s orbital. The 3d orbital energies of Sc, Ti, and V atom have been reported to 8.01, 9.94, and ~ 12 eV, respectively.^[107,108] The 5s orbital energy of Ag atom is evaluated to be 7.58 eV, which is equal to ionization energy reported in the NIST database. This suggests that the s–d interaction in V-doped clusters should be weaker than that in Sc- and Ti-doped clusters, yielding incomplete hybridization of the V 3d and Ag 5s electrons in Ag_{11}V^- and Ag_{13}V^- . In this sense, why the V 3d electrons are delocalized only in Ag_{12}V^- (18-e) is unclear at present. The author speculates that a highly symmetric (I_h), endohedral geometry of Ag_{12}V^- is responsible for this exception.

The size-dependent reactivity showed that the 17-e and 19-e clusters exhibit reactivity higher than the 18-e cluster as shown in Fig. 4.1(c). As mentioned above, V

3d electrons may be localized on the V atom in these highly reactive clusters. In common with the other 17-e and 19-e clusters, these V-doped clusters have an unpaired electron in the HOMO, which is higher in energy than that of the 18-e cluster as evidenced by lower VDEs. Therefore, these electronic structures with high-lying HOMOs may lead to the high reactivity because oxygen molecules behave as an electron acceptor.

6.5. Summary

In this chapter, the author investigated the electronic structures of Ag_NM^- ($\text{M} = \text{Sc}, \text{Ti}, \text{and V}$) with 17, 18, and 19 valence electrons by the newly developed PEI apparatus to explore localization/delocalization of 3d electrons.

For Sc-doped clusters, the photoelectron spectrum observed for $\text{Ag}_{14}\text{Sc}^-$ (18-e) exhibited a much lower VDE than $\text{Ag}_{13}\text{Sc}^-$ and $\text{Ag}_{15}\text{Sc}^-$, indicating that the 18-e cluster forms a closed electronic-shell structure with a delocalized 3d electron. A similar photoelectron spectrum was observed for $\text{Ag}_{13}\text{Sc}^-$, a 17-e cluster, suggesting that their electronic structures resemble each other. The photoelectron image of $\text{Ag}_{15}\text{Sc}^-$ (19-e), which was found to be significantly different from those of $N = 13$ and 14, exhibited a strong anisotropy along the laser polarization direction, suggesting that the HOMO of $\text{Ag}_{15}\text{Sc}^-$ may be s-like orbital. All the experimental results are supported by the DFT calculations predicting a 3d electron of Sc atom is fully delocalized in all the clusters. It thus follows that the 3d electron is delocalized in the doped clusters regardless of the number of the valence electrons.

These experimental features revealed for Ag_NSc^- were found to be in common with Ag_NTi^- , which were also supported by the DFT calculations. However, while the 18-e cluster of Ag_{12}V^- was found to form a closed electronic shell with delocalized 3d electrons, the Ag_{11}V^- (17-e) and Ag_{13}V^- (19-e) clusters exhibited trends different from the corresponding Sc- and Ti-doped clusters with the same number of valence electrons. The DFT calculations for Ag_{11}V^- and Ag_{13}V^- revealed that the V 3d electrons in both clusters are localized on the dopant, resulting in a local magnetic moment on the V atom.

Therefore, it is concluded that the 3d electron(s) of Sc and Ti atoms may prefer to delocalize in the clusters, while those of a V atom tend to localize except for Ag_{12}V^- , where the stabilization energy upon electronic-shell closure might exceed the promotion energy for the 3d electrons to delocalize.

Table 6.1. Vertical detachment energies (VDEs) of $\text{Ag}_{13}\text{Sc}^-$, $\text{Ag}_{14}\text{Sc}^-$, and $\text{Ag}_{15}\text{Sc}^-$ obtained by experimental and theoretical PES.

Clusters	Experimental VDE /eV	Calculated VDE /eV
$\text{Ag}_{13}\text{Sc}^-$	2.96	2.43
$\text{Ag}_{14}\text{Sc}^-$	2.99	2.82
$\text{Ag}_{15}\text{Sc}^-$	1.90	1.79

Table 6.2. Vertical detachment energies (VDEs) of $\text{Ag}_{12}\text{Ti}^-$, $\text{Ag}_{13}\text{Ti}^-$, and $\text{Ag}_{14}\text{Ti}^-$ obtained by experimental and theoretical PES.

Clusters	Experimental VDE /eV	Calculated VDE /eV
$\text{Ag}_{12}\text{Ti}^-$	2.89	2.57
$\text{Ag}_{13}\text{Ti}^-$	3.00	2.72
$\text{Ag}_{14}\text{Ti}^-$	1.80	2.33

Table 6.3. Vertical detachment energies (VDEs) of Ag_{11}V^- , Ag_{12}V^- , and Ag_{13}V^- obtained by experimental and theoretical PES.

Clusters	Experimental VDE /eV	Calculated VDE /eV
Ag_{11}V^-	2.61	2.34
Ag_{12}V^-	2.87	2.55
Ag_{13}V^-	2.27	2.24

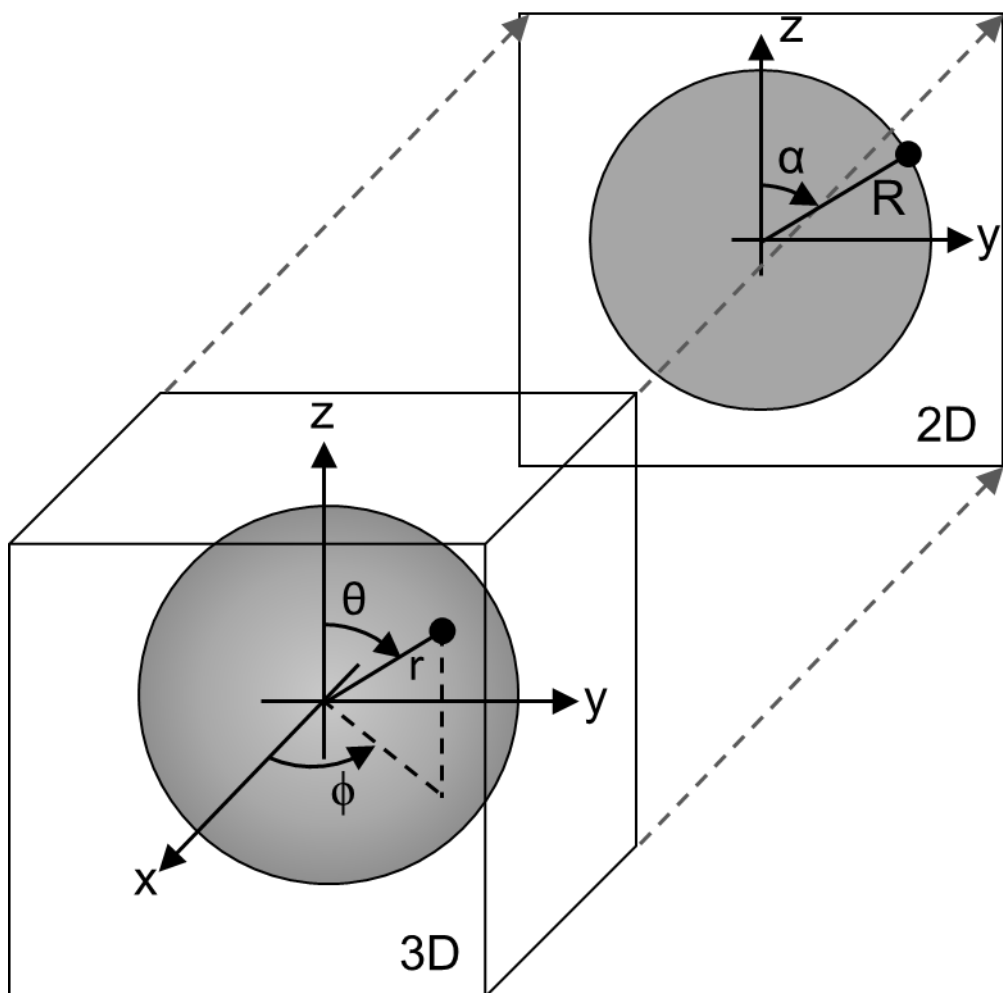


Figure 6.1. 3D distribution and 2D projection of photoelectrons ejected from cluster anions. The 3D distribution exhibits cylindrical symmetry with respect to laser polarization (z-axis).

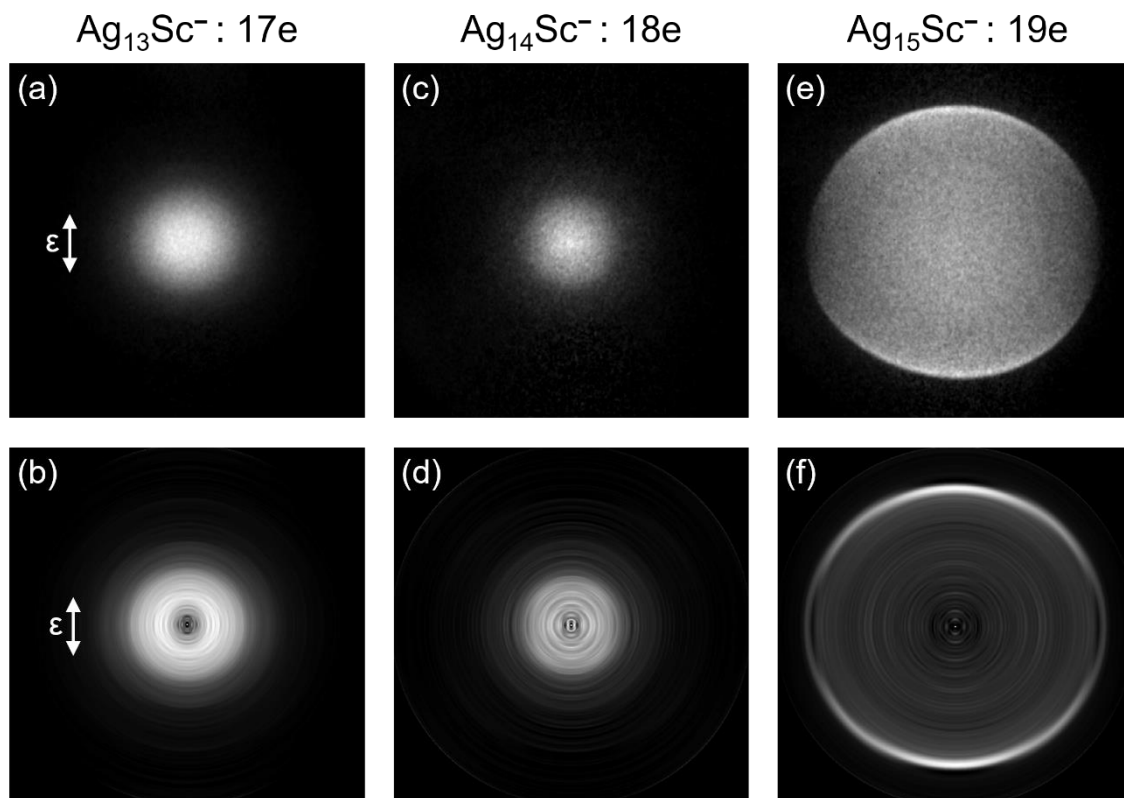


Figure 6.2. Photoelectron images (a, c, and e) and 2D slice images (b, d, and f) of Ag_NSc^- for $N=13, 14,$ and 15 . The images shown in the left side are for 17-e clusters; central panels for 18-e clusters; right panels for 19-e clusters. The direction of polarization is given in panels (a) and (b) by arrows.

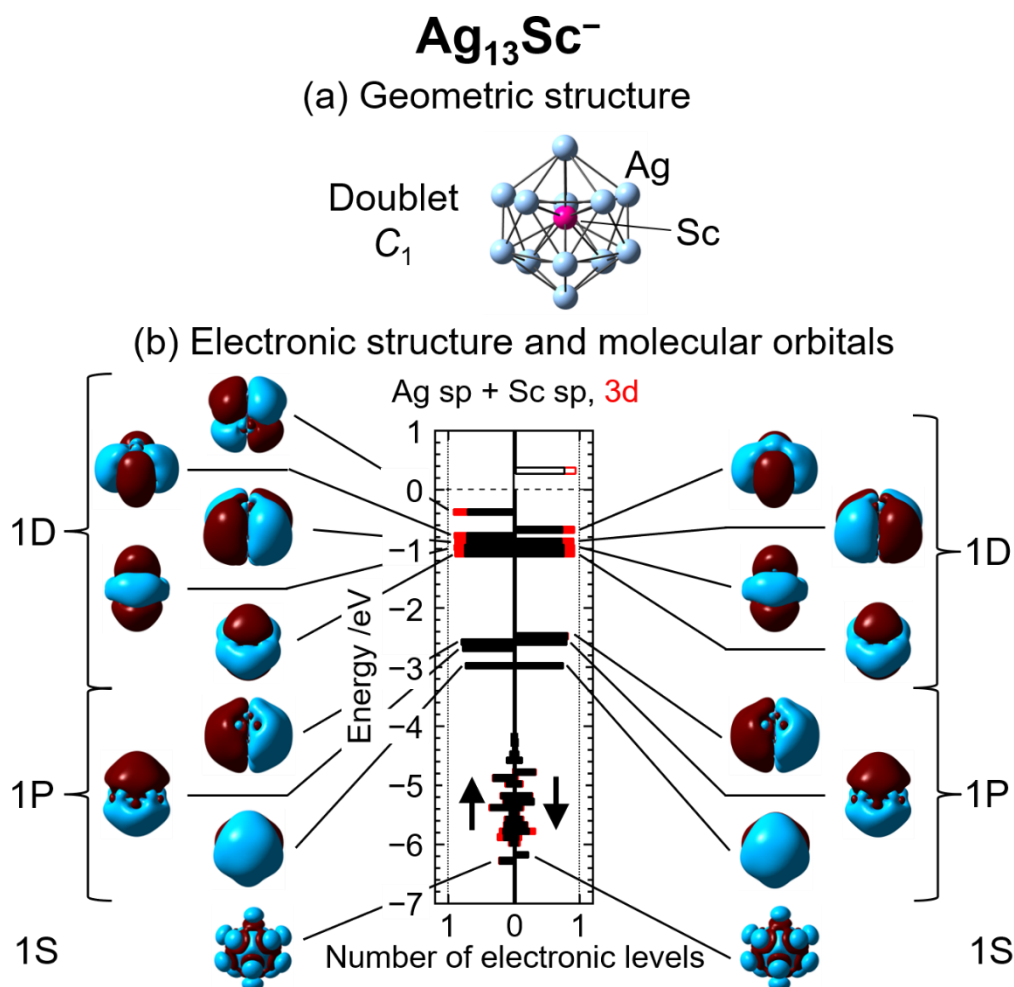


Figure 6.3. Results of DFT calculations on Ag₁₃Sc⁻. Panel (a) shows an optimized geometric structure along with its symmetry, spin multiplicity, and a local magnetic moment on the Sc atom. Panel (b) exhibits an electronic structure depicted by density-of-states (DOS) diagrams for majority and minority spins. Bars in black and red show DOSs of sp and 3d orbitals, respectively. The number of electronic levels is shown by histograms with 0.1-eV energy windows. The dashed line at 0 eV represents the chemical potential, below which the levels are occupied. The contours of the wave functions illustrate formation of 1S, 1P, and 1D orbitals with isovalue of 0.0035.

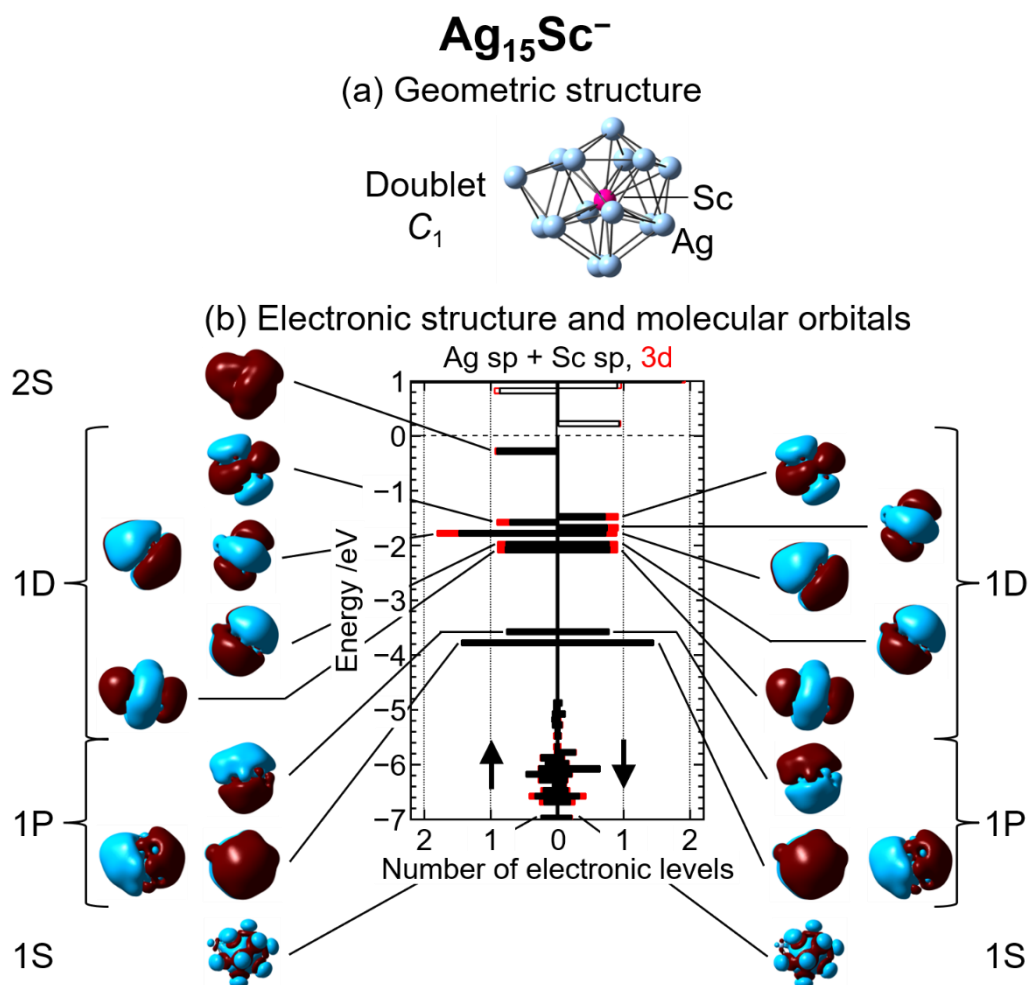


Figure 6.4. Results of DFT calculations on Ag₁₅Sc⁻. Panel (a) shows an optimized geometric structure along with its symmetry, spin multiplicity, and a local magnetic moment on the Sc atom. Panel (b) exhibits the electronic structure depicted by density-of-states (DOS) diagrams for majority and minority spins. Bars in black and red show DOSs of sp and 3d orbitals, respectively. The number of electronic levels is shown by histograms with 0.1-eV energy windows. The dashed line at 0 eV represents the chemical potential, below which the levels are occupied. The contours of the wave functions illustrate formation of 1S, 1P, 1D, and 2S orbitals with isovalue of 0.0035.

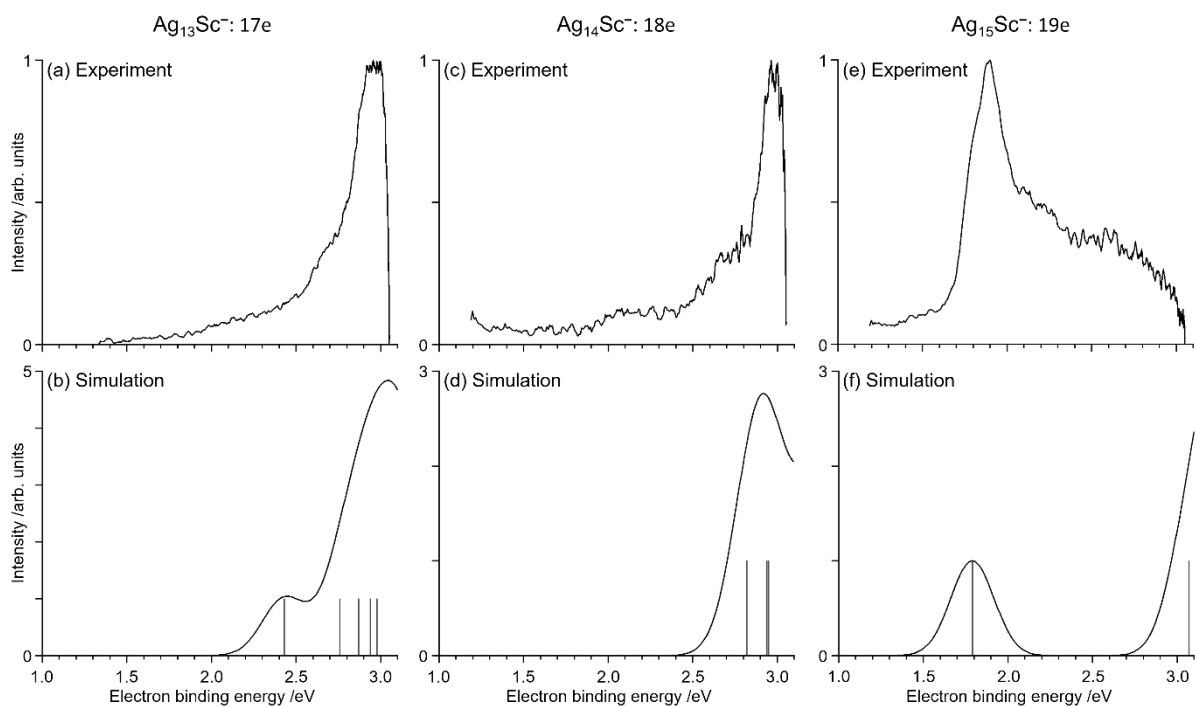


Figure 6.5. Photoelectron spectra of Ag_NSc^- for $N = 13, 14$, and 15 . Three pairs of spectra are shown in left, center, and right panels for $N = 13$ (17-e), 14 (18-e), and 15 (19-e), respectively. Panels (a), (c), and (e) show experimental spectra measured by PEI. Panels (b), (d), and (f) illustrate simulated spectra calculated by DFT and TDDFT.

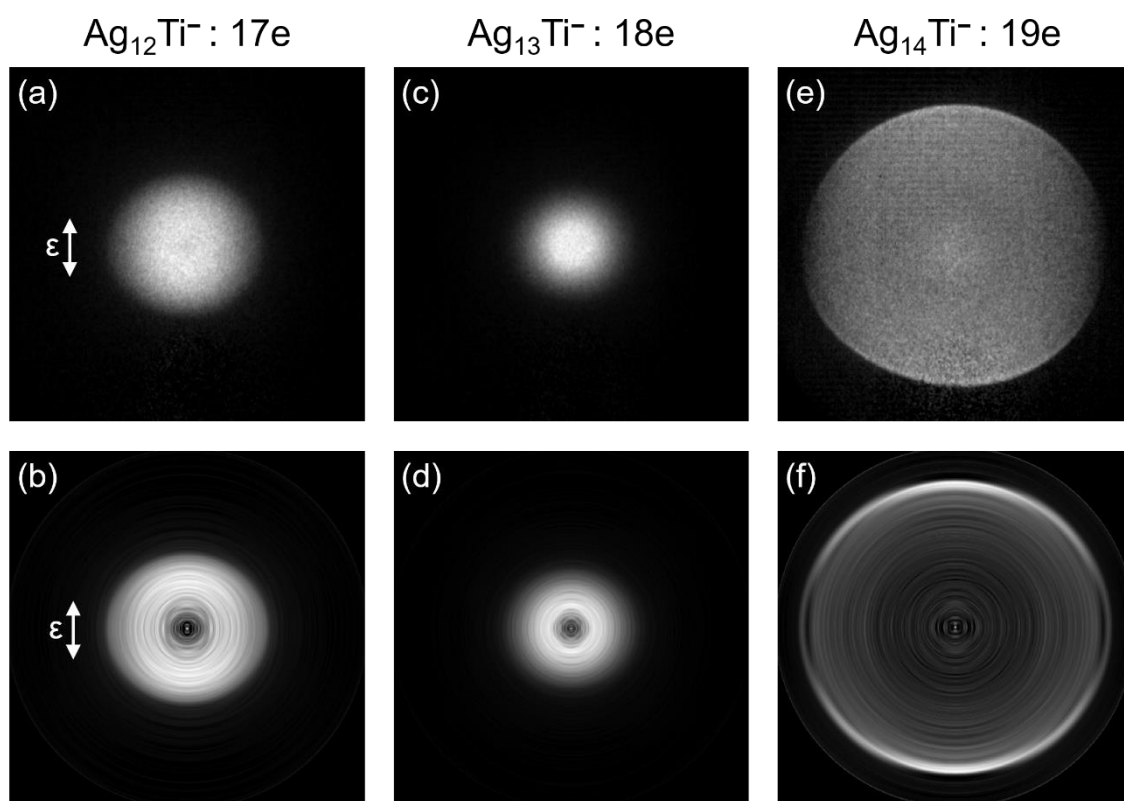


Figure 6.6. Photoelectron images (a, c, and e) and 2D slice images (b, d, and f) of Ag_NTi^- for $N = 12, 13$, and 14 . The images shown in the left side are for 17-e clusters; central panels for 18-e clusters; right panels for 19-e clusters. The direction of polarization is given in panels (a) and (b) by arrows.

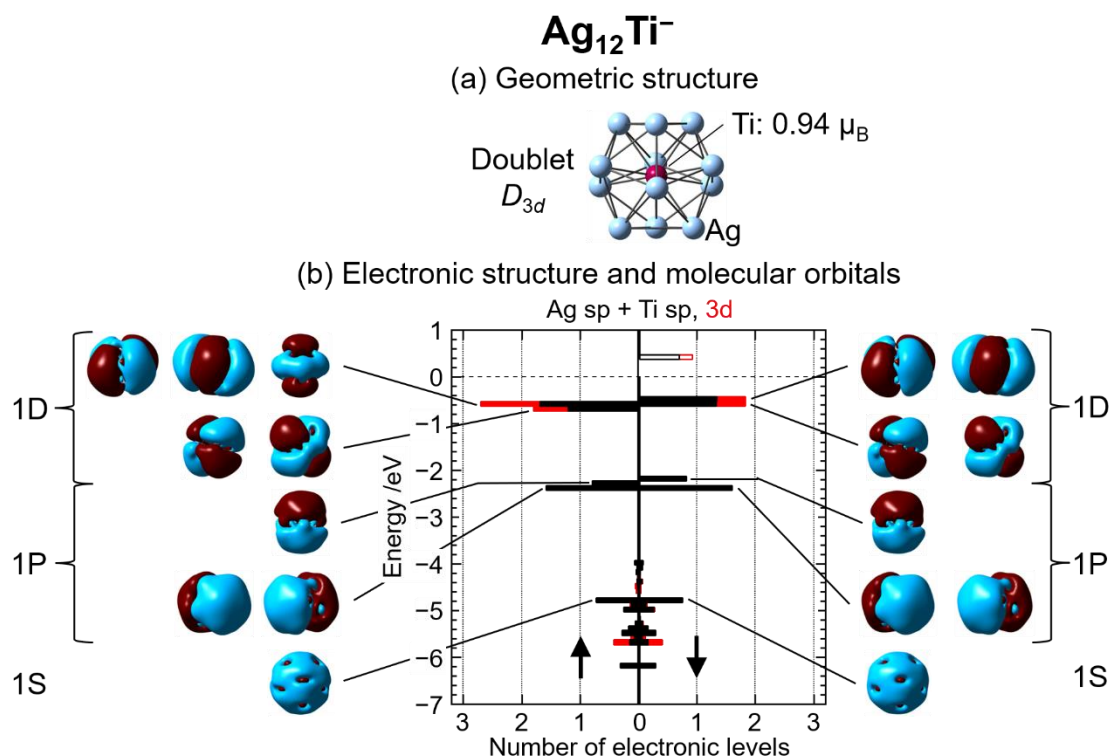


Figure 6.7. Results of DFT calculations on $\text{Ag}_{12}\text{Ti}^-$. Panel (a) shows an optimized geometric structure along with its symmetry, spin multiplicity, and a local magnetic moment on the Ti atom. Panel (b) exhibits an electronic structure depicted by density-of-states (DOS) diagrams for majority and minority spins. Bars in black and red show DOSs of sp and 3d orbitals, respectively. The number of electronic levels is shown by histograms with 0.1-eV energy windows. The dashed line at 0 eV represents the chemical potential, below which the levels are occupied. The contours of the wave functions illustrate formation of 1S, 1P, and 1D orbitals with isovalue of 0.0035.

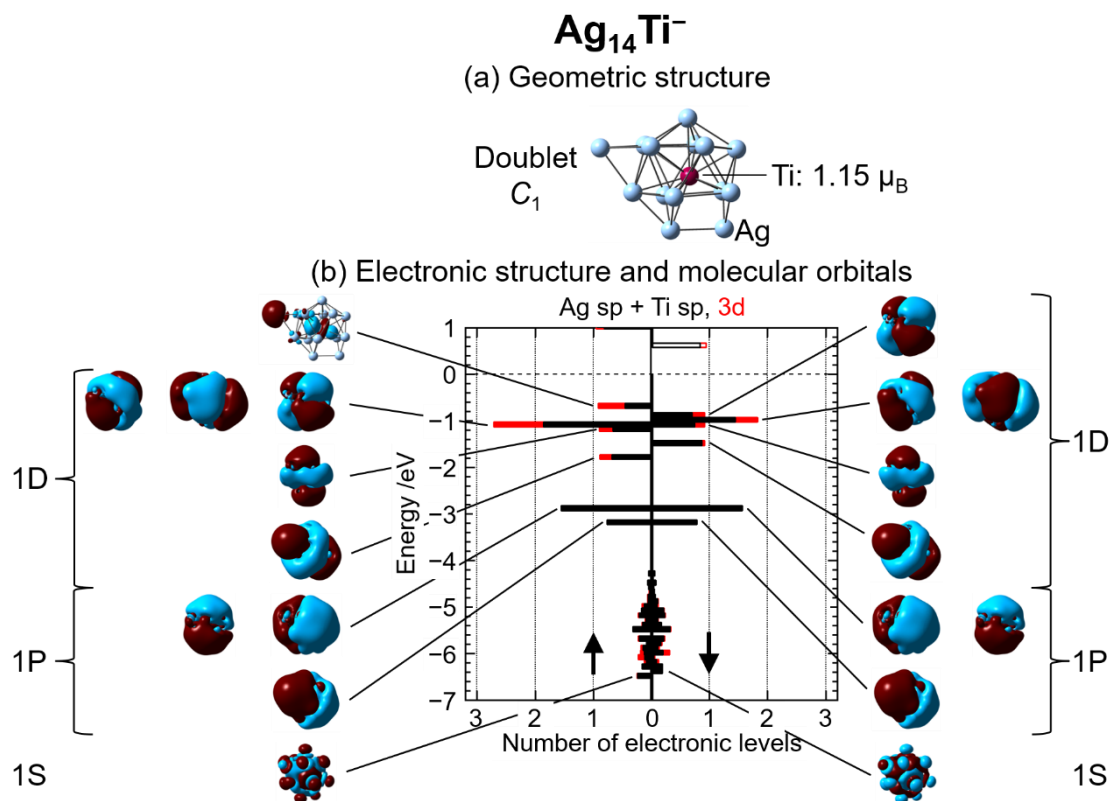


Figure 6.8. Results of DFT calculations on Ag₁₄Ti⁻. Panel (a) shows an optimized geometric structure along with its symmetry, spin multiplicity, and a local magnetic moment on the Ti atom. Panel (b) exhibits an electronic structure depicted by density-of-states (DOS) diagrams for majority and minority spins. Bars in black and red show DOSs of sp and 3d orbitals, respectively. The number of electronic levels is shown by histograms with 0.1-eV energy windows. The dashed line at 0 eV represents the chemical potential, below which the levels are occupied. The contours of the wave functions illustrate formation of 1S, 1P, and 1D orbitals. The isovalue of HOMO is 0.03, whereas the isovalue of the other orbitals is 0.0035.

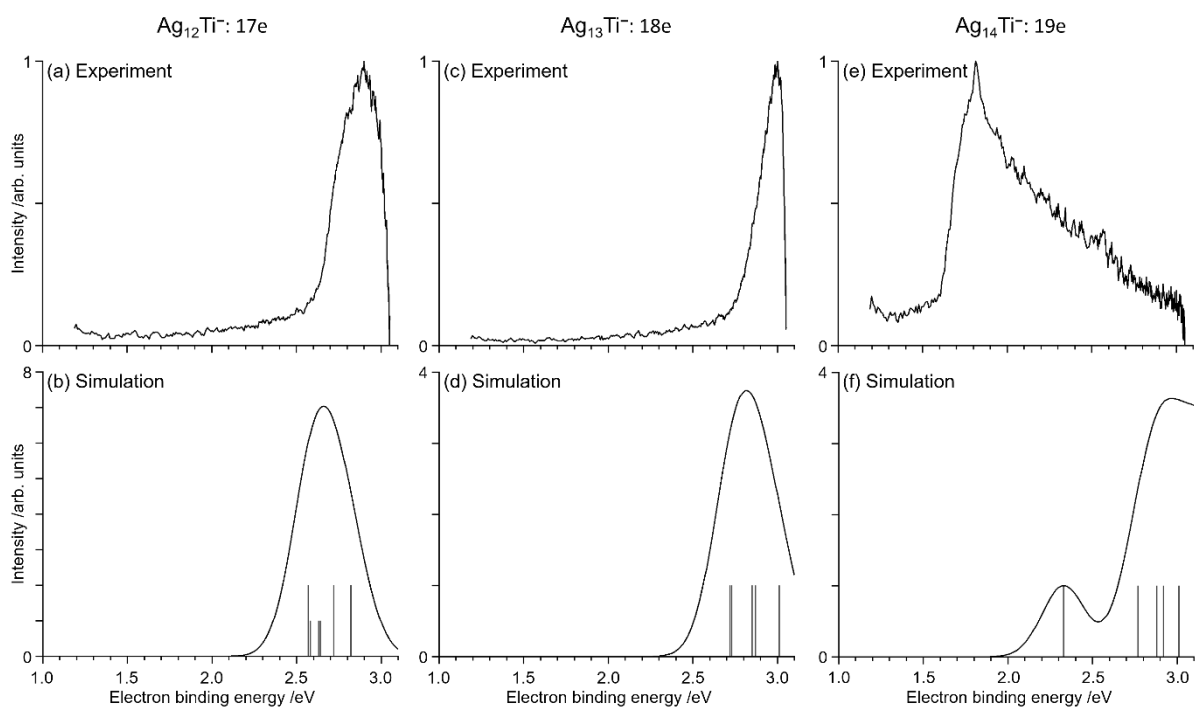


Figure 6.9. Photoelectron spectra of Ag_NTi^- for $N = 12, 13$, and 14 . Three pair of spectra are shown in the left, center, and right panels for $N = 12$ (17-e), 13 (18-e), and 14 (19-e), respectively. Panels (a), (c), and (e) show experimental spectra measured by PEI. Panels (b), (d), and (f) illustrate simulated spectra calculated by DFT and TDDFT.

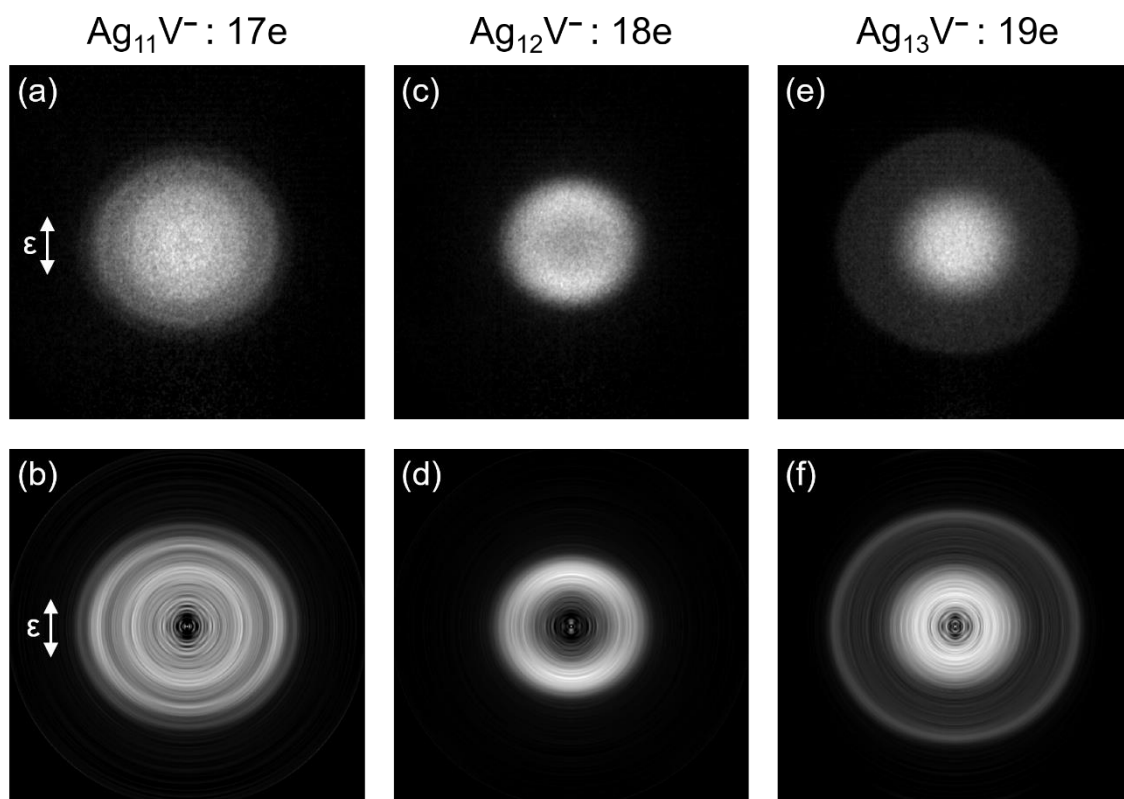


Figure 6.10. Photoelectron images (a, c, and e) and 2D slice images (b, d, and f) of Ag_NV^- for $N=11, 12$, and 13 . The images shown in the left side are for 17-e clusters; central panels for 18-e clusters; right panels for 19-e clusters. The direction of polarization is given in panels (a) and (b) by arrows.

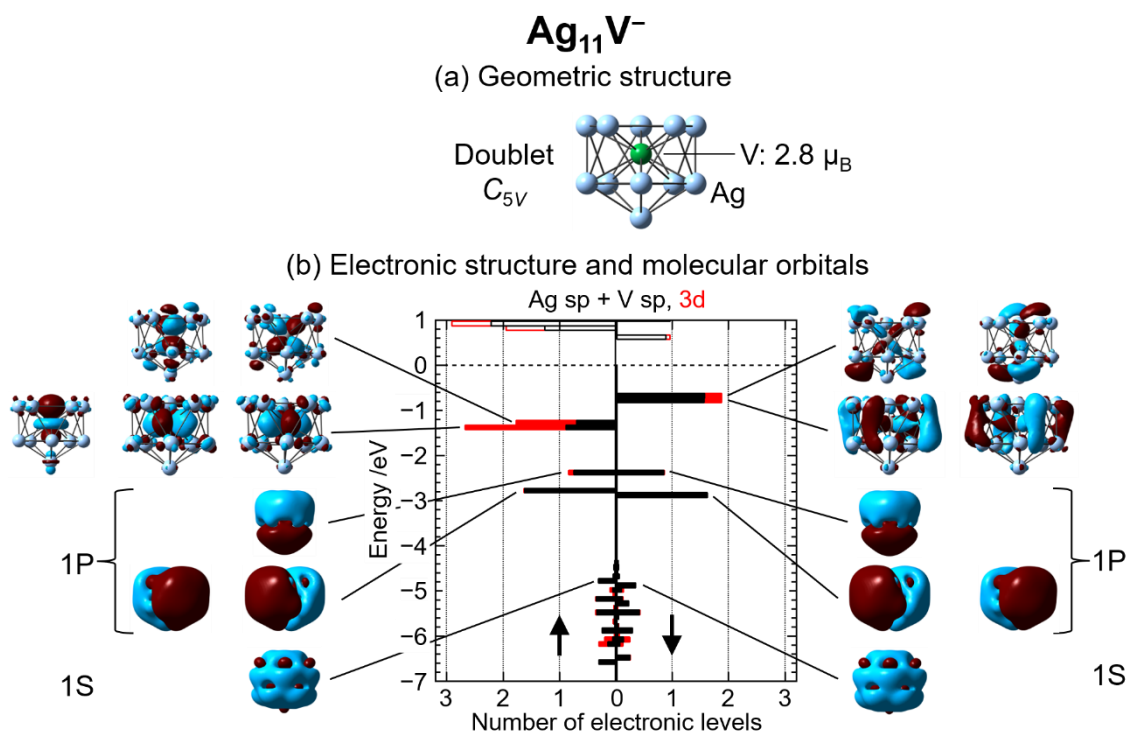


Figure 6.11. Results of DFT calculations on Ag₁₁V⁻. Panel (a) shows an optimized geometric structure along with its symmetry, spin multiplicity, and a local magnetic moment on the V atom. Panel (b) exhibits an electronic structure depicted by density-of-states (DOS) diagrams for majority and minority spins. Bars in black and red show DOSs of sp and 3d orbitals, respectively. The number of electronic levels is shown by histograms with 0.1-eV energy windows. The dashed line at 0 eV represents the chemical potential, below which the levels are occupied. The contours of the wave functions illustrate formation of 1S and 1P orbitals. The isovalue of top nine orbitals is 0.03, whereas the isovalue of the rest of them is 0.0035.

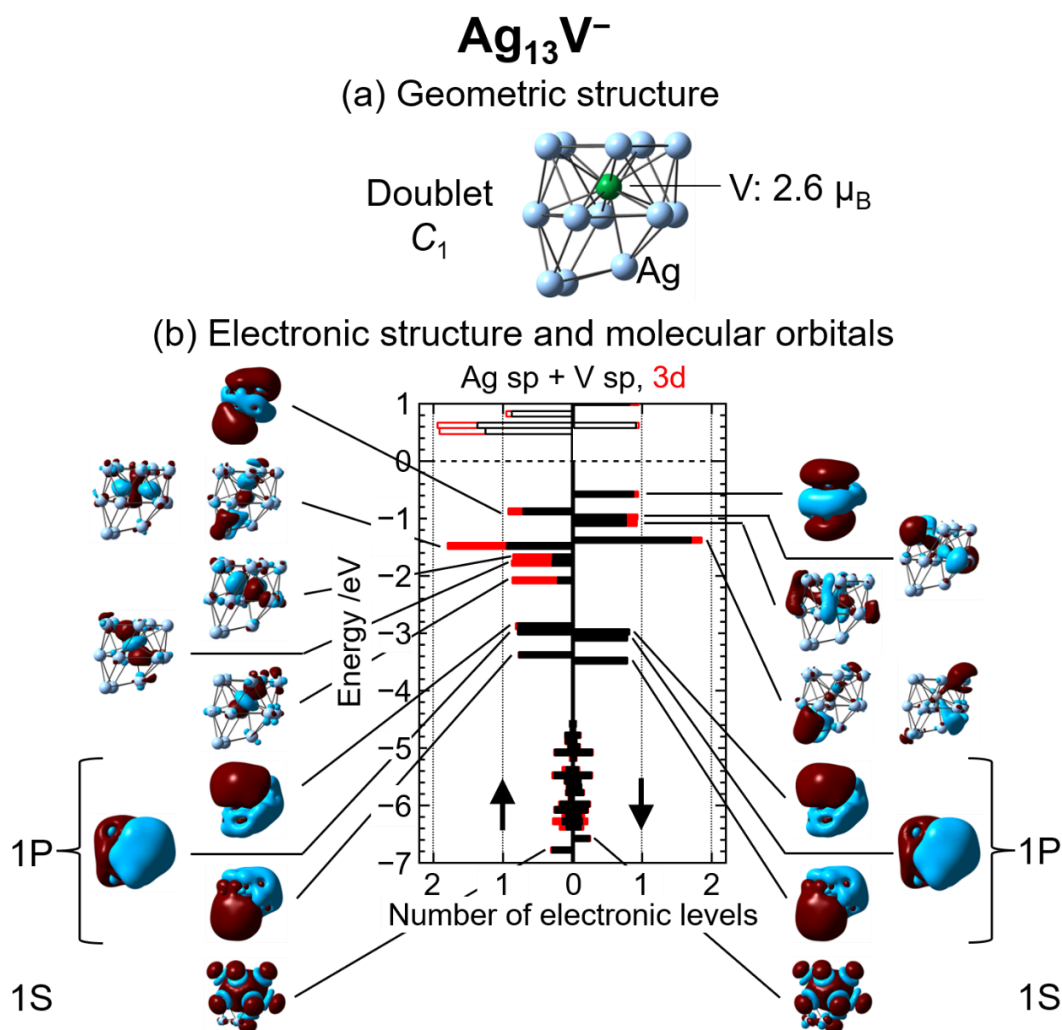


Figure 6.12. Results of DFT calculations on Ag_{13}V^- . Panel (a) shows an optimized geometric structure along with its symmetry, spin multiplicity, and a local magnetic moment on the V atom. Panel (b) exhibits an electronic structure depicted by density-of-states (DOS) diagrams for majority and minority spins. Bars in black and red show DOSs of sp and 3d orbitals, respectively. The number of electronic levels is shown by histograms with 0.1-eV energy windows. The dashed line at 0 eV represents the chemical potential, below which the levels are occupied. The contours of the wave functions illustrate formation of 1S, and 1P orbitals. The isovalue of HOMO, the second HOMO, and 1S and 1P orbitals is 0.0035, whereas that of the rest of them is 0.03.

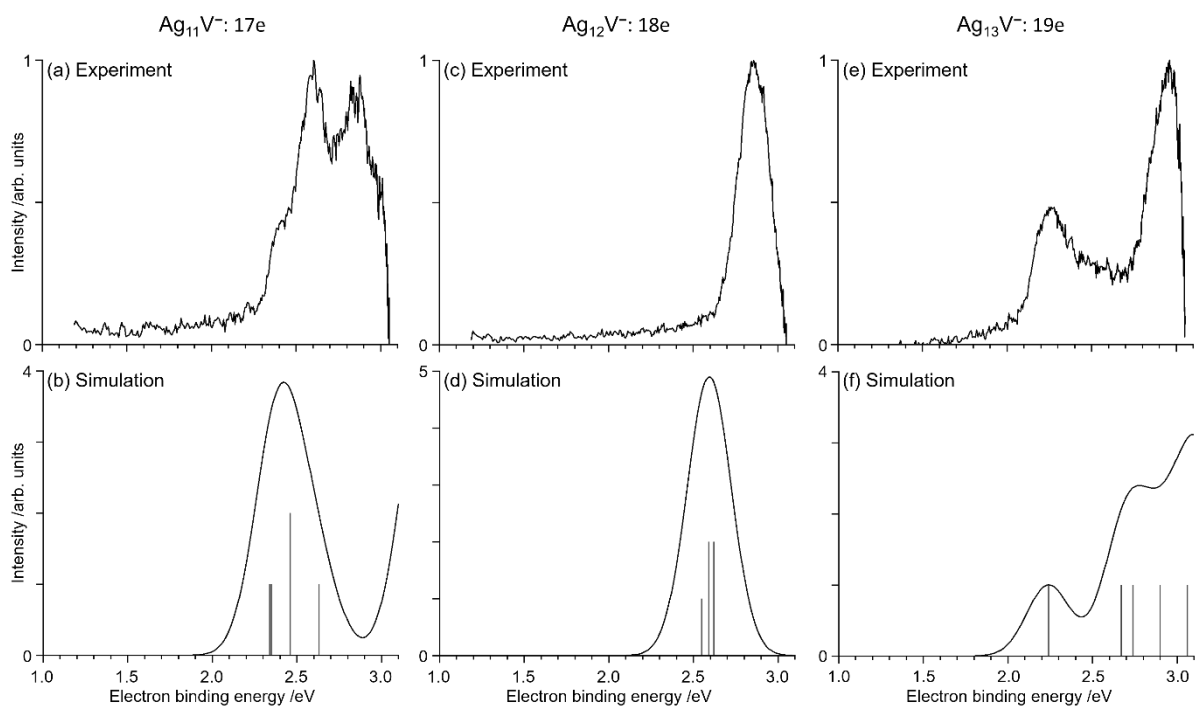


Figure 6.13. Photoelectron spectra of Ag_NV^- for $N = 11, 12$, and 13 . Three pair of spectra are shown in the left, center, and right panels for $N = 11$ (17-e), 12 (18-e), and 13 (19-e), respectively. Panels (a), (c), and (e) show experimental spectra measured by PEI. Panels (b), (d), and (f) illustrate simulated spectra calculated by DFT and TDDFT.

Chapter 7. Concluding Remarks

In the present study, reaction measurements and photoelectron imaging (PEI) spectroscopy were performed on 3d-transition-metal-doped silver cluster anions, Ag_NM^- ($\text{M} = \text{Sc-Ni}$), to explore their electronic and geometric structures with the aid of theoretical calculations.

The apparatus used for the reactivity measurements, described in Chapter 2, consisted of a cluster-ion source, a quadrupole mass filter, an ion trap, and a TOF mass spectrometer. Mass-selected cluster ions were introduced into the ion trap to react with O_2 gas. The resulting cluster ions were extracted from the trap and analyzed by the TOF mass spectrometer. Chapter 2 also described the apparatus used for photoelectron imaging. Mass-selected cluster anions were introduced into the apparatus to detach photoelectrons by using a CW diode laser. The detached photoelectrons were accelerated by a repeller, extractor, and ground electrodes and detected by a MCP. The angular distributions of the photoelectrons were recorded by a CMOS camera.

In Chapter 3, the reaction kinetics of Ag_NM^- were determined to investigate size-, dopant-, and charge-state-dependent effects. For all dopants, the fragment products observed at small sizes fell into three distinct categories: Ag-free MO_L^- , M-free Ag_N^- , and oxide fragment products, *i.e.*, Ag_NMO_L^- . The fragmentation pathways suggested that the dopant M served as an active site on the cluster surface. This was corroborated by DFT calculations, which showed that the M atom is located on the cluster surface. The adsorption energy of O_2 to M may be sufficiently large to cleave the Ag–Ag and Ag–M bonds, resulting in fragmentation. The formation of Ag-free MO_L^- also showed that the maximum number of released Ag atoms decreased from 8 for $\text{M} = \text{Sc}$ to 4 for $\text{M} = \text{Ni}$. This is related to $D(\text{M}^+-\text{O})$, which decreased from 6.9 eV for $\text{M} = \text{Sc}$ to 3.53 eV for $\text{M} = \text{Fe}$. Thus, the fragmentation channels may occur preferentially in systems doped with early transition metals. For large sizes, the main reaction channel was O_2 adsorption, rather than fragmentation. These large clusters, *e.g.*, $\text{Ag}_{14}\text{Sc}^-$, $\text{Ag}_{13}\text{Ti}^-$, and Ag_{12}V^-

showed endohedral geometries, suggesting that the reaction site changed to Ag atoms. Since the binding energies of O₂ to Ag_N⁻ are low, the oxygen adducts Ag_NMO₂⁻ could not proceed to fragmentation. By comparing the reaction products of Ag_NNi⁻ with those of Ag_NNi⁺, the maximum number of released Ag atoms for Ag_NNi⁻ is larger than that for Ag_NNi⁺. Since a negative charge promotes the reaction with molecular O₂ by electron transfer from the reactant to O₂, anionic clusters may produce a larger amount of excess energy available for dissociation than cationic clusters. Therefore, geometric structure, dopant element, and charge state all affect the reaction pathways.

In Chapter 4, the size-dependent reactivities of Ag_NM^{+/-} (M = Sc–Ni) were measured to investigate the localization/delocalization of 3d electrons, focusing on 18-e clusters. Ag_NM^{+/-} with early transition metals, *i.e.*, Sc, Ti, and V, exhibited the lowest reactivity among the 18-e clusters. For the late transition metals, *i.e.*, Fe, Co, and Ni, the cationic 18-e clusters also showed the lowest reactivity. The stability of these clusters was attributed to the closed electronic structure with delocalized 3d electrons. In contrast, Ag₉Fe⁻, Ag₈Co⁻, and Ag₇Ni⁻ exhibited high reactivity, as did neighboring sizes, even though they were all 18-e clusters. DFT calculations revealed that the transition metal atom is endohedrally doped in the former stable clusters, whereas the dopant M is located on the cluster surface. Therefore, it is concluded that the electron counting rule works only when the dopant atom is encapsulated by the host Ag atoms. For Cr- and Mn-doping, the half-filled 3d orbital of Cr and Mn is so stable that the 3d electrons are localized in both endohedral Ag₁₃Cr⁺ and Ag₁₂Mn⁺ and exohedral Ag₁₁Cr⁻ and Ag₁₀Mn⁻.

The present findings for open-shell Ag₈Co⁻ contradicted those of a previous study by Tono *et al.* based on photoelectron spectroscopy, in which they reported that Ag₈Co⁻ formed a closed electronic shell with delocalized 3d electrons. To overcome this contradiction, updated DFT and TDDFT calculations were performed on this cluster, and the results were reported in Chapter 5. Its geometric structure was confirmed to be exohedral by the updated DFT calculation. Furthermore, the PES was simulated by

TDDFT based on the exohedral geometry, which reproduced the experimental PES reported previously by Tono *et al.* The contradiction was solved in this way, and both the reactivities and the PES spectra are now explained consistently. Theoretical calculations thus provide a revised understanding of Ag_8Co^- : the s–d interaction is essentially weak, such that the 3d electrons of Co are localized, resulting in an open-shell triplet state. The electronic and geometric structures of Ag_6Co^- and Ag_7Co^- were also investigated. Both of these most stable isomers showed exohedral geometries and open electronic shell structures. Therefore, the 3d electrons in these clusters may also be localized on the Co atom.

In Chapter 6, the PEI spectroscopy results were presented. For Sc-doped clusters, the photoelectron image of $\text{Ag}_{15}\text{Sc}^-$ (19-e) suggests that the SOMO may be an s-like orbital, which provides evidence for the DFT calculations. The PES, combined with the theoretical calculations, revealed that the Sc 3d electron is delocalized and accommodated in superatomic 1D orbitals. In addition, the PES of $\text{Ag}_{14}\text{Sc}^-$ and $\text{Ag}_{13}\text{Sc}^-$ showed that the electron binding energy (EBE) of $\text{Ag}_{14}\text{Sc}^-$ is largest among the three Sc-doped clusters, suggesting that $\text{Ag}_{14}\text{Sc}^-$ is the most stable cluster, as indicated by reactivity measurements. Therefore, the 3d electron may be delocalized in Sc-doped clusters regardless of the number of valence electrons. For Ag_NTi^- , the present PEI study revealed that $\text{Ag}_{14}\text{Ti}^-$ (19-e) has a 2S-type HOMO and that the EBE of $\text{Ag}_{13}\text{Ti}^-$ is the largest. The PES, along with the theoretical calculations, revealed that 3d electrons are delocalized in $\text{Ag}_{12}\text{Ti}^-$, $\text{Ag}_{13}\text{Ti}^-$, and $\text{Ag}_{14}\text{Ti}^-$ to be accommodated in superatomic 1D orbitals. For V-doped clusters, the photoelectron image and PES of Ag_{13}V^- (19-e) suggested that the HOMO may not be the 2S orbital, unlike in Sc- and Ti-doped clusters. The DFT calculations for the V-doped cluster revealed that the 3d orbitals are localized on the V atom, resulting in a local magnetic moment on the V atom. The same theoretical result was obtained for Ag_{11}V^- (17-e). Thus, unlike the 3d electrons of the V atom, those of Sc and Ti atoms may preferentially delocalize in clusters.

This thesis systematically investigated the endohedral/exohedral geometries and

open/closed electronic structures of Ag_NM^- through reactivity measurements and PEI spectroscopy, in combination with DFT calculations. Thanks to the fact that the size-dependent reactivity reflected the stability of Ag_NM^- , the author discovered new magic-sized clusters: $\text{Ag}_{14}\text{Sc}^-$, $\text{Ag}_{13}\text{Ti}^-$, and Ag_{12}V^- . It was found that encapsulation of the dopant plays an important role, alongside electron counting, in delocalizing the 3d electrons, especially in the case of Ag_{12}V^- . DFT calculations for these clusters showed that 1S, 1P, 1D superatomic orbitals were formed. The energy levels of these orbitals were determined by PEI spectroscopy. The present thesis is the first study to conduct an experimental examination of the electronic structures of Ag_NM^- by the PEI method. Neighboring clusters were also investigated by PEI spectroscopy. It was found that the 3d electrons in Sc- and Ti-doped clusters with 17 and 19 electrons were delocalized, in contrast to V-doped clusters, whose 3d electrons were localized on the V atom. The present method for investigating the electronic and geometric structures of not only transition-metal-doped silver clusters but also cluster systems more generally will help to elucidate the origins of these cluster-size-dependent properties.

References

- [1] W. A. de Heer, *Rev. Mod. Phys.* **1993**, 65, 611–676.
- [2] P. Jena, Q. Sun, *Chem. Rev.* **2018**, 118, 5755–5870.
- [3] W. D. Knight, K. Clemenger, W. A. de Heer, W. A. Saunders, M. Y. Chou, M. L. Cohen, *Phys. Rev. Lett.* **1984**, 52, 2141–2143.
- [4] I. Katakuse, T. Ichihara, Y. Fujita, T. Matsuo, T. Sakurai, H. Matsuda, *Int. J. Mass Spectrom. Ion Process.* **1985**, 67, 229–236.
- [5] I. Katakuse, T. Ichihara, Y. Fujita, T. Matsuo, T. Sakurai, H. Matsuda, *Int. J. Mass Spectrom. Ion Process.* **1986**, 74, 33–41.
- [6] R. E. Leuchtner, A. C. Harms, A. W. Castleman, Jr., *J. Chem. Phys.* **1989**, 91, 2753–2754.
- [7] Z. Luo, A. W. Castleman, Jr., S. N. Khanna, *Chem. Rev.* **2016**, 116, 14456–14492.
- [8] K. J. Taylor, C. L. Pettiette-Hall, O. Cheshnovsky, R. E. Smalley, *J. Chem. Phys.* **1992**, 96, 3319–3329.
- [9] T. Diederich, T. Dppner, T. Fennel, J. Tiggesbümker, K. H. Meiwes-Broer, *Phys. Rev. A - At. Mol. Opt. Phys.* **2005**, 72, 1–11.
- [10] R. B. King, I. Silaghi-Dumitrescu, *J. Chem. Soc. Dalt. Trans.* **2008**, 6083–6088.
- [11] S. Sajjad, T. Mahmood, R. Ludwig, K. Ayub, *Solid State Sci.* **2018**, 86, 60–68.
- [12] W. Ekardt, *Phys. Rev. B* **1984**, 29, 1558–1564.
- [13] W. G. Sun, J. J. Wang, C. Lu, X. X. Xia, X. Y. Kuang, A. Hermann, *Inorg. Chem.* **2017**, 56, 1241–1248.
- [14] Z. Luo, G. U. Gamboa, J. C. Smith, A. C. Reber, J. U. Reveles, S. N. Khanna, A. W. Castleman, Jr., *J. Am. Chem. Soc.* **2012**, 134, 18973–18978.
- [15] T. Watanabe, T. Tsukuda, *J. Phys. Chem. C* **2013**, 117, 6664–6668.
- [16] M. M. Kappes, P. Radi, M. Schär, E. Schumacher, *Chem. Phys. Lett.* **1985**, 119, 11–16.
- [17] W. Bouwen, F. Vanhoutte, F. Despa, S. Bouckaert, S. Neukermans, L. Theil Kuhn, H. Weidele, P. Lievens, R. E. Silverans, *Chem. Phys. Lett.* **1999**, 314, 227–233.
- [18] K. Majer, B. V. Issendorff, *Phys. Chem. Chem. Phys.* **2012**, 14, 9371–9376.
- [19] S. Nonose, Y. Sone, K. Onodera, S. Sudo, K. Kaya, *J. Phys. Chem.* **1990**, 94, 2744–2746.
- [20] S. Datta, M. Kabir, T. Saha-Dasgupta, A. Mookerjee, *Phys. Rev. B - Condens. Matter Mater. Phys.* **2009**, 80, 1–9.

- [21] J. Kondo, *Prog. Theor. Phys.* **1964**, 32, 37–49.
- [22] M. D. Daybell, W. A. Steyert, *Rev. Mod. Phys.* **1968**, 40, 380–389.
- [23] A. J. Heeger, *Solid State Phys.* **1970**, 23, 283–411.
- [24] Q. Sun, X. G. Gong, Q. Q. Zheng, D. Y. Sun, G. H. Wang, *Phys. Rev. B* **1996**, 54, 10896–10904.
- [25] Q. Sun, Q. Wang, J. Z. Yu, Z. Q. Li, J. T. Wang, Y. Kawazoe, *J. Phys. I* **1997**, 7, 1233–1244.
- [26] M. Zhang, X. Y. Gu, W. L. Zhang, L. N. Zhao, L. M. He, Y. H. Luo, *Phys. B Condens. Matter* **2010**, 405, 642–648.
- [27] P. Pykkö, N. Runeberg, *Angew. Chemie - Int. Ed.* **2002**, 41, 2174–2176.
- [28] S.-Y. Wang, J.-Z. Yu, H. Mizuseki, Q. Sun, C.-Y. Wang, Y. Kawazoe, *Phys. Rev. B* **2004**, 70, 165413.
- [29] M. Sargolzaei, N. Lotfizadeh, *Phys. Rev. B* **2011**, 83, 1–8.
- [30] X. Gong, W. Ju, T. Li, Z. Feng, Y. Wang, *J. Clust. Sci.* **2015**, 26, 759–773.
- [31] P. Pykkö, *J. Organomet. Chem.* **2006**, 691, 4336–4340.
- [32] H. T. Pham, N. T. Cuong, N. M. Tam, N. T. Tung, *J. Phys. Chem. A* **2016**, 120, 7335–7343.
- [33] J. Zhao, Q. Du, S. Zhou, V. Kumar, *Chem. Rev.* **2020**, 120, 9021–9163.
- [34] S. Neukermans, E. Janssens, H. Tanaka, R. E. Silverans, P. Lievens, *Phys. Rev. Lett.* **2003**, 90, 033401.
- [35] E. Janssens, H. Tanaka, S. Neukermans, R. E. Silverans, P. Lievens, *Phys. Rev. B* **2004**, 69, 085402.
- [36] E. Janssens, S. Neukermans, P. Lievens, *Curr. Opin. Solid State Mater. Sci.* **2004**, 8, 185–193.
- [37] E. Janssens, S. Neukermans, H. M. T. Nguyen, M. T. Nguyen, P. Lievens, *Phys. Rev. Lett.* **2005**, 94, 113401.
- [38] E. Janssens, S. Neukermans, X. Wang, N. Veldeman, R. E. Silverans, P. Lievens, *Eur. Phys. J. D* **2005**, 34, 23–27.
- [39] F. C. Frank, J. S. Kasper, *Acta Crystallogr.* **1958**, 11, 184–190.
- [40] N. Veldeman, T. Höltzl, S. Neukermans, T. Veszprémi, M. T. Nguyen, P. Lievens, *Phys. Rev. A* **2007**, 76, 011201.
- [41] T. Höltzl, N. Veldeman, J. De Haeck, T. Veszprémi, P. Lievens, M. T. Nguyen, *Chem. - A Eur. J.* **2009**, 15, 3970–3982.
- [42] K. Hirsch, V. Zamudio-Bayer, A. Langenberg, M. Niemeyer, B. Langbehn, T. Möller, A. Terasaki, B. V. Issendorff, J. T. Lau, *Phys. Rev. Lett.* **2015**, 114, 087202.

- [43] H. Handschuh, C. Y. Cha, P. S. Bechthold, G. Ganteför, W. Eberhardt, *J. Chem. Phys.* **1995**, *102*, 6406–6422.
- [44] W. H. Blades, A. C. Reber, S. N. Khanna, L. López-Sosa, P. Calaminici, A. M. Köster, *J. Phys. Chem. A* **2017**, *121*, 2990–2999.
- [45] S. Sarugaku, R. Murakami, J. Matsumoto, T. Kawano, M. Arakawa, A. Terasaki, *Chem. Lett.* **2017**, *46*, 385–388.
- [46] S. Sarugaku, M. Arakawa, T. Kawano, A. Terasaki, *J. Phys. Chem. C* **2019**, *123*, 25890–25897.
- [47] K. Tono, A. Terasaki, T. Ohta, T. Kondow, *Chem. Phys. Lett.* **2007**, *449*, 276–281.
- [48] H. Haberland, M. Karrais, M. Mall, *Zeitschrift für Phys. D Atoms, Mol. Clust.* **1991**, *20*, 413–415.
- [49] B. C. Guo, K. P. Kerns, A. W. Castleman, Jr., *J. Phys. Chem.* **1992**, *96*, 6931–6937.
- [50] B. A. Mamyrin, V. I. Karataev, D. V. Shmikk, V. A. Zagulin, *Sov. Physics. JETP* **1973**, *37*, 45–48.
- [51] S. Sarugaku, M. Arakawa, A. Terasaki, *Int. J. Mass Spectrom.* **2017**, *414*, 65–69.
- [52] T. Handa, T. Horio, M. Arakawa, A. Terasaki, *Int. J. Mass Spectrom.* **2020**, *451*, 116311.
- [53] L. A. Posey, M. J. Deluca, M. A. Johnson, *Chem. Phys. Lett.* **1986**, *131*, 170–174.
- [54] A. T. J. B. Eppink, D. H. Parker, *Rev. Sci. Instrum.* **1997**, *68*, 3477–3484.
- [55] D. A. Horke, G. M. Roberts, J. Lecointre, J. R. R. Verlet, *Rev. Sci. Instrum.* **2012**, *83*, 063101.
- [56] M. J. Frisch, G. W. Trucks, H. B. Schlegel, G. E. Scuseria, M. A. Robb, J. R. Cheeseman, G. Scalmani, V. Barone, G. A. Petersson, H. Nakatsuji, X. Li, M. Caricato, A. V. Marenich, J. Bloino, B. G. Janesko, R. Gomperts, B. Mennucci, H. P. Hratchian, J. V. Ortiz, A. F. Izmaylov, J. L. Sonnenberg, D. Williams-Young, F. Ding, F. Lipparini, F. Egidi, J. Goings, B. Peng, A. Petrone, T. Henderson, D. Ranasinghe, V. G. Zakrzewski, J. Gao, N. Rega, G. Zheng, W. Liang, M. Hada, M. Ehara, K. Toyota, R. Fukuda, J. Hasegawa, M. Ishida, T. Nakajima, Y. Honda, O. Kitao, H. Nakai, T. Vreven, K. Throssell, J. A. Montgomery, Jr., J. E. Peralta, F. Ogliaro, M. J. Bearpark, J. J. Heyd, E. N. Brothers, K. N. Kudin, V. N. Staroverov, T. A. Keith, R. Kobayashi, J. Normand, K. Raghavachari, A. P. Rendell, J. C. Burant, S. S. Iyengar, J. Tomasi, M. Cossi, J. M. Millam, M. Klene, C. Adamo, R. Cammi, J. W. Ochterski, R. L. Martin, K.

- Morokuma, O. Farkas, J. B. Foresman, D. J. Fox, Gaussian 16 (Revision A.03), Gaussian Inc., Wallingford, CT, **2016**.
- [57] M. Reiher, O. Salomon, B. A. Hess, *Theor. Chem. Acc.* **2001**, *107*, 48–55.
 - [58] A. J. H. Wachters, *J. Chem. Phys.* **1970**, *52*, 1033–1036.
 - [59] P. J. Hay, W. R. Wadt, *J. Chem. Phys.* **1985**, *82*, 299–310.
 - [60] A. E. Reed, L. A. Curtiss, F. Weinhold, *Chem. Rev.* **1988**, *88*, 899–926.
 - [61] E. D. Glendening, A. E. Reed, J. E. Carpenter, F. Weinhold, NBO Version 3.1.
 - [62] S. Yin, E. R. Bernstein, *Phys. Chem. Chem. Phys.* **2018**, *20*, 22610–22622.
 - [63] B. C. Guo, K. P. Kerns, A. W. Castleman, *J. Chem. Phys.* **1992**, *96*, 8177–8186.
 - [64] C. Hsuan Wei, *Inorg. Chem.* **1969**, *8*, 2384–2397.
 - [65] S. Yin, Z. Wang, E. R. Bernstein, *J. Chem. Phys.* **2013**, *139*, 084307.
 - [66] M. Neumaier, M. Olzmann, B. Kiran, K. H. Bowen, B. Eichhorn, S. T. Stokes, A. Buongiorno, R. Burgert, H. Schnöckel, *J. Am. Chem. Soc.* **2014**, *136*, 3607–3616.
 - [67] T. Ito, M. Arakawa, Y. Taniguchi, A. Terasaki, *Zeitschrift für Phys. Chemie* **2019**, *233*, 759–770.
 - [68] K. Minamikawa, S. Sarugaku, M. Arakawa, A. Terasaki, *Phys. Chem. Chem. Phys.* **2022**, *24*, 1447–1455.
 - [69] P. C. Jennings, H. A. Aleksandrov, K. M. Neyman, R. L. Johnston, *J. Phys. Chem. C* **2015**, *119*, 11031–11041.
 - [70] H. Cruz-Martínez, L. López-Sosa, O. Solorza-Feria, P. Calaminici, *Int. J. Hydrogen Energy* **2017**, *2*, 2–9.
 - [71] E. Schumacher, *DETMECH – Chemical Reaction Kinetics Software*, University of Bern, **2003**
 - [72] L. Lai, D. Die, B.-X. Zheng, Q. Du, *J. Phys. Chem. Solids* **2021**, *148*, 109757.
 - [73] V. M. Medel, A. C. Reber, V. Chauhan, P. Sen, A. M. Köster, P. Calaminici, S. N. Khanna, *J. Am. Chem. Soc.* **2014**, *136*, 8229–8236.
 - [74] L. D. Socaciu, J. Hagen, J. Le Roux, D. Popolan, T. M. Bernhardt, L. Wöste, Š. Vajda, *J. Chem. Phys.* **2004**, *120*, 2078–2081.
 - [75] E. Janssens, X. J. Hou, M. T. Nguyen, P. Lievens, *J. Chem. Phys.* **2006**, *124*, 184319.
 - [76] H. T. Pham, L. Q. Ngo, M. P. Pham-Ho, M. T. Nguyen, *J. Phys. Chem. A* **2016**, *120*, 7964–7972.
 - [77] R. Dong, X. Chen, H. Zhao, X. Wang, H. Shu, Z. Ding, L. Wei, *J. Phys. B At. Mol. Opt. Phys.* **2011**, *44*, 035102.
 - [78] P. L. Rodríguez-Kessler, A. R. Rodríguez-Domínguez, *Comput. Theor. Chem.*

- 2015**, *1066*, 55–61.
- [79] P. L. Rodríguez-Kessler, S. Pan, E. Florez, J. L. Cabellos, G. Merino, *J. Phys. Chem. C* **2017**, *121*, 19420–19427.
 - [80] R. Xiong, D. Die, L. Xiao, Y. G. Xu, X. Y. Shen, *Nanoscale Res. Lett.* **2017**, *12*, 625.
 - [81] R. Xiong, D. Die, Y. G. Xu, B. X. Zheng, Y. C. Fu, *Phys. Chem. Chem. Phys.* **2018**, *20*, 15824–15834.
 - [82] P. Marín, J. A. Alonso, E. Germán, M. J. López, *J. Phys. Chem. A* **2020**, *124*, 6468–6477.
 - [83] C. Wang, Y. Yang, X. Liu, Y. Li, D. Song, Y. Tian, Z. Zhang, X. Shen, *Phys. Chem. Chem. Phys.* **2020**, *22*, 9053–9066.
 - [84] E. R. Fisher, J. L. Elkind, D. E. Clemmer, R. Georgiadis, S. K. Loh, N. Aristov, L. S. Sunderlin, P. B. Armentrout, *J. Chem. Phys.* **1990**, *93*, 2676–2691.
 - [85] J. Xu, M. T. Rodgers, J. B. Griffin, P. B. Armentrout, *J. Chem. Phys.* **1998**, *108*, 9339–9350.
 - [86] J. B. Griffin, P. B. Armentrout, *J. Chem. Phys.* **1997**, *106*, 4448–4462.
 - [87] J. B. Griffin, P. B. Armentrout, *J. Chem. Phys.* **1998**, *108*, 8062–8074.
 - [88] T. M. Bernhardt, J. Hagen, S. M. Lang, D. M. Popolan, L. D. Socaciu-Siebert, L. Wöste, *J. Phys. Chem. A* **2009**, *113*, 2724–2733.
 - [89] N. M. Reilly, J. U. Reveles, G. E. Johnson, S. N. Khanna, A. W. Castleman, *Chem. Phys. Lett.* **2007**, *435*, 295–300.
 - [90] M. F. Jarrold, J. E. Bower, *J. Chem. Phys.* **1986**, *85*, 5373–5375.
 - [91] A. Ruban, B. Hammer, P. Stoltze, H. L. Skriver, J. K. Nørskov, *J. Mol. Catal. A Chem.* **1997**, *115*, 421–429.
 - [92] M. Ichihashi, T. Hanmura, T. Kondow, *J. Chem. Phys.* **2006**, *125*, 133404.
 - [93] A. C. Reber, S. N. Khanna, P. J. Roach, W. H. Woodward, A. W. Castleman, *J. Am. Chem. Soc.* **2007**, *129*, 16098–16101.
 - [94] S. Sarugaku, M. Arakawa, T. Kawano, A. Terasaki, *J. Phys. Chem. C* **2019**, *123*, 25890–25897.
 - [95] M. Arakawa, M. Horioka, K. Minamikawa, T. Kawano, A. Terasaki, *Phys. Chem. Chem. Phys.* **2021**, *23*, 22947–22956.
 - [96] D. G. Leopold, J. Ho, W. C. Lineberger, *J. Chem. Phys.* **1986**, *86*, 1715–1726.
 - [97] J. Ho, K. M. Ervin, W. C. Lineberger, *J. Chem. Phys.* **1990**, *93*, 6987–7002.
 - [98] J. Conceicao, R. T. Laaksonen, L. S. Wang, T. Guo, P. Nordlander, R. E. Smalley, *Phys. Rev. B* **1995**, *51*, 4668–4671.
 - [99] H. Häkkinen, B. Yoon, U. Landman, X. Li, H. J. Zhai, L. S. Wang, *J. Phys.*

- Chem. A* **2003**, *107*, 6168–6175.
- [100] W. Huang, H. J. Zhai, L. S. Wang, *J. Am. Chem. Soc.* **2010**, *132*, 4344–4351.
- [101] X. J. Hou, E. Janssens, P. Lievens, M. T. Nguyen, *Chem. Phys.* **2006**, *330*, 365–379.
- [102] R. Mabbs, E. Grumbling, K. Pichugin, A. Sanov, *Chem. Soc. Rev.* **2009**, *38*, 2169–2177.
- [103] C. Bartels, C. Hock, J. Huwer, R. Kuhn, J. Schwobel, B. von Issendorff, *Science*. **2009**, *323*, 1323–1327.
- [104] G. M. Roberts, J. L. Nixon, J. Lecointre, E. Wrede, J. R. R. Verlet, *Rev. Sci. Instrum.* **2009**, *80*, 053104.
- [105] J. Cooper, R. N. Zare, *J. Chem. Phys.* **1968**, *48*, 942–943.
- [106] B. Yin, Q. Du, L. Geng, H. Zhang, Z. Luo, S. Zhou, J. Zhao, *CCS Chem.* **2021**, *3*, 219–229.
- [107] D. A. Shirley, R. L. Martin, S. P. Kowalczyk, F. R. McFeely, L. Ley, *Phys. Rev. B* **1977**, *15*, 544–552.
- [108] J. M. Dyke, B. W. J. Gravenor, M. P. Hastings, G. D. Josland, A. Morris, *J. Electron Spectros. Relat. Phenomena* **1985**, *35*, 65–75.

List of Publications

Publications related to the thesis

(Chapter 3)

- [1] **K. Minamikawa**, M. Horioka, N. Hayashi, M. Arakawa, and A. Terasaki
Reaction kinetics of transition-metal-doped silver cluster anions toward oxygen
Manuscript in preparation

(Chapter 4)

- [2] **K. Minamikawa**, S. Sarugaku, M. Arakawa, and A. Terasaki
Electron counting in cationic and anionic silver clusters doped with a 3d transition-metal atom: endo- vs. exohedral geometry
Phys. Chem. Chem. Phys. **2022**, 24, 1447–1455

(Chapter 5)

- [3] **K. Minamikawa**, M. Arakawa, K. Tono, and A. Terasaki
A revisit to electronic structures of cobalt-doped silver cluster anions by size-dependent reactivity measurement
Chem. Phys. Lett. **2020**, 753, 137613

(Chapter 6)

- [4] **K. Minamikawa**, T. Horio, T. Nishizato, H. Hashimoto, K. Matsumoto, M. Arakawa, and A. Terasaki
Electronic structures of Sc-, Ti-, and V-doped silver cluster anions probed by photoelectron imaging
Manuscript in preparation

Publications not related to the thesis

- [1] M. Arakawa, M. Horioka, **K. Minamikawa**, T. Kawano, and A. Terasaki
Reaction kinetics of nitric oxide on size-selected silver cluster cations
J. Phys. Chem. C **2020**, 124, 26881–26888

- [2] T. Hayakawa, M. Arakawa, S. Kono, T. Handa, N. Hayashi, **K. Minamikawa**, T. Horio, and A. Terasaki
X-ray absorption spectroscopy of small copper-oxide cluster ions for analyses of Cu oxidation state and Ar complexation: CuOAr^+ and Cu_2O_2^+
Z. Phys. Chem. **2021**, 235, 213–224
- [3] M. Arakawa, M. Horioka, **K. Minamikawa**, T. Kawano, and A. Terasaki
Reaction of nitric oxide molecules on transition-metal-doped silver cluster cations: size- and dopant-dependent reaction pathways
Phys. Chem. Chem. Phys. **2021**, 23, 22947–22956

Acknowledgements

I would like to express my sincere gratitude to the following people for their tremendous help.

First of all, I would like to thank my direct supervisor, Professor Akira Terasaki, for his enthusiastic guidance in the last six years. He taught me all the interesting aspects of cluster science. During my first challenging encounter with cluster science, he was keen to teach me the basics of cluster science and the skills I would need for various experimental techniques. He kindly advised me on how best to interpret the experimental data and the theoretical calculation results. He also gave me important advice as I prepared for presentations at domestic and international conferences. In addition, he carefully reviewed my papers. Without his patient help, this thesis would not have been possible.

I would like to express my gratitude to Associate Professor Takuya Horio, in particular for his help with photoelectron imaging spectroscopy. I had little prior knowledge of the experimental method; he was the one who taught me the basics in considerable detail. When we started up the new velocity map imaging (VMI) apparatus, he provided me with much-needed guidance. He also showed me how to interpret the experimental results and helped me in preparing for presentations.

I would like to express my gratitude to Assistant Professor Masashi Arakawa. He gave me valuable advice on the interpretation of experimental and theoretical results. He helped me to find solutions when I encountered problems with laboratory equipment. He also gave me important advice regarding my papers and presentations.

I also would like to thank Professors Haruyuki Nakano, Kenji Furuya, and Hideaki Kano for their invaluable advice on my research.

Much appreciation is due to the former and current members of the Quantum Chemistry Laboratory (Kyushu University). Dr. Shun Sarugaku taught me how to handle the equipment and the methods of quantum chemical calculations. Mr. Tomoki

Kawano taught me the experimental procedures, ways of dealing with equipment-related problems, and how to analyze the experimental data. Mr. Masataka Horioka and Ms. Naho Hayashi assisted me with experiments and data analysis, especially in the present reactivity study. Mr. Tasuku Nishizato helped me with the VMI setup, experiments, and data analysis. Ms. Tamami Kawai supported me in office work and daily life at the laboratory. I would like to express my gratitude to all other members of the laboratory as well, too many to cite individually here.

I would like to thank Dr. Tetsuichiro Hayakawa (Genesis Research Institute, Inc.). He gave me a precious opportunity to join his research team at the High Energy Accelerator Research Organization. I had the chance to study X-ray absorption spectroscopy of clusters and learned the methods involved. In addition, I learned how to be attentive in research and take responsibility in experiments.

Finally, a big thank you to my family, without whose love and support, I would not have been able to concentrate on my research during the last six years.

Kento Minamikawa